Dark Matter Dynamics

by

Phillip Gregory Zukin

B.S. Physics
California Institute of Technology (2006)

Submitted to the Department of Physics
in partial fulfillment of the requirements for the degree of

Doctor of Philosophy in Physics

at the

MASSACHUSETTS INSTITUTE OF TECHNOLOGY

May 2012

Author .....
Department of Physics
May 18, 2012

Certified by .....
Edmund Bertschinger
Department Head, Professor of Physics
Thesis Supervisor

Accepted by .....
Krishna Rajagopal
Professor of Physics
Associate Department Head for Education

Dark Matter Dynamics

by

Phillip Gregory Zukin

Submitted to the Department of Physics
on May 18, 2012, in partial fulfillment of the
requirements for the degree of
Doctor of Philosophy in Physics

Abstract

N-body simulations have revealed a wealth of information about dark matter halos but their results are largely empirical. Here we attempt to shed light on simulation results by using a combination of analytic and numerical methods. First we generalize an analytic model of halo formation, known as Secondary Infall, to include the effects of tidal torque. Given this model we compare its predictions for halo profiles to simulation results and infer that angular momentum plays an important role in setting the structure of dark matter profiles at small radii. Next, we focus on explaining the origin of universality in halos. We find evidence that diffusion – which can potentially lead to universality – occurs during halo evolution and is partially sourced by external torques from large scale structure. This is surprising given that the halo is nonlinear and typically thought to be unaffected by neighboring structures. Last, we describe promising ways to analytically describe the evolution of nonlinear halos using a Fokker-Planck formalism.

Thesis Supervisor: Edmund Bertschinger
Title: Department Head, Professor of Physics

Acknowledgments

Thank you to my advisor, Ed Bertschinger, for his guidance. Thank you to the Astrophysics Department and the MKI community for their enthusiasm and passion for this field, which fueled my own. Thank you to my family for their love and support.

For my grandparents

Contents

List of Figures

Chapter 1

Introduction

The energy content of the universe, through Einstein's theory of General Relativity, influences the universe's geometry and evolution. Therefore – assuming General Relativity is correct – we can constrain the universe's components by measuring the geometry of the universe at different times. To measure the geometry of the universe, cosmologists use what is known as standard candles and standard rulers. These are astronomical objects for which we know their intrinsic brightness or size, respectively. Knowing the intrinsic brightness or size of an object, and measuring the object's apparent brightness or apparent size, constrains the distance to that object. This distance, when coupled with General Relativity, then allows us to infer the contents of the universe.

One common standard candle is a Supernovae Type IA explosion, which is believed to occur when a White Dwarf accretes enough matter from a neighboring star to become unstable, and then detonates. These extremely luminous explosions are observable very far away. Interestingly, they appear dimmer than cosmologists would have initially expected, leading the community to believe that the universe is currently undergoing an epoch of cosmological acceleration (Riess et al., 1998; Perlmutter et al., 1999). This is very unintuitive. Given an initial Big Bang, one would expect gravity acting on matter to pull back and decelerate the expansion of the universe. However, this observation implies that the universe is composed of a material that forces gravity

to push out and accelerate the expansion. The material that sources this expansion is called dark energy; the scientists who made the observations leading to dark energy's discovery have recently been awarded the Nobel Prize.

Supernovae explosions test our understanding of the universe on large scales and reveal that dark energy is a major component of our universe. It is also possible to test our understanding of the universe on smaller scales – like that of a galaxy – by calculating the mass of galaxies using two independent methods and then comparing both mass estimates. One method is dynamical in nature. Astronomers estimate the mass – assuming Newtonian Gravity is valid on these scales – based on the speed of orbiting objects. The other method is photometric in nature. Astronomers observe a total amount of light coming from the galaxy. They assume the galaxy is composed of stars. Given the mass and luminosity of an individual star, they then convert some total observed luminosity of the galaxy to an estimate of the total mass. With these two independent estimates of the mass, astronomers found that the dynamical mass estimate is much larger than the photometric estimate (Rubin & Ford, 1970). This, assuming Newton correctly described gravity on these scales, implies that there is a significant amount of mass in a galaxy that is not visible. This invisible component is known as Dark Matter; its existence was postulated by Zwicky in the 1930s based on observations of the Coma Cluster.

Observations like those described above – on both cosmological and galaxy scales – coupled with General Relativity, constrain our universe today to be composed of roughly 73% dark energy, 23% dark matter and 4% baryons (Komatsu et al., 2010). While baryons are directly observable and well understood, dark energy and dark matter are complete mysteries.

The simplest models for dark energy assume that it does not cluster. In other words, gravity does not produce dark energy clumps. Dark matter, on the other hand, can cluster. Therefore, as the universe evolves, dark energy stays smooth throughout,

while the dark matter gets more and more concentrated as gravity pulls matter onto initial over-densities. These large concentrations of dark matter are where galaxies eventually form.

Galaxy formation is a complicated nonlinear process. Our current understanding is that gravity makes dark matter clumps that grow with time. Initially, the baryons and dark matter are evenly mixed. Over time, however, since baryons can lose energy through more pathways than dark matter, most baryons settle into the center of the clumps. While at early times only gravity is relevant, other forces become important later on as baryons start to radiatively and mechanically couple to their environment.

Galaxy formation is of great interest to the community. Comparing theoretically predicted galaxies to observed ones not only tests our cosmological model on large scales, it also tests our theoretical understanding of astrophysical processes within galaxies. In other words, galaxies are systems which allow us to test our understanding of physics over a wide range of scales. Given the complex nature of galaxy formation – with many competing processes – it is best to first focus on the most massive component of a galaxy, known as the dark matter halo. Doing so simplifies the problem. Then – given a fundamental understanding of halo formation – one can later add complications in order to take into account the influence of baryons and develop a model which matches observations of galaxies. This thesis, as a result, focuses exclusively on dark matter halo formation.

A dark matter halo is composed of many gravitationally interacting dark matter particles. If a system contains more than two gravitationally interacting particles, it becomes difficult to understand completely with pen and paper. As a result, most studies of halo formation use purely numerical methods and run large computer programs known as N-body simulations. While numerical methods are useful, in order to really understand how halos form, it is necessary to develop analytic models that explain and bring intuition to the numerical results.

There is currently a large community of theoretical cosmologists that work on N-body simulations. Initially, the particles are given positions and velocities that are consistent with linear perturbation theory. These initial conditions are only valid at very early times before the dark matter starts to clump significantly. Then particles are evolved forward in time only subject to gravitational forces. Today, simulated universes shows distinct groups of particles – dark matter halos – of varying size ranging from roughly $10^6 M_\odot$ to $10^{14} M_\odot$. The lower limit depends on the mass of the smallest particle in the simulation while the upper limit depends on the size of the cosmological box simulated.

Many interesting trends have been discovered with these simulations. First, the density profiles of all halos can roughly be fit by an empirical formula, known as the NFW profile, that only depends on two parameters (Navarro et al., 1996, 1997). In addition, the pseudo-phase space density, which depends on the velocity of particles in the halo, also seems to follow a single functional form – the same power law – in different halos (Taylor & Navarro, 2001; Ludlow et al., 2010). Naively one would expect these quantities to depend on initial conditions, environment, and mass of the halo. However, N-body simulations find that – aside from scalings – the density and pseudo-phase space density profiles of halos are universal. This universality is extremely surprising and immediately brings forth many interesting theoretical questions. What is the origin of the NFW profile? Are dynamical processes responsible for the universality of these profiles? Why are certain halo properties universal while others are not?

While all of these dark matter halo properties are informative, they are all empirical. In order to gain better intuition for halo formation – and eventually galaxy formation – and understand the origin of these empirical relationships, this thesis explores different ways to analytically model halo formation.

Understanding halos analytically is straightforward at early times. Halos are initially linear in the quantity $\delta \equiv (\rho - \bar{\rho})/\bar{\rho}$, where ρ is the density and $\bar{\rho}$ is the mean matter density in the universe. For $\delta \ll 1$, the dark matter fluid equations of motion can be linearized and it is found that the over-density grows with time – in the matter dominated era – according to $\delta \propto t^{2/3}$ where t is the age of the universe. At one point, as the universe evolves, the over-density becomes $\delta \sim 1$ and the fluid equations are no longer valid. Hence it is necessary to explore other analytic techniques in order to track a halo's evolution into the nonlinear regime where we typically observe halos with $\delta > 200$ today.

An analytic formalism that can track a halo from the linear through the nonlinear regime is known as the Self-Similar Secondary Infall model (Gunn & Gott, 1972; Gott, 1975; Gunn, 1977). Secondary Infall describes the continuous accretion of mass shells onto an initial over-density. Self-similarity constrains the system to look identical when scaled in time and amplitude. Moreover, imposing self-similarity makes the system analytically tractable. In this thesis we generalize the model to take into account tidal torques acting on particles within the halo. In Chapters 2 and 3, we use our generalized model to gain intuition about the density and velocity profiles of dark matter halos. Both chapters are heavily based on published papers (Zukin & Bertschinger, 2010a,b).

In Chapter 4, we explore the origin of the 'observed' universality. Universality implies that information in the system has been lost, since the result does not depend on initial conditions, mass, or environment. One way to lose information is through dynamical processes, like diffusion. Another way occurs when analyzing the data, where for instance all angular informative is averaged over when calculating a radial density profile. In Chapter 4 we analyze the roles each of these mechanisms play in causing universality by using a combination of numerical and analytic methods.

Chapter 2

Self-Similar Spherical Collapse with Tidal Torque [1]

Abstract

N-body simulations have revealed a wealth of information about dark matter halos however their results are largely empirical. Using analytic means, we attempt to shed light on simulation results by generalizing the self-similar secondary infall model to include tidal torque. In this chapter, we describe our halo formation model and compare our results to empirical mass profiles inspired by N-body simulations. Each halo is determined by four parameters. One parameter sets the mass scale and the other three define how particles within a mass shell are torqued throughout evolution. We choose torque parameters motivated by tidal torque theory and N-body simulations and analytically calculate the structure of the halo in different radial regimes. We find that angular momentum plays an important role in determining the density profile at small radii. For cosmological initial conditions, the density profile on small scales is set by the time rate of change of the angular momentum of particles as well as the halo mass. On intermediate scales, however, $\rho \propto r^{-2}$, while $\rho \propto r^{-3}$ close to the virial radius.

2.1 Introduction

The structure of dark matter halos affects our understanding of galaxy formation and evolution and has implications for dark matter detection. Progress in our understanding of dark matter halos has been made both numerically and analytically.

[1] This chapter is based on the published paper Zukin & Bertschinger 2010a

Analytic treatments began with work by Gunn and Gott; they analyzed how bound mass shells that accrete onto an initially collapsed object can explain the morphology of the Coma cluster (Gunn & Gott, 1972; Gott, 1975) and elliptical galaxies (Gunn, 1977). This continuous accretion process is known as secondary infall.

Secondary infall introduces a characteristic length scale: the shell's turnaround radius r_*. This is the radius at which a particular mass shell first turns around. Since the average density is a decreasing function of distance from the collapsed object, mass shells initially farther away will turnaround later. This characteristic scale should be expected since the radius of a mass shell, like the radius of a shock wave in the Sedov Taylor solution, can only depend on the initial energy of the shell, the background density, and time (Bertschinger, 1985). By imposing that the structure of the halo is self-similar – all quantities describing the halo only depend on the background density, $r_{\rm ta}$ (the current turnaround radius), and lengths scaled to $r_{\rm ta}$ – Bertschinger (1985), and Fillmore & Goldreich (1984), (hereafter referred to as FG) were able to relate the asymptotic slope of the nonlinear density profile to the initial linear density perturbation.

Assuming purely radial orbits, FG analytically showed that the slope ν of the halo density distribution $\rho \propto r^{-\nu}$ falls in the range $2 < \nu < 2.25$ for $r/r_{\rm ta} \ll 1$. This deviates strongly from N-body simulations which find $\nu \lesssim 1$ (Navarro et al., 2010; Graham et al., 2006) or $\nu \sim 1.2$ (Diemand et al., 2004) at their innermost resolved radius and observations of Low Surface Brightness and spiral galaxies which suggest $\nu \sim .2$ (de Blok, 2003) and the presence of cores (Gentile et al., 2004; Salucci et al., 2007; Donato et al., 2009). Though the treatment in FG assumes radial orbits while orbits in simulations and observed galaxies contain tangential components, it is analytically tractable and does not suffer from resolution limits. Numerical dark matter simulations, on the other hand, do not make any simplifying assumptions and have finite dynamic range. Moreover, it is difficult to draw understanding from their analysis and computational resources limit the smallest resolvable radius, since smaller scales require more particles and smaller time steps. It seems natural, then, to generalize the work done by FG in order to explain the features predicted in

simulations and observed in galaxies. This chapter, in particular, investigates how non-radial motion affects the structure of dark matter halos.

Numerous authors have investigated how angular momentum affects the asymptotic density profile. Ryden & Gunn (1987) analyzed the effects of non-radial motion caused by substructure while others have examined how an angular momentum, or a distribution of angular momenta, assigned to each mass shell at turnaround, affects the structure of the halo (Nusser, 2001; Hiotelis, 2002; Williams et al., 2004; Sikivie et al., 1997; Del Popolo, 2009; White & Zaritsky, 1992; Le Delliou & Henriksen, 2003; Ascasibar et al., 2004). Note that many of these authors do not impose self-similarity. Those that do assume that a shell's angular momentum remains constant after turnaround.

This chapter extends previous work by Nusser (2001). Assuming self-similarity, he analytically calculated the structure of the halo in different radial regimes for shells with constant angular momentum after turnaround. He found that the inclusion of angular momentum allows $0 < \nu < 2.25$. According to Hoffman & Shaham (1985), ν depends on the effective primordial power spectral index ($d \ln P / d \ln k$), which varies for different mass halos. For galactic size halos, Nusser's analytic work predicts $\nu \sim 1.3$, in disagreement with simulation results (Navarro et al., 2010; Diemand et al., 2004). In order to address this discrepancy, we extend Nusser's work by including torque. We consistently keep track of a particle's angular momentum, allowing it to build up before turnaround because of tidal interactions with neighboring protogalaxies (Hoyle, 1951) and to evolve after turnaround because of nonlinear effects within the halo. Moreover, we compare the predictions of our halo model to simulation results.

Self-similar secondary infall requires $\Omega_m = 1$ since a nonvanishing Ω_Λ introduces an additional scale. Applying self-similarity to halo formation in the ΛCDM model therefore requires approximations and a mapping to halos in an Einstein de-Sitter universe. We assume that the linear power spectrum and background matter density $\bar{\rho}_m$ today are equal in both universes so that the statistics, masses, and length scales of halos found in the two models are equivalent. Since the scale factor evolves differently

in both universes, the halo assembly histories will differ.

In section 2.2, we define our self-similar system and torqueing parameters. In section 2.3, we set initial conditions and evolve the mass shells before turnaround. In section 2.4, we describe evolution after turnaround and then analyze the asymptotic behavior of the density profile at different scales in section 2.5. In section 2.6, we give numerical results, discuss the overall structure of the halo, and compare to N-body simulations. We conclude in section 2.7.

This chapter requires the use of many equations and symbols. As a guide to the reader, in Table 2.1 we summarize the key symbols and the equations where they are defined or first used.

Table 2.1: Symbols Used in this Chapter

Symbol	Meaning	Reference Equation
r_*	Turnaround radius of an individual shell	...
t_*	Turnaround time of an individual shell	...
$r_{\rm ta}$	Current turnaround radius	...
L	Angular momentum per unit mass	(2.8)
δ	Initial density perturbation	...
β	Exponent characterizing $r_{\rm ta}$	(2.20)
n	Exponent characterizing δ	(2.17)
p	Exponent characterizing correction to δ caused by L	(2.17)
B	Amplitude of L at turnaround	(2.8), (2.30)
γ	Exponent characterizing evolution of L ($t < t_*$)	(2.12)
ϖ	Exponent characterizing evolution of L ($t > t_*$)	(2.12)
λ	Radius scaled to current turnaround radius	...
f	Angular momentum normalized by self-similar scaling	(2.8), (2.12)
$\mathcal{D}$	Density normalized by self-similar scaling	(2.9)
$\mathcal{M}$	Internal mass normalized by self-similar scaling	(2.10)
ξ	Time variable: $\ln(t/t_{ta})$	...
r_a	Apocenter distance of an individual shell	...
r_p	Pericenter distance of an individual shell	...
y	Ratio of pericenter to apocenter distance	(2.41)
y_0	Proportional to first pericenter at turnaround (r_p/r_*)	...
α	Exponent characterizing slope of nonlinear internal mass	(2.37)
q	Exponent characterizing evolution of apocenter distance	(2.38)
l	Exponent characterizing evolution of y	(2.44)

2.2 Self-Similar Definitions

Here we explicitly define our self-similar system and derive constraints on the functional form of the mass distribution within a halo and the angular momentum of particles in a particular shell.

If the infall process is self-similar, then the halo's appearance does not change once all lengths are scaled to the current turnaround radius. For our analysis, we define the current turnaround radius as $r_{\rm ta}(t) \equiv Ct^{\beta}$ where both C and β are positive constants. The exponent β, as we will find, depends on the initial perturbation spectrum.

The evolution of a particular mass shell must depend on time t and the shell's turnaround time t_*. More explicitly, assuming spherical symmetry, we have $r = R(t, t_*)$. We define a self-similar system as one in which every trajectory obeys the following scaling:

$$R(\Lambda t, \Lambda t_*) = \Lambda^{\beta} R(t, t_*) \tag{2.1}$$

where Λ is a constant. The above implies that the trajectory of one mass shell with turnaround time t_1 can be mapped to the trajectory of another mass shell with turnaround time $t_2 = \Lambda t_1$. The exponent β follows since $R(t_1, t_1)/R(t_2, t_2) = (t_1/t_2)^{\beta}$.

Each shell of a self-similar system must also follow the same equation of motion. From Newton's law, the radial equation of motion for a mass shell with angular momentum is given by:

$$\ddot{R}(t, t_*) = -\frac{GM\Big(R(t, t_*), t\Big)}{R^2(t, t_*)} + \frac{L^2\Big(R(t, t_*), t, t_*\Big)}{R^3(t, t_*)} \tag{2.2}$$

where dots denote derivatives with respect to the first argument, M is the mass of the halo interior to r and L is the angular momentum per unit mass of a particle in the shell. Note that we enforce the mass to not depend explicitly on t_*, while the angular momentum can. As we will show below, this is physically motivated. From eq. (2.1), we find:

$$\ddot{R}(\Lambda t, \Lambda t_*) = \Lambda^{\beta-2} R(t, t_*) \tag{2.3}$$

Plugging in eqs. (2.1) and (2.3) into eq. (2.2) and simplifying, we find:

$$\ddot{R}(\Lambda t, \Lambda t_*) = - \Lambda^{3\beta-2} \frac{GM\Big(\Lambda^{-\beta} R(\Lambda t, \Lambda t_*), t\Big)}{R^2(\Lambda t, \Lambda t_*)} + \Lambda^{4\beta-2} \frac{L^2\Big(\Lambda^{-\beta} R(\Lambda t, \Lambda t_*), t, t_*\Big)}{R^3(\Lambda t, \Lambda t_*)} \tag{2.4}$$

Changing variables from $R(t, t_*)$ to $R(t, t_*)/Ct^\beta$ for the mass and angular momentum and rewriting eq. (2.4), we find:

$$\ddot{R}(\Lambda t, \Lambda t_*) = -\Lambda^{3\beta-2} \frac{GM\Big(R(\Lambda t, \Lambda t_*)/C(\Lambda t)^\beta, t\Big)}{R^2(\Lambda t, \Lambda t_*)} + \Lambda^{4\beta-2} \frac{L^2\Big(R(\Lambda t, \Lambda t_*)/C(\Lambda t)^\beta, t, t_*\Big)}{R^3(\Lambda t, \Lambda t_*)} \tag{2.5}$$

Relabeling coordinates and enforcing consistency with eq. (2.2), we find the following constraints on the functional forms of the mass and angular momentum.

$$M\Big(R(t, t_*)/Ct^\beta, t\Big) = \Lambda^{3\beta-2} M\Big(R(t, t_*)/Ct^\beta, t/\Lambda\Big) \tag{2.6}$$

$$L\Big(R(t, t_*), t, t_*\Big) = \Lambda^{2\beta-1} L\Big(R(t, t_*)/Ct^\beta, t/\Lambda, t_*/\Lambda\Big) \tag{2.7}$$

With the above in mind, we define the angular momentum per unit mass L of a particle in a shell at r, and the density ρ and mass M of the halo as follows.

$$L(r, t) = B \frac{r_{\rm ta}^2(t)}{t} f(\lambda, t/t_*) \tag{2.8}$$

$$\rho(r, t) = \rho_B(t) D(\lambda) \tag{2.9}$$

$$M(r, t) = \frac{4\pi}{3} \rho_B(t) r_{\rm ta}^3(t) \mathcal{M}(\lambda) \tag{2.10}$$

where $\lambda \equiv r/r_{\rm ta}(t)$ is the radius scaled to the current turnaround radius and $\rho_B =$

$1/6\pi G t^2$ is the background density for an Einstein de-Sitter (flat $\Omega_m = 1$) universe.

Using eq. (2.1), it is straightforward to show:

$$\lambda(t, \Lambda t_*) = \lambda(t/\Lambda, t_*) \tag{2.11}$$

Eq. (2.11) implies that if one can compute $\lambda(t, t_*)$ for a particular mass shell t_* at all times, then one also knows the position of all other mass shells, labeled by Λt_* with varying Λ, at a particular time. This interpretation is very powerful and will be used later in order to calculate the mass profile after turnaround.

If the mass profile $\mathcal{M}(\lambda)$ also depended explicitly on t_*, then the mass would not have to grow like the background mass enclosed in the current turnaround radius. This is clearly not physical. Hence we suppressed the explicit dependence on t_*. On the other hand, we've kept the dependence on t_* in the angular momentum in order to have this extra freedom. Inspired by tidal torque theory and numerical simulations, in eq. (2.8) we take f to be:

$$f(\lambda, t/t_*) = \begin{cases} \lambda^{-\gamma} & \text{if } t < t_*, \\ (t/t_*)^{\varpi+1-2\beta} & \text{if } t > t_*. \end{cases} \tag{2.12}$$

The constant B sets the amplitude of the angular momentum at turnaround while γ (ϖ) controls how quickly the angular momentum increases before (after) turnaround. Constraints on B, γ, and ϖ will be discussed in later sections.

We've assumed that the halo is spherically symmetric. While simulated halos are triaxial (Hayashi et al., 2007), the description above is meant to represent an average halo. Since there are no preferred directions in the universe, it should be expected that a statistically averaged halo is spherically symmetric.

In the above, L represents the angular momentum per unit mass of all particles in the shell. We impose that all particles in the shell have orbital planes that are randomly distributed. This implies that the total vector angular momentum of the mass shell, and hence the total angular momentum of the halo $\boldsymbol{J}$, vanishes. Hence, while individual particles on a mass shell gain angular momentum in random direc-

tions throughout evolution, on average the mass shell remains spherical. Therefore, like we've assumed above, only one radial equation of motion is necessary to describe the evolution of the shell.

Since our statistically averaged halo has a vanishing total angular momentum, this model cannot address the nonzero spin parameters observed in individually simulated halos (Barnes & Efstathiou, 1987; Boylan-Kolchin et al., 2010). Nor can it reproduce the nonzero value of $\langle J^2 \rangle$ expected from cosmological perturbation theory (Peebles, 1969; White, 1984; Doroshkevich, 1970). However, $\int L^2 dm$ where dm is the mass of a shell, does not vanish for this model. We will use this quantity, which is a measure of the tangential dispersion in the halo, to constrain our torque parameters.

2.3 Before Turnaround

The trajectory of the mass shell after turnaround determines the halo mass profile. In order to start integrating at turnaround, however, the enclosed mass of the halo must be known. For the case of purely radial orbits, the enclosed mass at turnaround can be analytically calculated (Bertschinger, 1985; Fillmore & Goldreich, 1984). For the case of orbits that have a time varying angular momentum, we must numerically evolve both the trajectory and $\mathcal{M}(\lambda)$ before turnaround in order to determine the enclosed mass at turnaround.

The trajectory of a mass shell follows from Newton's law. We have:

$$\frac{d^2 r}{dt^2} = -\frac{GM(r,t)}{r^2} + \frac{L^2(r,t)}{r^3} \tag{2.13}$$

Rewriting eq. (2.13) in terms of λ and $\xi \equiv \log(t/t_i)$, where t_i is the initial time, and plugging in eqs. (2.8), (2.10) and (2.12), we find:

$$\frac{d^2\lambda}{d\xi^2} + (2\beta - 1)\frac{d\lambda}{d\xi} + \beta(\beta - 1)\lambda = -\frac{2}{9}\frac{\mathcal{M}(\lambda)}{\lambda^2} + B^2 \lambda^{-2\gamma - 3} \tag{2.14}$$

The angular momentum before turnaround was chosen so that eq. (2.14) does not explicitly depend on ξ. This allows for a cleaner perturbative analysis. Since r is

an approximate power law in t at early times, we still have the freedom to choose a particular torque model inspired by tidal torque theory. This will be discussed at the end of this section.

In order to numerically solve the above equation, one must know $\mathcal{M}(\lambda)$, a function we do not have a priori. Before turnaround, however, the enclosed mass of a particular shell remains constant throughout evolution since no shells cross. Taking advantage of this, we relate dr/dt to $\mathcal{M}$ by taking a total derivative of eq. (2.10). We find:

$$\left(\frac{dr}{dt}\right)_M = \beta\frac{r}{t} - (3\beta-2)Ct^{\beta-1}\frac{\mathcal{M}}{\mathcal{M}'} \tag{2.15}$$

In the above, a prime represents a derivative taken with respect to λ. Taking another derivative of the above with respect to time, plugging into eq. (2.13) and simplifying, we find an evolution equation for $\mathcal{M}$:

$$\beta(\beta-1)\lambda + (3\beta-2)(\beta-1)\frac{\mathcal{M}}{\mathcal{M}'} - (3\beta-2)^2\frac{\mathcal{M}^2\mathcal{M}''}{(\mathcal{M}')^3} = -\frac{2}{9}\frac{\mathcal{M}}{\lambda^2} + B^2\lambda^{-2\gamma-3} \tag{2.16}$$

Given eqns. (2.14) and (2.16), we must now specify initial conditions when $\lambda \gg 1$. We assume the following perturbative solutions for $D(\lambda)$ and $\lambda(\xi)$ valid at early times. $\mathcal{M}(\lambda)$ follows from eq. (2.10).

$$D(\lambda) = 1 + \delta_1\lambda^{-n} + \delta_2\lambda^{-p} + ... \tag{2.17}$$

$$\mathcal{M}(\lambda) = \lambda^3\left(1 + \frac{3\delta_1}{3-n}\lambda^{-n} + \frac{3\delta_2}{3-p}\lambda^{-p} + ...\right) \tag{2.18}$$

$$\lambda(\xi) = \lambda_0 e^{(2/3-\beta)\xi}(1 + \lambda_1 e^{\alpha_1\xi} + \lambda_2 e^{\alpha_2\xi} + ...) \tag{2.19}$$

In the above, n characterizes the first order correction to the background density. It is related to the FG parameter ϵ through $n = 3\epsilon$. It is also related to the effective power spectral index $n_{\rm eff} = d\ln P/d\ln k$ through $n = n_{\rm eff} + 3$ (Hoffman & Shaham, 1985). Since $n_{\rm eff}$ depends on scale and hence halo mass (Appendix A.1), we have

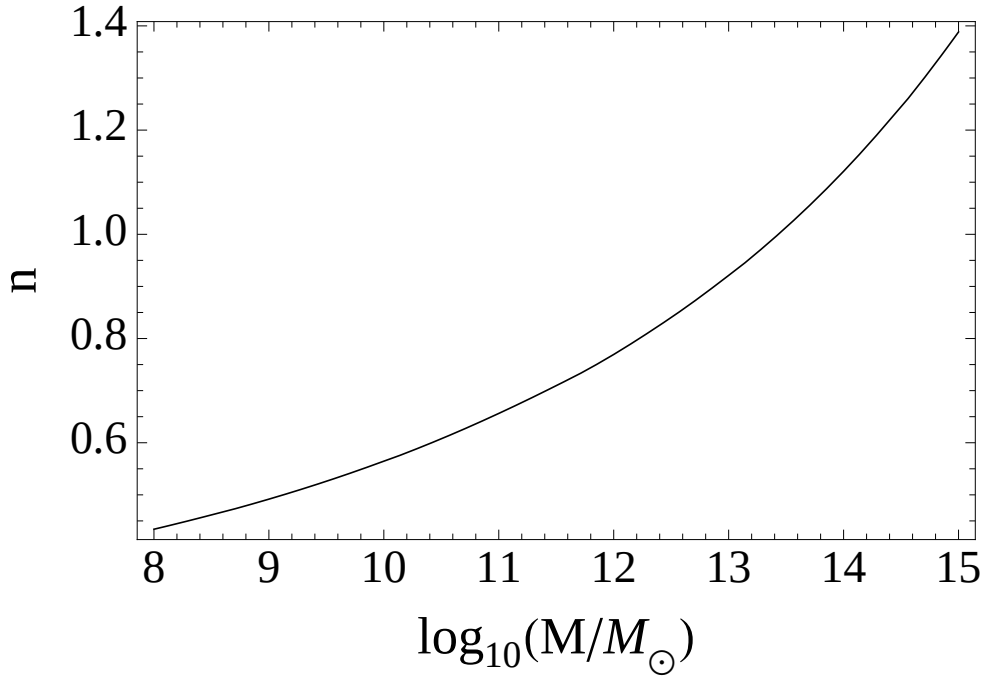

Figure 2-1: The variation of model parameter n with halo mass. Larger mass halos map to steeper initial density profiles.

a relationship between n and halo mass. As Figure 2-1 shows, larger mass halos have larger n. This is expected since larger smoothing lengths imply steeper initial density profiles. As in FG, we restrict $0 < n < 3$ so that the density decreases with radius while the mass increases. We examine this whole range for completeness even though $n > 1.4$ corresponds to objects larger than galaxy clusters. The exponent p characterizes the next order correction to the background density caused by angular momentum. Consistency with our perturbative expansion (eqs. 2.17 through 2.19) demands that we take $n < p < 2n$. However, it is straightforward to generalize to other cases (Section 2.3.1). As we show below, the constants $\{\delta_2, \lambda_1, \lambda_2, \alpha_1, \alpha_2\}$ are set by the equations of motion. The constants $\{\delta_1, \lambda_0\}$ are set by boundary conditions. Plugging eq. (2.18) into eq. (2.16) and enforcing equality between terms proportional to λ^{1-n} we find two possible solutions.

$$\beta = \frac{2}{3}\left(1+\frac{1}{n}\right) \tag{2.20}$$

$$\beta = \frac{2}{3}\left(1-\frac{3}{2n}\right) \tag{2.21}$$

These represent the two solutions to the second order differential equation (eq. 2.16). For the first case, the turnaround radius grows faster than the Hubble flow while for the second it grows slower. Hence, the first solution represents the growing mode of the perturbation while the second is the decaying mode. Since we are interested in the growth of halos, we will only consider the growing mode from now on. Next, imposing $p = 2\gamma + 4$ and enforcing equality between terms proportional to λ^{1-p} in eq. (2.16), we find:

$$\delta_2 = \frac{9n^2B^2(p-3)}{2(p-n)(3n+2p)} \tag{2.22}$$

Comparing eqs. (2.18) and (2.22), we see that the correction to the initial mass caused by angular momentum is negative since $p > n$. This is expected since the angular momentum acts against gravity.

Next, we find constraints for the parameters in eq. (2.19). Plugging in eq. (2.19) into eq. (2.14) and setting terms linear in δ_1, δ_2, λ_1, and λ_2 equal to each other, we find:

$$\alpha_1 = \frac{2}{3} \tag{2.23}$$

$$\lambda_1 = \frac{\delta_1}{n-3}\lambda_0^{-n} \tag{2.24}$$

$$\alpha_2 = p\left(\beta-\frac{2}{3}\right) \tag{2.25}$$

$$\lambda_2 = \frac{\delta_2}{p-3}\lambda_0^{-p} \tag{2.26}$$

Eqns. (2.17) through (2.26) set the initial conditions for eqs (2.14) and (2.16). We

evolve λ and $\mathcal{M}$ and choose $\{\lambda_0, \delta_1\}$ such that turnaround occurs ($d\lambda/d\xi = -\lambda\beta$) when $\lambda = 1$. The free parameters for evolution before turnaround are $\{n, B, p\}$. For the zero angular momentum case analyzed in FG, the enclosed mass is the same regardless of n; $\mathcal{M}(1) = (3\pi/4)^2$. Including torque, however, we find that the enclosed mass depends on the parameters B and p. Figure 2-2 shows a contour plot of $16\mathcal{M}(1)/9\pi^2$ for $n = 1$. As expected, the enclosed mass at turnaround must be larger than the no-torque case in order to overcome the additional angular momentum barrier. B sets the amplitude of the angular momentum while p controls how the angular momentum grows in comparison to the mass perturbation. Larger B and smaller p correspond to stronger torques on the mass shell. Contour plots with different values of n give the same features.

The above perturbative scheme ensures that the inclusion of angular momentum preserves cosmological initial conditions. Analyzing eq. (2.19) for $\xi \to -\infty$, and using eqs. (2.23) and (2.25), we see that since $p > n$, the angular momentum correction is subdominant to the density perturbation correction. More importantly, at early times, the shell moves with the Hubble flow. Last, in order to be consistent with cosmological initial conditions, the angular momentum of particles within a mass shell must vanish at early times. Imposing $r \propto t^{2/3}$, and plugging into eq. (2.8), we find that $L \propto t^{(1+p/n)/3}$. Hence, for all values of p we consider, the angular momentum vanishes at early times and has a value of Br_*^2/t_* at turnaround. Note that shells which turn around later have larger angular momentum.

2.3.1 Tidal Torque Theory

According to Hoyle's tidal torque mechanism, mass shells before turnaround gain angular momentum through their interactions with the tidal fields of neighboring protogalaxies (Hoyle, 1951). Peebles (1969) claimed that the angular momentum of protogalaxies in an Einstein de-Sitter universe grows as $t^{5/3}$ while Doroshkevich (1970) showed that for non-spherical regions, the angular momentum grows as t. White (1984) confirmed Doroshkevich's analysis with N-body simulations. Since the net angular momentum of our model's halo vanishes, we will instead use $\tilde{\sigma}^2$, defined

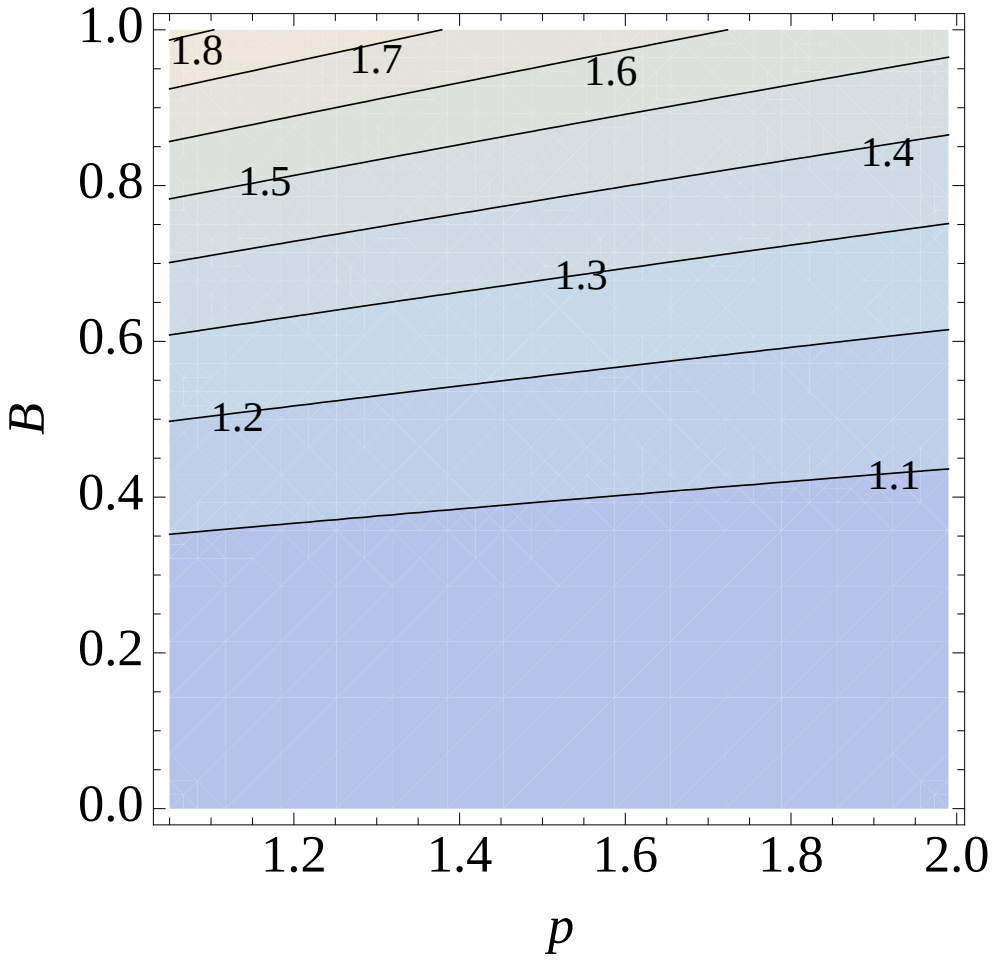

Figure 2-2: Contour plot of $16\mathcal{M}(1)/9\pi^2$ for $n = 1$ as a function of torquing parameters B and p. Smaller p and larger B result in larger torques on the mass shell. These larger torques require bigger enclosed masses at turnaround, in order to counteract the stronger angular momentum barrier.

below, to constrain p and B.

$$\tilde{\sigma}^2 \equiv \int_{V_L} dm |(\boldsymbol{r} - \boldsymbol{r}_0) \times (\boldsymbol{v} - \boldsymbol{v}_0)|^2 \tag{2.27}$$

In the above, we integrate over the Lagrangian volume V_L of the halo, $\boldsymbol{r}$ and $\boldsymbol{v}$ are the physical radius and velocity of particles within the halo, $\boldsymbol{r}_0$ is the center of mass of the halo and $\boldsymbol{v}_0 \equiv \boldsymbol{v}(\boldsymbol{r}_0)$. As described earlier in this section, $\lambda \gg 1$ corresponds to early times when the halo is linear. Therefore, since our model represents a statistically averaged halo, we can calculate $\langle\tilde{\sigma}^2\rangle$ using cosmological linear perturbation theory

and compare to expectations from our model.

Using the Zel'dovich approximation (Zel'dovich, 1970), assuming a spherical Lagrangian volume with radius R, and working to first order, we find:

$$\left\langle \tilde{\sigma}^2 \right\rangle_M = 6a^4 \dot{D}^2 M x_{\max}^2 A^2(R) \tag{2.28}$$

where M is the mass of the halo, a is the scale factor, D is the linear growth factor, dots denote derivatives with respect to proper time, $x_{\max}$ is the lagrangian radius of the volume, R is the spherical top hat radius for a halo of mass M and $A(R)$ is a time independent function defined in Appendix A.2 which has units of length. Note that the scale factor a and $\dot{D}$ are the only quantities which vary with time. For a matter dominated universe, $(\langle \tilde{\sigma}^2 \rangle_M)^{1/2} \propto t$, just as in the White analysis. This is expected since the Lagrangian mass is time independent.

Next we calculate eq. (2.27) from the perspective of our model. Using eqns. (2.8), (2.10), and (2.12) and assuming first order corrections to M are negligible, we find:

$$\tilde{\sigma}^2 = \int_{r_{\min}}^{r_{\max}} B^2 \frac{r_{ta}^4}{t^2} \lambda^{-2\gamma} \frac{\partial M(r,t)}{\partial r} dr = \frac{4\pi}{3-2\gamma} \frac{B^2 \rho_B(t) r_{ta}^7(t)}{t^2} \left[\lambda_{\max}^{3-2\gamma}(t) - \lambda_{\min}^{3-2\gamma}(t) \right] \tag{2.29}$$

The lower limit of integration sets an effective smoothing length which we choose to be $\lambda \gg 1$ so that we only count shells that are still described by linear theory. The upper limit of integration is required since all the mass in the universe does not go into the halo. Since $p = 2\gamma + 4$ and $n < p < 2n$, then for the range of n we consider, $2\gamma < 3$ and the angular momentum of the protogalaxy is dominated by shells close to $r_{\max}$. Equating eqs. (2.28) and (2.29) and assuming the first order corrections to $r_{\max}$ in eq. (2.19) are negligible, we find $p = 2n$ and:

$$B = \frac{2}{3} \sqrt{2(7-2n)} \mathcal{M}(1)^{(n-1)/3} \frac{A(R)}{R} \tag{2.30}$$

Eqs. (2.28) and (2.30) are derived in Appendix A.2. Note that the perturbative

analysis, presented above, which is used to calculate $\mathcal{M}(1)$ is not valid for $p = 2n$. Redoing the analysis for this special case, we find:

$$\alpha_2 = \frac{4}{3} \tag{2.31}$$

$$\delta_2 = \frac{9}{14}B^2(2n-3) + \frac{(7n-17)(2n-3)}{7(n-3)^2}\delta_1^2 \tag{2.32}$$

$$\lambda_2 = \frac{9}{14}\lambda_0^{-2n}\left(B^2 - \frac{2}{3}\frac{\delta_1^2}{(n-3)^2}\right) \tag{2.33}$$

For the remainder of this chapter we impose $p = 2n$, so that angular momentum grows in accordance with cosmological perturbation theory, and set n according to the halo mass. Unfortunately, when comparing to N-body simulations (Section 2.6.1), eq. (2.30) overestimates the angular momentum of particles at turnaround by a factor of 1.5 to 2.3. We discuss possible reasons for this discrepancy in Appendix A.2. For convenience, $B_{1.5}$ ($B_{2.3}$) denotes B calculated using eq. (2.30) with the right hand side divided by 1.5 (2.3). As described above, $\mathcal{M}(1)$ in eq. (2.30) depends on B. Therefore, in order to find B, we calculate B and $\mathcal{M}(1)$ iteratively until eq. (2.30) is satisfied.

The relationship between n and $n_{\rm eff}$ as well as tidal torque theory implies that $\{n, p, B\}$ are all set by the halo mass. Figure 2-3 shows the variation of B with halo mass. $A(R)$ increases with halo mass since more power at large scales is included; R also increases with halo mass. These two competing effects cause a slight variation in B over seven orders of magnitude in halo mass.

2.4 After Turnaround

Given the enclosed mass found at turnaround, we now solve for the trajectory and mass profile after turnaround. For convenience, we redefine the time variable to be $\xi \equiv \ln(t/t_{ta})$, where t_{ta} is the current turnaround time. The trajectory's evolution equation after turnaround, with the appropriate torque model (eq. 2.12), is shown

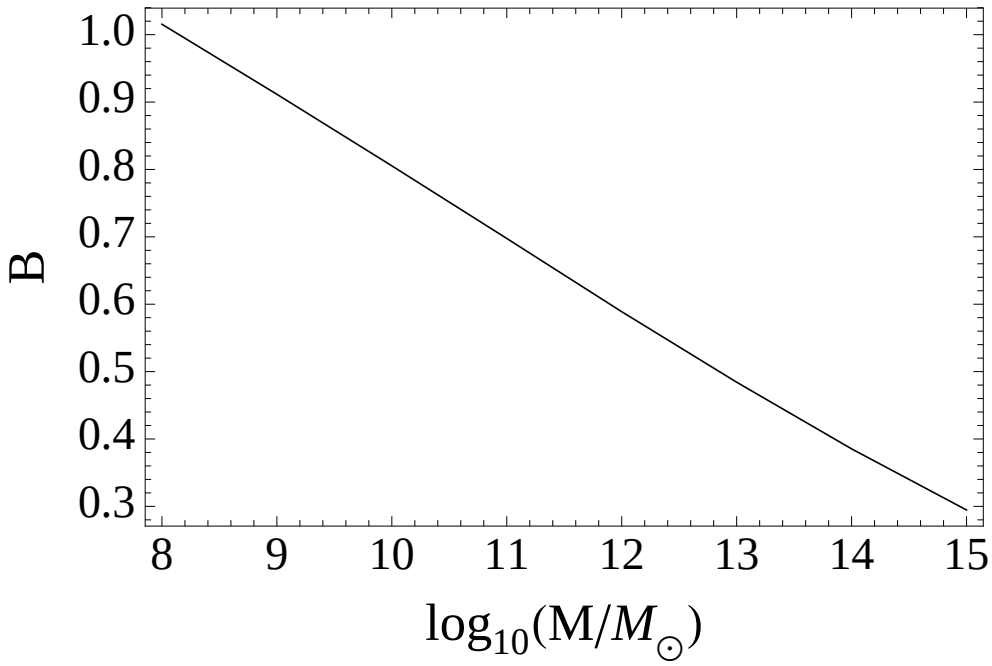

Figure 2-3: The variation of model parameter B with halo mass. B sets the angular momentum of particles at turnaround.

below.

$$\frac{d^2\lambda}{d\xi^2} + (2\beta - 1)\frac{d\lambda}{d\xi} + \beta(\beta - 1)\lambda = -\frac{2}{9}\frac{\mathcal{M}(\lambda)}{\lambda^2} + \frac{B^2}{\lambda^3}e^{2(\varpi+1-2\beta)\xi} \tag{2.34}$$

The torque model after turnaround was chosen to not explicitly depend on r, since r begins to oscillate on a much faster timescale than the growth of the halo. Nusser (2001) and Sikivie et al. (1997) focused on the case $\varpi = 0$. However, as was discussed before, this results in density profiles steeper than what is predicted by numerical simulations.

There are a number of dynamical processes that can cause a particle's angular momentum to evolve after turnaround. Dynamical friction (Chandrasekhar, 1943) transfers the angular momentum of massive bound objects – like black holes, globular clusters and merging satellite galaxies – to the background halo. A massive black hole at the center of the halo that dominates the potential at small scales tends to make the velocity dispersion isotropic (Gerhard & Binney, 1985; Merritt & Quinlan, 1998; Cruz et al., 2007). Bars (Kalnajs, 1991; Dehnen, 2000) and supermassive black

hole binaries (Milosavljević & Merritt, 2003; Sesana et al., 2007) are also expected to perturb the dark matter velocity distribution. While the torque model proposed after turnaround is clearly very simplistic and may not accurately describe some of the above phenomena, it still allows us to get intuition for how torques acting on mass shells change the structure of the halo.

Analytically calculating ϖ is difficult since the halo after turnaround is nonlinear. In Appendix A.3, we show in a simplistic manner how ϖ is sourced by substructure and argue that dark matter dominated substructure should cause steeper density profiles than baryon dominated substructure. In order to properly constrain ϖ, N-body simulations are required. This is beyond the scope of this work.

The initial conditions for eq. (2.34), enforced in the above section, are $\lambda(\xi = 0) = 1$ and $d\lambda/d\xi(\xi = 0) = -\beta$. As discussed before, self-similarity implies that all mass shells follow the same trajectory $\lambda(\xi)$. Hence, $\lambda(\xi)$ can either be interpreted as labeling the location of a particular mass shell at different times, or labeling the location of all mass shells at a particular time. We take advantage of the second interpretation in order to calculate the mass profile.

After turnaround, shells cross since dark matter is collisionless. Therefore, the mass interior to a particular shell does not stay constant. However, since $\lambda(\xi)$ specifies the location of all mass shells at a particular time, the mass interior to a given scale is simply the sum of all mass shells interior to it. The mass profile is then given by (Bertschinger, 1985; Fillmore & Goldreich, 1984):

$$\begin{aligned} \mathcal{M}(\lambda) &= \frac{2}{n}\mathcal{M}(1)\int_0^\infty d\xi \exp[-(2/n)\xi]H[\lambda - \lambda(\xi)] \\ &= \mathcal{M}(1)\sum_i (-1)^{i-1}\exp[-(2/n)\xi_i] \end{aligned} \tag{2.35}$$

where $\mathcal{M}(1)$ is the normalization constant found in the prior section, $H[u]$ is the Heaviside function, and ξ_i is the ith root that satisfies $\lambda(\xi) = \lambda$. The above is straightforward to interpret. The roots ξ_i label shell crossings at a particular scale and the exponential factor accounts for the mass difference between shells that turn

around at different times.

Since the trajectory and the mass profile depend on each other, it is necessary to first assume a mass profile, then calculate the trajectory from eq. (2.34) and resulting mass profile from eq. (2.35) and repeat until convergence is reached.

The density profile $D(\lambda)$ is straightforward to derive using eqs. 2.9, 2.10 and 2.35. We find (Bertschinger, 1985; Fillmore & Goldreich, 1984):

$$D(\lambda) = \frac{1}{3\lambda^2}\frac{d\mathcal{M}}{d\lambda} = \frac{2}{3n}\frac{\mathcal{M}(1)}{\lambda^2}\sum_i (-1)^i \exp[-(2/n)\xi_i]\left(\frac{d\lambda}{d\xi}\right)_i^{-1} \tag{2.36}$$

2.5 Asymptotic Behavior

Unlike N-body experiments, self-similar systems are not limited by resolution. One can analytically infer the asymptotic slope of the mass profile close to the origin. FG did this by taking advantage of adiabatic invariance, self-consistently calculating the mass profile, and analyzing the limit of the mass profile as $\lambda \to 0$. Below, we generalize their analysis to the case of particles with changing angular momentum. Unlike Nusser (Nusser, 2001), we do not restrict our analysis to the case $\varpi = 0$.

Just as in FG, we start by parameterizing the halo mass and the variation of the apocenter distance r_a.

$$M(r,t) = \kappa(t) r^\alpha \tag{2.37}$$

$$\frac{r_a}{r_*} = \left(\frac{t}{t_*}\right)^q \tag{2.38}$$

In the above r_* is the turnaround radius of a mass shell which turns around at t_*. It is possible to relate q and α to n by taking advantage of adiabatic invariance. The equation of motion for the mass shell is:

$$\frac{d^2 r}{dt^2} = -G\kappa(t) r^{\alpha-2} + \frac{L^2(t)}{r^3} \tag{2.39}$$

At late times, the orbital period is much smaller than the time scale for the mass

and angular momentum to grow. Taking $\kappa(t)$ and $L(t)$ to stay roughly constant over an orbit and integrating the above equation, we find the energy equation:

$$\left(\frac{dr}{dt}\right)^2 = \frac{2G\kappa(t)}{\alpha-1}(r_a^{\alpha-1} - r^{\alpha-1}) - L^2(t)(r^{-2} - r_a^{-2}) \tag{2.40}$$

The above relationship tells us how the pericenters r_p evolve with time. Note that we only consider torquing models (eq. 2.12) which give rise to bound orbits. This restriction on ϖ will be discussed below. Defining $y \equiv r_p/r_a$ and evaluating the above at $r = r_p$, we find:

$$\frac{1-y^{\alpha-1}}{y^{-2}-1} \equiv A(y) = \frac{(\alpha-1)L^2(t)}{2G\kappa(t)r_a^{\alpha+1}(t)} \tag{2.41}$$

For $\varpi > (<)\ 0$, the angular momentum of particles in the mass shell increases (decreases). This gives rise to pericenters that increase (decrease). Hence at late times, the orbit of a mass shell with increasing angular momentum will circularize and have $y \sim 1$, while the orbit of a mass shell with decreasing angular momentum will become more radial, with $y \ll 1$. With this in mind, we can now calculate the radial action in order to find how q relates to n and α. The radial action is given by:

$$\begin{aligned} J &= 2\int_{r_p}^{r_a} dr \left(\frac{dr}{dt}\right) \\ &= 2\left(\frac{2G\kappa(t)}{\alpha-1}\right)^{1/2} r_a^{(\alpha+1)/2} \int_{y(t)}^{1} du \left[(1-u^{\alpha-1}) - A(y)(u^{-2}-1)\right]^{1/2} \end{aligned} \tag{2.42}$$

In the above we've assumed $\alpha > 1$. Generalizing to the case $\alpha < 1$ is straightforward. The special case $\alpha = 1$ will be addressed later. For $y(t) \ll 1$, the above integral is dominated by the region in which $y(t) \ll u \ll 1$. Over this region, the integrand is time independent and hence the same for all orbits. Therefore adiabatic invariance implies $\kappa(t)r_a^{\alpha+1} = \text{const}$. For $y(t) \sim 1$, the orbit is circular, which implies the radial action vanishes and $L^2(t) = G\kappa(t)r_a^{\alpha+1}$. Using eq. (2.38), and noting that $\kappa(t) \propto t^s$ where $s = 3\beta - 2 - \alpha\beta$, we find at late times:

$$q = \begin{cases} \frac{1}{\alpha+1}\{2\varpi + \frac{2}{3n}[\alpha(1+n)-3]\} & \text{if } \varpi \geq 0 \\ \frac{2}{3n(\alpha+1)}\left[\alpha(1+n)-3\right] & \text{if } \varpi < 0 \end{cases} \tag{2.43}$$

For the specific case, $\varpi < 0$, taking advantage of $y \ll 1$, the adiabatic invariance arguments above, and eqs. (2.8) and (2.12), we can rewrite eqn. (2.41) in the form $y(t, t_*) = y_0(t/t_*)^l$, where:

$$l = \begin{cases} \varpi & \text{if } \alpha > 1, \\ 2\varpi/(\alpha+1) & \text{if } \alpha < 1. \end{cases} \tag{2.44}$$

and $y_0 r_*$ is the pericenter of a mass shell at turnaround. Constant angular momentum after turnaround corresponds to $\varpi = 0$. This case was addressed analytically in (Nusser, 2001) and numerically in (Sikivie et al., 1997).

We next take advantage of the functional form of the mass profile. Following FG, we define $P(r/r_a, y)$ to be the fraction of time a particle with apocenter distance r_a and pericenter yr_a, at a particular time t, spends inside r.

$$\begin{aligned} P(v,y) &= 0 \qquad (v < y) \\ P(v,y) &= \frac{I(v,y)}{I(1,y)} \quad (y < v \leq 1) \\ P(v,y) &= 1 \qquad (v > 1) \end{aligned} \tag{2.45}$$

where

$$I(v,y) \equiv \begin{cases} \int_y^v \frac{du}{((1-u^{\alpha-1})-A(y)(u^{-2}-1))^{1/2}} & \text{if } \alpha > 1, \\ \int_y^v \frac{du}{((u^{\alpha-1}-1)+A(y)(u^{-2}-1))^{1/2}} & \text{if } \alpha < 1. \end{cases} \tag{2.46}$$

We see that the presence of pericenters causes the new case $v < y$, which did not exist in the FG analysis. Self consistency demands that

$$\left(\frac{r}{r_{\rm ta}}\right)^{\alpha} = \frac{M(r,t)}{M(r_{\rm ta},t)} = \int_0^{M_{ta}} \frac{dM_*}{M_{ta}} P\left(\frac{r}{r_a(t,t_*)}, y(t,t_*)\right) \tag{2.47}$$

where M_* is the mass internal to a shell that turns around at t_* and M_{ta} is the current turnaround mass. The integral assigns a weight to each shell depending on how often that shell is below the scale r. Noting from eq. (2.10) that

$$M_* = M_{ta}\left(\frac{t_*}{t}\right)^{3\beta-2}, \tag{2.48}$$

using eq. (2.38) and transforming integration variables, we find:

$$\left(\frac{r}{r_{\rm ta}}\right)^{\alpha-k} = k\int_{r/r_{\rm ta}}^{\infty}\frac{du}{u^{1+k}}P\left(u, y(t,t_*)\right) \tag{2.49}$$

where

$$k = \frac{6}{2+n(2-3q)} \tag{2.50}$$

As u increases, the above integral sums over shells with smaller t_*. Since the pericenter of a shell evolves with time, the second argument of P depends on u. The dependence, as we showed, varies with torque model (sign of ϖ); hence we've kept the dependence on u implicit. Next we analyze the above for certain regimes of $r/r_{\rm ta}$, and certain torquing models, in order to constrain the relationship between α and k.

2.5.1 Inner Solution; Negative Torque

For $\varpi < 0$, particles lose angular momentum over time. When probing scales $r/r_{\rm ta} \ll y_0$, mass shells with $t_* \ll t_{ta}$ only contribute. As a result, $y(t,t_*) \ll 1$. Using eq. (2.44), we then find:

$$y(t,t_*) = y_0\left(\frac{t}{t_*}\right)^{l} = y_0\left(\frac{r}{ur_{\rm ta}}\right)^{\delta} \tag{2.51}$$

where $\delta \equiv l/(q-\beta)$. For bound mass shells, $q-\beta < 0$. Therefore, since $\delta > 0$, the first argument of P in eq. (2.49) increases while the second decreases as we sum over shells that have turned around at earlier and earlier times ($u \to \infty$). For $r/r_{\rm ta} \ll y_0$, mass shells which most recently turned around do not contribute to the mass inside $r/r_{\rm ta}$ since we are probing scales below their pericenters. Mass shells only begin to

contribute when the two argument of P are roughly equal to each other. This occurs around:

$$u = y_1 \equiv \left(y_0 (r/r_{\rm ta})^\delta\right)^{1/(1+\delta)} \tag{2.52}$$

Hence, we can replace the lower limit of integration in eq. (2.49) with y_1. We next want to calculate the behavior of eq. (2.49) close to y_1 in order to determine whether the integrand is dominated by mass shells around y_1 or mass shells that have turned around at much earlier times. The first step is to calculate the behavior of $P(u, y)$ for $u \approx y$. We find:

$$P(u, y) \propto u^{1/2}(1 - y/u)^{1/2} \times \begin{cases} y^{1/2} & \text{if } \alpha > 1, \\ y^{1-\alpha/2} & \text{if } \alpha < 1. \end{cases} \tag{2.53}$$

Given the above, we evaluate the indefinite integral in eq. (2.49), noting that y is a function of u (eq. 2.51). For $u \sim y_1$, we find:

$$\int \frac{du}{u^{1+k}} P\left(u, y_0 \left(\frac{r}{u r_{\rm ta}}\right)^\delta\right) \propto (u/y_1 - 1)^{3/2} \begin{cases} y_1^{1-k} & \text{if } \alpha > 1, \\ y_1^{3/2-k-\alpha/2} & \text{if } \alpha < 1. \end{cases} \tag{2.54}$$

Now comes the heart of the argument. Following the logic in FG, if we keep u/y_1 fixed and the integrand blows up as $r/r_{\rm ta} \to 0$, then the left hand side of eq. (2.49) must diverge in the same way as the right hand side shown in eq. (2.54). Therefore, using eq. (2.52):

$$\alpha - k = \begin{cases} \delta(1-k)/(1+\delta) & \text{if } \alpha > 1, \\ \delta(3/2 - k - \alpha/2)(1+\delta) & \text{if } \alpha < 1. \end{cases} \tag{2.55}$$

Otherwise, if the right hand side converges, then the integrand will not depend on $r/r_{\rm ta}$ as $r/r_{\rm ta} \to 0$. Therefore, the left hand side cannot depend on $r/r_{\rm ta}$ either, which implies $\alpha = k$. Solving the above system of equations for α given eqs. (2.43)

and (2.50) and making sure the solution is consistent, (ie: using eq. (2.55) only if the integrand diverges), we find:

$$\begin{aligned}
\text{For } n &\leq 2: \\
\alpha &= \frac{1+n-\sqrt{(1+n)^2+9n\varpi(n\varpi-2)}}{3n\varpi} \\
k &= \frac{1+n+3n\varpi-\sqrt{(1+n)^2+9n\varpi(n\varpi-2)}}{n\varpi(4+n)} \\
q &= \frac{1+n-3n\varpi-\sqrt{(1+n)^2+9n\varpi(n\varpi-2)}}{3n} \\
\text{For } n &\geq 2: \\
\alpha &= k = \frac{3}{1+n}\,, \quad q = 0
\end{aligned} \tag{2.56}$$

The above solutions are continuous at $n = 2$. Moreover, taking the no-torque limit ($\varpi \to 0$) for $n \leq 2$ gives the same solutions as $n \geq 2$, which is consistent with analytic and numeric results from (Nusser, 2001; Sikivie et al., 1997). Taking the limit, $\varpi \to -\infty$ reproduces the FG solution, as expected, since the shell loses its angular momentum instantly. The solution for $n \geq 2$ is independent of ϖ. This is because the mass is dominated by shells with turnaround time $t_* \ll t_{ta}$ which have effectively no angular momentum. In other words, for $\varpi < 0$, the solution should only depend on torquing parameters when the mass is dominated by shells that have turned around recently.

2.5.2 Inner Solution; Positive Torque

For $\varpi > 0$, the angular momentum of particles increase with time. As mentioned above, when probing scales $r/r_{\rm ta} \ll y_0$, mass shells with $t_* \ll t_{ta}$ only contribute. As a result, $y(t, t_*) \sim 1$. In other words, the orbits are roughly circular. We can therefore replace the lower limit of integration in eq. (2.49) with 1 since mass shells will only start contributing to the sum when $u \sim y \sim 1$. Hence, the right hand side of eq. (2.49) does not depend on $r/r_{\rm ta}$, which implies $\alpha = k$. Using eq. (2.43) and

(2.50), we find:

$$\alpha = k = \frac{3}{1+n-3n\varpi}\,, \quad q = 2\varpi\,, \qquad \text{for } 0 \leq n \leq 3 \tag{2.57}$$

The no torque case, $\varpi = 0$, is consistent with the analysis in the prior subsection. The singularity $\varpi = (1+n)/3n$ implies $q = \beta$. This physically corresponds to the orbital radius of mass shells increasing at the same rate as the turnaround radius and results in orbits that are not bound and a cored profile where there are no particles internal to a particular radius. This breaks the assumption of a power law mass profile (eq. 2.37); hence we only consider $\varpi < (1+n)/3n$.

Unlike the Nusser solution, certain parameters give $\alpha > 3$, which corresponds to a density profile which converges as $r \to 0$. Since the angular momentum acts like a heat source $d\rho/dr > 0$ is dynamically stable and physical.

2.5.3 Outer Solution

In this regime, we are probing scales larger than the pericenters of the most recently turned around mass shells. As a result, $P(u, y)$ is dominated by the contribution from the integrand when $u \gg y$. Therefore:

$$P(u,y) \propto \begin{cases} u & \text{if } \alpha > 1, \\ u^{(3-\alpha)/2} & \text{if } \alpha < 1. \end{cases} \tag{2.58}$$

Hence the integral in eq. (2.49) becomes:

$$\int \frac{du}{u^{1+k}} P\left(u, y(t, t_*)\right) \propto \begin{cases} u^{1-k} & \text{if } \alpha > 1, \\ u^{3/2-k-\alpha/2} & \text{if } \alpha < 1. \end{cases} \tag{2.59}$$

Following the logic in the prior section, if the integral diverges as $r/r_{\rm ta} \to 0$, then we set the exponents on the left hand side and right hand side equal to each other so that both sides diverge in the same way. If the integral converges, then the left

hand side cannot depend on $r/r_{\rm ta}$, which implies $\alpha = k$. Given these arguments, and imposing consistency with the above inequalities on α to find the appropriate ranges for n, we find:

$$\begin{aligned} \alpha &= 1\,, \quad k = \frac{6}{4+n}\,, \quad q = \frac{n-2}{3n}\,, \quad \text{for } n \leq 2 \\ \alpha &= k = \frac{3}{1+n}\,, \quad q = 0\,, \qquad\qquad\quad \text{for } n \geq 2 \end{aligned} \tag{2.60}$$

The above is exactly the FG solution. We expect to recover these solutions since we are probing scales larger than the pericenters of the most massive shells, where the angular momentum does not affect the dynamics.

This section assumed $\alpha \neq 1$ and yet, for certain parts of parameters space, eqs. (2.56), (2.57) and (2.60) give $\alpha = 1$. However, since the solutions are continuous as $\alpha \to 1$ from the left and right, then the results hold for $\alpha = 1$ as well.

2.6 Structure of the Halo

In this section, we discuss the radial structure of galactic size halos and compare directly to numerical N-body simulations. Note however, that the mass of a halo is not well defined when our model is applied to cosmological structure formation since it is unclear how the spherical top hat mass which characterizes the halo when it is linear relates to the virial mass which characterizes the halo when it is nonlinear. For halos today with galactic size virial masses, we assume the model parameter n which characterizes the initial density field, is set by a spherical top hat mass of $10^{12} M_{\odot}$. As described in prior sections, specifying the top hat mass also sets model parameters B and p. Before comparing directly to N-body simulations, we first describe how ϖ influences the halo.

Figure 2-4 shows the mass $\mathcal{M}(\lambda)$ and density profiles $D(\lambda)$ for galactic size halos $\{n = 0.77, p = 2n, B_{1.5} = 0.39\}$ with varying ϖ. The spikes in the density profile are caustics which form at the shell's turning points. They form because of unphysical

initial conditions; we assume each shell has zero radial velocity dispersion. The structure of the halos naturally break down into three different regions. The dividing points between these regions are roughly the virial radius (r_v) and $y_0 r_{\rm ta}$, the pericenter of the mass shell which most recently turned around.

As in dark matter N-body simulations, we associate the virial radius with r_{200}, the radius at which $M(r_{200}) = 800\pi\rho_B r_{200}^3/3$ is satisfied. Numerically, we find that the virial radius occurs near the first caustic ($\lambda \sim .18$). For $r > r_v$, the mass profile flattens and then starts to increase. The flattening is equivalent to what is seen on large scales in N-body simulations where $\rho \propto r^{-3}$. The mass profile then starts to increase again because at large radii, where $\lambda \gg 1$, the density is roughly constant, which implies $\mathcal{M} \propto \lambda^3$. For $r \sim r_v$, it is difficult to make analytic predictions for the mass profile because adiabatic invariance breaks down. In other words, the mass of the halo and angular momentum of a shell change on the same time scale as the shell's orbital period.

As discussed in the prior section, for $y_0 r_{\rm ta} \ll r \ll r_v$, we can take advantage of adiabatic invariance to infer the logarithmic slope of the mass profile. Since this regime probes a scale much larger than the pericenters of the mass shells, the angular momentum does not affect the dynamics and we recover the FG solution. For our particular choice of $n = 0.77$, this gives an isothermal profile with $\rho \propto r^{-2}$. However, since $n < 2$ for all collapsed objects today (Figure 2-1) and based on the results of FG, our model predict that all halos are isothermal in this regime.

Last, for $r/r_{\rm ta} \ll y_0$, angular momentum begins to play a role and the halo starts to exhibit different features than the FG solution. The behavior is very intuitive. The mass of a particular shell does not contribute to the internal mass when probing radii less than the pericenter of that mass shell. Therefore, as one probes radii smaller than the pericenter of the most recently turned around mass shell, one expects a steeper fall off than the FG solution, since less mass is enclosed interior to that radius. Moreover, varying ϖ varies the pericenter of mass shells over time. Increasing (decreasing) angular momentum, $\varpi > (<)\ 0$, causes the pericenters to increase (decrease) over time. This results in profiles which are steeper (shallower) than the no-torque case.

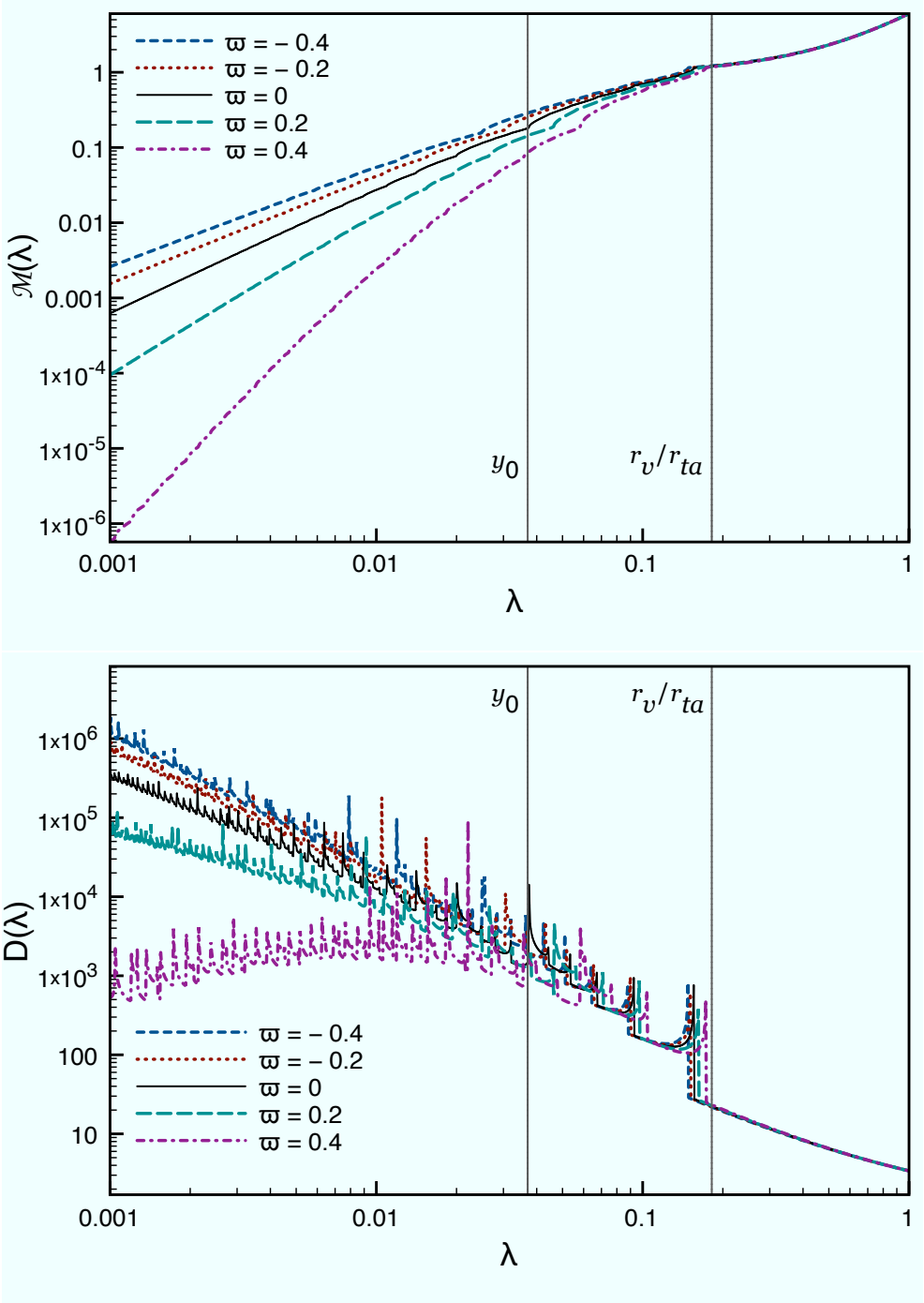

Figure 2-4: The mass and density profiles for galactic size halos $\{n = 0.77, p = 2n, B_{1.5} = 0.39\}$ with varying ϖ. The value of ϖ changes how pericenters evolve with time and thereby affects how many shells at a particular scale contribute to the internal mass. The above numerically computed profiles match analytic predictions. The virial radius (r_v) and first pericenter passage ($y_0 r_{ta}$) are labeled for clarity.

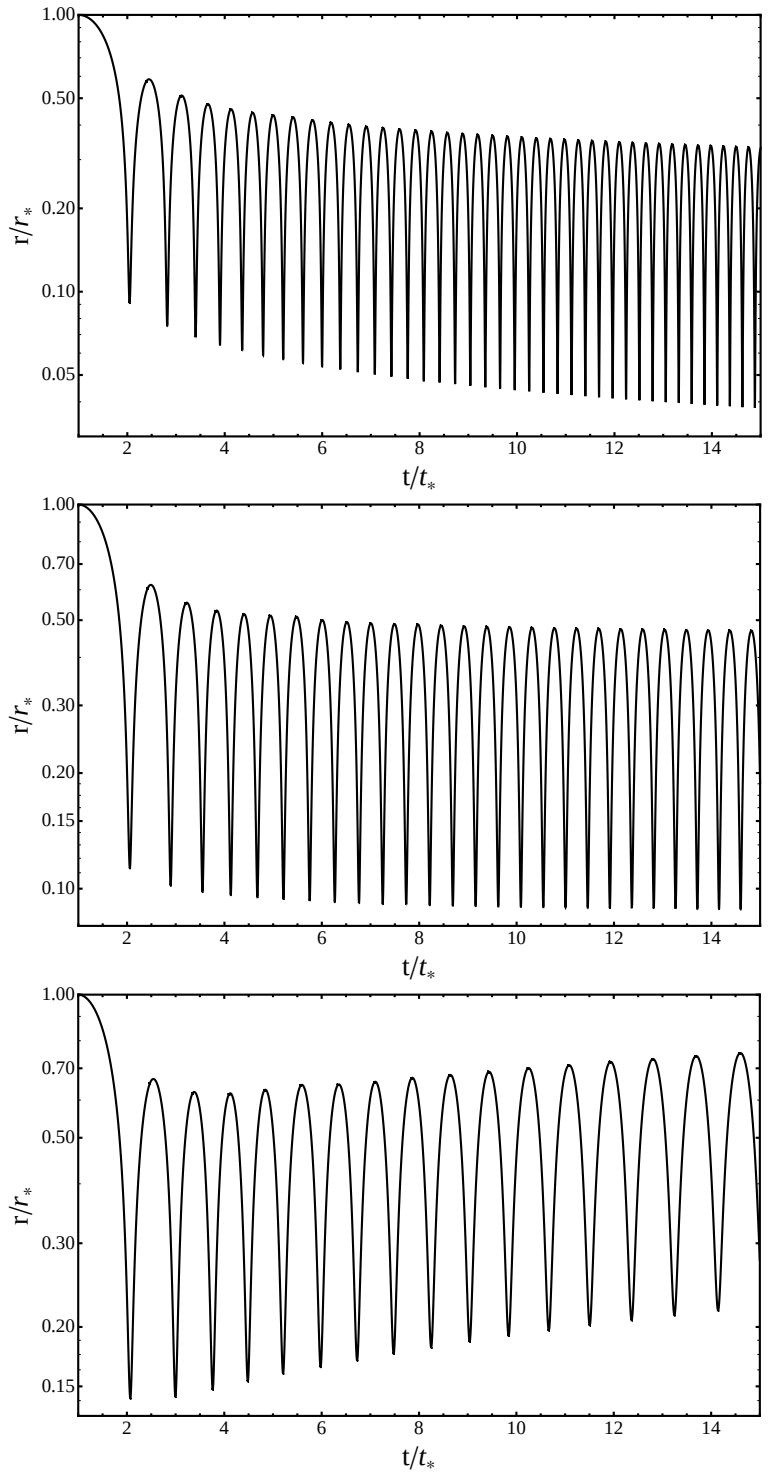

Figure 2-5: The radius of a mass shell, normalized to its turnaround radius, for a galactic size halo $\{n = 0.77, p = 2n, B_{1.5} = 0.39\}$, plotted vs time. The top panel shows a shell with particles that have decreasing angular momentum ($\varpi = -0.2$). The middle panel shown a shell with particles that have constant angular momentum ($\varpi = 0$). The bottom panel shows a shell with particles that have increasing angular momentum ($\varpi = 0.2$).

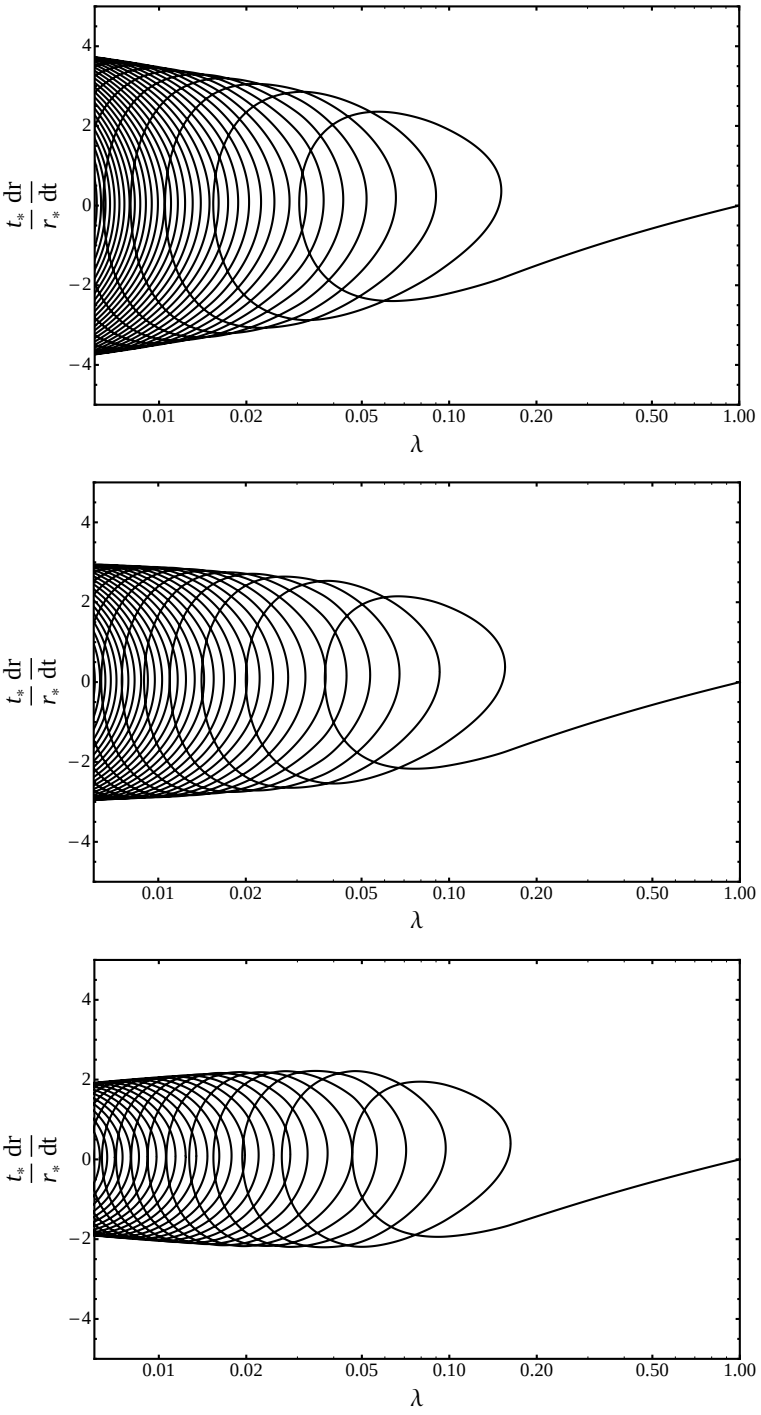

Figure 2-6: A phase space diagram of a galactic size halo $\{n = 0.77, p = 2n, B_{1.5} = 0.39\}$ at the current turnaround time. Velocities are normalized to the turnaround time and radius of each shell. The top panel shows a halo with $\varpi = -0.2$. The middle panel shows a halo with $\varpi = 0$. The bottom panel shows a halo with $\varpi = 0.2$.

It is informative to find how the transition radius y_0 depends on model parameters. Since the mass and angular momentum grow significantly before the first pericenter, we can only approximately determine this relationship. We assume that the profile is isothermal on large scales and the halo mass and shell angular momentum are fixed to their turnaround values. For $y_0 \ll 1$, the transitional radius y_0 solves the transcendental equation $y_0^2 \ln(y_0) = -9B^2/4\mathcal{M}(1)$. As expected, $B \to 0$ reproduces $y_0 \to 0$. As shown in Figure 2-2, $\mathcal{M}(1)$ varies with $\{B, p\}$. However, for reasonable parameter values, the mass normalization is changed at most by a factor of 2. Therefore, y_0 most strongly depends on B, and p has a negligible effect on the structure of the halo. As seen in figure 2-4, y_0 should also depends on ϖ. The above approximation neglects this dependence since we assumed the angular momentum is set to the turnaround value.

Figure 2-5 shows the radius of a mass shell, normalized to its turnaround radius r_*, for a galactic size halo $\{n = 0.77, p = 2n, B_{1.5} = 0.39\}$, as a function of time. In the top panel, particles in the shell lose angular momentum ($\varpi = -0.2$), in the middle panel the angular momentum remains constant ($\varpi = 0$), while in the bottom panel particles in the shell gains angular momentum ($\varpi = 0.2$). As expected, the pericenters in the top panel decrease with time while the pericenters grow in the bottom panel. Hence, the orbits of particles with decreasing angular momentum become more radial while those with increasing angular momentum become more circular.

Notice that the period of oscillation also varies for different ϖ. The period of oscillation is set by the shell's apocenter r_a and the mass internal to r_a. Using the adiabatic invariance relations we found in Section 2.5 and assuming Kepler's third law, we find that the period of the orbit $P \propto r_a^2$ for shells with decreasing angular momentum and $P \propto r_a$ for shells with increasing angular momentum. Moreover, from eqs. (2.56) and (2.60), r_a decreases (increases) with time for $\varpi < (>)\ 0$. Though Kepler's third law doesn't hold for this system, it still gives intuition for the above results.

Figure 2-6 shows the phase space diagram for a galactic size halo $\{n = 0.77, p = 2n, B_{1.5} = 0.39\}$. In the top panel, the particles in the shell lose angular momentum

($\varpi = -0.2$), in the middle panel the angular momentum remains constant ($\varpi = 0$), while in the bottom panel the particles in the shell gain angular momentum ($\varpi = 0.2$). The diagram labels the phase space point of every shell at the current turnaround time. All radial velocities are normalized to the shell's turnaround time t_* and radius r_*. Unlike FG, the presence of angular momentum results in caustics associated with pericenters as well, which can be seen in the lower panel of Figure 2-4. In addition, since an increasing angular momentum results in increasing pericenters, the pericenter caustics are more closely spaced in the lower panel than in the upper panel. Moreover, the amplitude of the radial velocity is smaller in the lower panel because orbits are circularizing. The phase space curve appears to intersect itself because we did not plot the tangential velocity component. In full generality, the distribution in the phase space $(r, v_r, v_t = L/r)$ for our model is a non-self-intersecting one-dimensional curve.

2.6.1 Comparing with N-body Simulations

In this subsection, we compare the density profile of our model's halo to empirical fits inspired by N-body simulations. We first numerically calculate the density profile for a galactic size halo with $\varpi = 0.12$. This value of ϖ was chosen so that $\rho \propto r^{-1}$ on small scales. We then compute the spherically averaged density in 50 spherical shells equally spaced in $\log_{10} r$ over the range $1.5 \times 10^{-4} < r/r_v < 3$, and take $r_v = r_{200}$ (defined above). This is the same procedure followed with the recent Aquarius simulation (Navarro et al., 2010). Next, we calculate r_{-2}, the radius where $r^2\rho$ reaches a maximum. For our halo, as discussed above, the profile is isothermal over a range of r. Moreover, the maximum peaks associated with the caustics are unphysical. So, we choose a value of r_{-2} in the isothermal regime that gives good agreement with the empirical fits. Changing r_{-2} does not change our interpretation of the results.

In Figure 2-7 we compare our spherically averaged density profile to NFW and Einasto profiles. We plot $r^2\rho$ in order to highlight differences. The NFW profile is given by (Navarro et al., 1996):

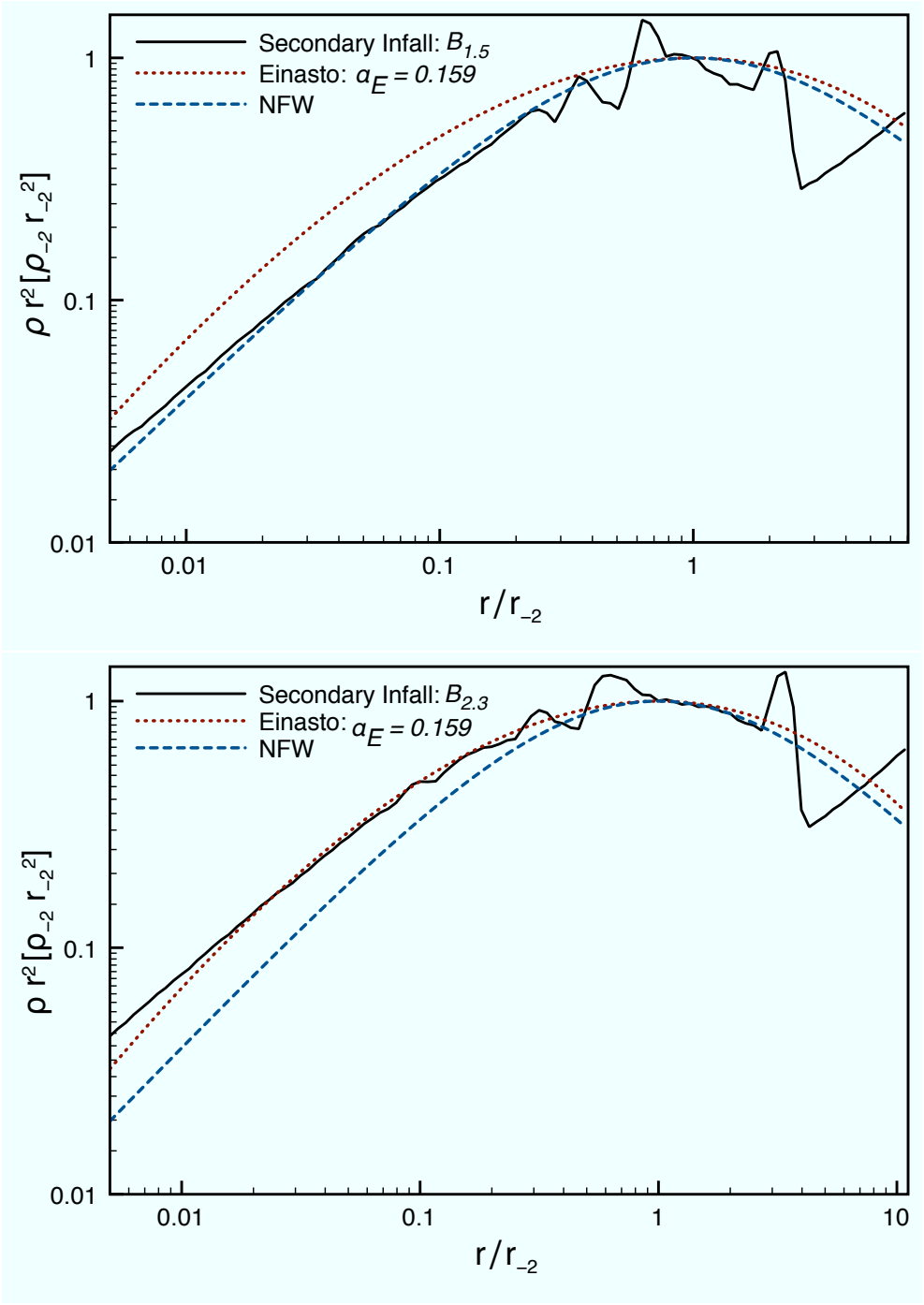

Figure 2-7: Spherically averaged density profile for the secondary infall model compared with NFW and Einasto profiles. The secondary infall model is calculated for a galactic size halo $\{n = 0.77, p = 2n\}$ with $\varpi = .1167$. In the top panel we chose $B_{1.5} = 0.39$ while in the bottom panel we chose $B_{2.3} = 0.26$.

$$\rho(r) = \frac{4\rho_{-2}}{(r/r_{-2})(1 + r/r_{-2})^2} \tag{2.61}$$

while the Einasto profile is given by:

$$\ln\left[\rho(r)/\rho_{-2}\right] = (-2/\alpha_E)[(r/r_{-2})^{\alpha_E} - 1] \tag{2.62}$$

where ρ_{-2} is the density of our halo at r_{-2} and α_E, known as the shape parameter, sets the width of the $r^2\rho$ peak. In the top panel, we use $B_{1.5} = .39$ while in the bottom panel, we use $B_{2.3} = .26$. We choose $\alpha_E = 0.159$ since this value was used in Figure 3 of Navarro et al. (2010).

We see that the secondary infall model works surprisingly well. The peaks are a result of the caustics that arise because of cold radial initial conditions. The first spike on the right comes from the first apocenter passage while the second comes from the first pericenter passage. The location of pericenter is most strongly influenced by the model parameter B. Hence, the isothermal region is smaller in the top panel than in the bottom panel since particles have less angular momentum at turnaround in the lower panel than in the upper panel. The parameter B then plays the same role as α_E; it sets the width of the isothermal region. If we assume N-body simulations faithfully represent dark matter halos, then Figure 2-7 implies that our estimate of B in eq. (2.30) overestimates the actual value by 1.5 to 2.3. We discuss possible reasons for this in Appendix A.2.

2.7 Discussion

N-body simulations reveal a wealth of information about dark matter halos. Older simulations predict density profiles that are well approximated by an NFW profile (Navarro et al., 1996), while more recent simulations find density profiles that fit better with a modified NFW profile (Moore et al., 1999) or the Einasto profile (Navarro et al., 2010). In an attempt to gain intuition for these empirical profiles, we've generalized the self-similar secondary infall model to include torque. This model doesn't

suffer from resolution limits and is much less computationally expensive than a full N-body simulation. Moreover, it is analytically tractable. Using this model, we were able to analytically calculate the density profile for $r/r_{\rm ta} \ll y_0$ and $y_0 \ll r/r_{\rm ta} \ll 1$. Note that the self-similar framework we've extended predicts power law mass profiles on small scales. Hence, it is inconsistent with an Einasto profile.

It is clear from our analysis that angular momentum plays an essential role in determining the structure of the halo in two important ways. First, the amount of angular momentum at turnaround (B) sets the width of the isothermal region. Second, the presence of pericenters softens the inner density slope relative to the FG solution because less mass shells contribute to the enclosed mass. Moreover, the interior density profile is sensitive to the way in which particles are torqued after turnaround (ϖ).

If we assume that ϖ is constant for all halos, then this secondary infall model predicts steeper interior density profiles for larger mass halos. More specifically, if we use the value of $\varpi = 0.12$ which gave $\rho \propto r^{-1}$ for galactic size halos, then $\rho \propto r^{-0.66}$ for a $10^8 M_\odot$ halo and $\rho \propto r^{-1.42}$ for a $10^{15} M_\odot$ halo. This trend towards steeper interior slopes for larger mass halos, and hence non-universality, has been noticed in recent numerical simulations (Ricotti et al., 2007; Cen et al., 2004) as well as more general secondary infall models (Del Popolo, 2010). On the other hand, if we assume that all halos have $\rho \propto r^{-1}$ as $r \to 0$, then ϖ must vary with halo mass. More specifically, halos with mass $M < 10^9 M_\odot$ must have particles which lose angular momentum over time ($\varpi < 0$) while halos with mass $M > 10^9 M_\odot$ must have particles which gain angular momentum over time ($\varpi > 0$). In other words, in order for our self-similar framework to predict universal density profiles, ϖ must conspire to erase any dependence on initial conditions. A more thorough treatment requires the use of N-body simulations, which is beyond the scope of this chapter.

It is also possible to predict a dark matter halo's density distribution if one assumes a mapping between a mass shell's initial radius, when the structure is linear, to its final average radius, which is some fraction of its turnaround radius. From this scheme, one can also infer a velocity dispersion, using the virial theorem. Unfortunately, this

scheme does not give any information about the halo's velocity anisotropy. Our self-similar prescription discussed above, on the other hand, contains all of the velocity information. Hence, one can reconstruct the velocity anisotropy profile given the trajectory of a mass shell. The velocity anisotropy is significant since it describes to what degree orbits are radial. Moreover, it can break degeneracies between n and ϖ in our halo model. We will discuss the velocity structure of our halo model, including the pseudo-phase-space density profile, in more detail in Paper 2 of this series. There we will once again compare our halo predictions to the recent Aquarius simulation results (Navarro et al., 2010).

While the above self-similar prescription has its clear advantages, it's also unphysical since mass shells at turnaround are radially cold. The same tidal torque mechanisms which cause a tangential velocity dispersion (Hoyle, 1951), should also give rise to a radial velocity dispersion. For a more physical model, one would need to impose self-similarity to a phase space description of the halo and include sources of torque as diffusion terms in the Boltzmann equation. This will be the subject of Paper 3 of this series.

As we've shown, the way in which particles are torqued after turnaround (ϖ) influences the interior power law of the density profile. One way to source this change in angular momentum is through substructure that is aspherically distributed throughout the halo. It is reasonable to assume that substructure dominated by baryons torque halo particles more strongly than substructure dominated by dark matter since baryons can achieve higher densities and hence are not tidally disrupted as easily. If this is the case, then torques sourced by baryons would result in a larger value of ϖ than torques sourced by dark matter. According to the predictions of this secondary infall model, this would lead to less cuspy profiles (See Appendix A.3 for a more detailed discussion). Therefore a more thorough understanding of ϖ coupled with this simplified model of halo formation could potentially shed light on the Cusp Core problem and thereby possibly bridge the gap between simulations and observations.

Chapter 3

Velocity Structure of Self-Similar Spherically Collapsed Halos[1]

Abstract

Using a generalized self-similar secondary infall model, which accounts for tidal torques acting on the halo, we analyze the velocity profiles of halos in order to gain intuition for N-body simulation results. We analytically calculate the asymptotic behavior of the internal radial and tangential kinetic energy profiles in different radial regimes. We then numerically compute the velocity anisotropy and pseudo-phase-space density profiles and compare them to recent N-body simulations. For cosmological initial conditions, we find both numerically and analytically that the anisotropy profile asymptotes at small radii to a constant set by model parameters. It rises on intermediate scales as the velocity dispersion becomes more radially dominated and then drops off at radii larger than the virial radius where the radial velocity dispersion vanishes in our model. The pseudo-phase-space density is universal on intermediate and large scales. However, its asymptotic slope on small scales depends on the halo mass and on how mass shells are torqued after turnaround. The results largely confirm N-body simulations but show some differences that are likely due to our assumption of a one-dimensional phase space manifold.

3.1 Introduction

Recent N-body simulations have revealed a wealth of information about the velocity structure of halos (Navarro et al., 2010; Ludlow et al., 2010; Vogelsberger et al.,

[1]This chapter is based on the published paper Zukin & Bertschinger 2010b

2010). However, simulations have finite dynamic range. Moreover, it is difficult to draw understanding from their analysis, and computational resources limit the smallest resolvable radius, since probing smaller scales require using more particles and smaller time steps. Hence, it seems natural to use analytic techniques, which do not suffer from resolution limits, to analyze the velocity distributions of halos.

Numerous authors have analytically investigated the density profiles of halos. Work began with Gunn and Gott where they analyzed the continuous accretion of mass shells onto an initial overdensity (Gunn & Gott, 1972; Gott, 1975; Gunn, 1977). This process is known as secondary infall. By imposing that the mass accretion is self-similar, Fillmore & Goldreich (1984) and Bertschinger (1985), assuming purely radial orbits, were able to analytically calculate the asymptotic slope of the density profile. Since then, there have been numerous extensions, some which do not assume self-similarity, that take into account non-radial motions (Ryden & Gunn, 1987; Nusser, 2001; Hiotelis, 2002; Williams et al., 2004; Sikivie et al., 1997; Del Popolo, 2009; White & Zaritsky, 1992; Le Delliou & Henriksen, 2003; Ascasibar et al., 2004). Those works that do not impose self-similarity can only infer information about the velocity dispersion using the virial theorem. Hence they cannot predict a halo's velocity anisotropy. Those works that do impose self-similarity focus only on the asymptotic slopes of density profiles.

In this Chapter, we analytically and numerically analyze the velocity structure of halos using an extended self-similar secondary infall model (Zukin & Bertschinger, 2010a). The work which introduced this extended infall model was discussed in detail in Chapter 1. We then compare the predictions of our halo model to simulation results, focusing on the velocity anisotropy (Binney & Tremaine, 2008) and pseudo-phase-space density profiles (Taylor & Navarro, 2001; Navarro et al., 2010; Ludlow et al., 2010).

Density profiles do not uniquely determine a self gravitating system. In order to more fully characterize dark matter halos, one needs to probe their phase space distributions. The velocity anisotropy and pseudo-phase-space density profiles are thereby useful since they complement density profiles by revealing additional infor-

mation about the phase space structure of the halo.

In Section 3.2 we summarize our generalized secondary infall model and discuss how to numerically calculate the radial and tangential velocity dispersions in the halo. In Section 3.3 we analytically calculate the asymptotic behavior of the radial and tangential kinetic energy profiles on small and intermediate scales. In Section 3.4 we compare our numerically calculated anisotropy and pseudo-phase-space density profiles to recent N-body results and conclude in Section 3.5.

3.2 Self-Similar Model

Here we first summarize the self-similar halo formation model developed in Chapter I. The model is characterized by four parameters $\{n, p, B, \varpi\}$ which are described below.

In this model, the universe is initially composed of a linear spherically symmetric density perturbation with mass shells that move approximately with the hubble flow. Because of the central overdensity, mass shells eventually stop their radially outward motion and turn around. The radius at which a mass shell first turns around, or its first apocenter, is known as the turnaround radius. Since the average density is a decreasing function from the central overdensity, mass shells initially farther away will turnaround later. The halo grows by continuously accreting mass shells. Mass shells are labeled by their turnaround time t_* or their turnaround radius r_*.

Model parameter n characterizes how quickly the initial linear density field falls off with radius ($\delta \propto r^{-n}$). It is related to the effective primordial power spectral index $n_{\rm eff}$ ($d\ln P/d\ln k$) through $n = n_{\rm eff} + 3$ (Hoffman & Shaham, 1985). Since $n_{\rm eff}$ depends on scale, n is set by the halo mass. As in Chapter I, we restrict our attention to $0 < n < 3$ so that the initial density field decreases with radius while the excess mass increases with radius. Note however that $n > 1.4$ corresponds to objects larger than galaxy clusters today. Model parameter n also sets the growth of the current turnaround radius: $r_{ta} \propto t^{\beta}$ where $\beta = 2(1+n)/3n$ (Zukin & Bertschinger, 2010a).

Self-similarity imposes that at time t, the angular momentum per unit mass L of

a particle in a shell at r, and the density ρ and mass M of the halo have the following functional forms (Zukin & Bertschinger, 2010a).

$$L(r,t) = B\frac{r_{\rm ta}^2(t)}{t}f(\lambda, t/t_*) \tag{3.1}$$

$$\rho(r,t) = \rho_B(t)D(\lambda) \tag{3.2}$$

$$M(r,t) = \frac{4\pi}{3}\rho_B(t)r_{\rm ta}^3(t)\mathcal{M}(\lambda) \tag{3.3}$$

where $\lambda \equiv r/r_{\rm ta}(t)$ is the radius scaled to the current turnaround radius, $\rho_B = 1/6\pi G t^2$ is the background density for an Einstein de-Sitter (flat $\Omega_m = 1$) universe, and B is a constant. Inspired by tidal-torque theory and numerical simulations, we take f to be:

$$f(\lambda, t/t_*) = \begin{cases} \lambda^{(4-p)/2} & \text{if } t < t_*, \\ (t/t_*)^{\varpi+1-2\beta} & \text{if } t > t_*. \end{cases} \tag{3.4}$$

Model parameter p, defined above, sets how quickly angular momentum builds up before turnaround while B sets the amplitude of angular momentum at turnaround. In Chapter I, using cosmological linear perturbation theory, we constrained p and B so that the angular momentum of particles before turnaround evolves as tidal torque theory predicts (Hoyle, 1951; Peebles, 1969; White, 1984; Doroshkevich, 1970). Conveniently both p and B are set by the halo mass. However, after comparing to density profiles from N-body simulations, we found that our expression for B derived from linear theory overestimates the actual value. Hence, for the rest of this chapter, the notation $B_{1.5}$ ($B_{2.3}$) signifies using a value of B divided by 1.5 (2.3).

Model parameter ϖ, defined above, sets how quickly the angular momentum of particles grows after turnaround. This parameter is difficult to constrain analytically since the halo is nonlinear after turnaround. However, in Chapter I we showed that a nonzero ϖ can be sourced by substructure. Moreover, ϖ influences the density profile at small scales since it controls how the pericenters of shells evolve over time.

The trajectory of a shell after turnaround contains all of the velocity information

in the halo. The trajectory's evolution equation, which follows from Newton's law, is given by:

$$\frac{d^2\lambda}{d\xi^2} + (2\beta - 1)\frac{d\lambda}{d\xi} + \beta(\beta - 1)\lambda = -\frac{2}{9}\frac{\mathcal{M}(\lambda)}{\lambda^2} + \frac{B^2}{\lambda^3}e^{2(\varpi+1-2\beta)\xi} \tag{3.5}$$

where $\xi \equiv \ln(t/t_{ta})$ and t_{ta} is the current turnaround time. The initial conditions for eq. (3.5) are $\lambda(\xi = 0) = 1$ and $d\lambda/d\xi(\xi = 0) = -\beta$. Calculating $\mathcal{M}(1)$ requires evolving both the shell's trajectory and $\mathcal{M}(\lambda)$ before turnaround (Zukin & Bertschinger, 2010a). Because of self-similarity, the trajectory $\lambda(\xi)$ can either be interpreted as labeling the location of a particular mass shell at different times, or labeling the location of all mass shells at a particular time. We take advantage of the second interpretation in order to numerically calculate the velocity profiles.

Inside the shell that is currently at its second apocenter, multiple shells exist at all radii. This can be seen from Figure 5 of (Bertschinger, 1985), which plots the location of all shells at a particular time. Therefore the expectation value of a quantity h, for example the radial velocity, at radius r and time t is the value of h for each shell at r weighted by each shell's mass. We find:

$$\langle h(r,t)\rangle = \frac{\int_0^{M_{ta}} \frac{dM_*}{M_{ta}} h(t,t_*)\delta^D\big(\lambda - \lambda(\xi)\big)}{\int_0^{M_{ta}} \frac{dM_*}{M_{ta}} \delta^D\big(\lambda - \lambda(\xi)\big)} \tag{3.6}$$

where M_{ta} is the current turnaround mass, $h(t,t_*)$ represents the value of h for the shell with turnaround time t_*, dM_* is the mass of the shell with turnaround time t_*, and δ^D is the dirac delta function which picks out all shells at r.

In order to numerically calculate h, we must relate $h(t,t_*)$ to $\lambda(\xi)$, the computed trajectory of the shell which turns around at t_{ta}. Using self-similarity, we find:

$$v_t(t,t_*) = B\frac{r_{ta}}{t}e^{(1+\varpi-2\beta)\xi_*}\frac{1}{\lambda(\xi_*)} \tag{3.7}$$

$$v_r(t,t_*) = \frac{r_{ta}}{t}e^{-\beta\xi_*}\frac{d}{d\xi}\left[e^{\beta\xi}\lambda(\xi)\right]|_{\xi=\xi_*} \tag{3.8}$$

where $\xi_* \equiv t/t_*$ and v_t (v_r) is the tangential (radial) velocity. Using eqs. (3.6)-(3.8),

and taking advantage of the delta function, the tangential (σ_t^2) and radial (σ_r^2) velocity dispersions become:

$$\sigma_t^2(r,t) \equiv \left\langle v_t^2(r,t)\right\rangle = \frac{r_{ta}^2}{t^2}\frac{\sum_i e^{(4-7\beta+2\varpi)\xi_i}\lambda_i^{-2}\left|d\lambda/d\xi\right|_i^{-1}}{\sum_i e^{(2-3\beta)\xi_i}\left|d\lambda/d\xi\right|_i^{-1}} \tag{3.9}$$

$$\begin{aligned}\sigma_r^2(r,t) &\equiv \left\langle v_r^2(r,t)\right\rangle - \left\langle v_r(r,t)\right\rangle^2 \\ &= \frac{r_{ta}^2}{t^2}\frac{\sum_i e^{(2-5\beta)\xi_i}\left[d(e^{\beta\xi}\lambda)/d\xi\right]_i^2\left|d\lambda/d\xi\right|_i^{-1}}{\sum_i e^{(2-3\beta)\xi_i}\left|d\lambda/d\xi\right|_i^{-1}} \\ &- \frac{r_{ta}^2}{t^2}\left(\frac{\sum_i e^{(2-4\beta)\xi_i}\left[d(e^{\beta\xi}\lambda)/d\xi\right]_i\left|d\lambda/d\xi\right|_i^{-1}}{\sum_i e^{(2-3\beta)\xi_i}\left|d\lambda/d\xi\right|_i^{-1}}\right)^2\end{aligned} \tag{3.10}$$

where ξ_i is the ith root that satisfies $\lambda = \lambda(\xi)$. In the above, we've imposed $\langle v_t(r,t)\rangle = 0$ since our model assumes that the orbital planes of particles in a given shell are oriented in random directions. Note that inside the shell that is currently at its second apocenter, interference between multiple shells forces $\langle v_r(r,t)\rangle$ to quickly go to zero.

3.3 Asymptotic Behavior

Here, using techniques developed in (Fillmore & Goldreich, 1984), we analytically calculate the logarithmic slope of the tangential and radial kinetic energy in two different radial regimes. We accomplish this by taking advantage of adiabatic invariance and self consistently calculating the total radial and tangential kinetic energy profiles of the halo.

We start by parametrizing the halo mass, radial kinetic energy K_r, tangential kinetic energy K_t and the variation of the apocenter distance r_a.

$$M(r,t) = \kappa(t) r^{\alpha} \tag{3.11}$$

$$K_r(r,t) = \kappa_r(t) r^{\alpha_r} \tag{3.12}$$

$$K_t(r,t) = \kappa_t(t) r^{\alpha_t} \tag{3.13}$$

$$\frac{r_a}{r_*} = \left(\frac{t}{t_*}\right)^q \tag{3.14}$$

In the above r_* is the turnaround radius of a mass shell that turns around at t_*. As was shown in Chapter I, adiabatic invariance allows us to relate q and α to n. At late times, the orbital period is much smaller than the time scale for the mass and angular momentum to grow. Integrating Newton's equation and assuming $\kappa(t)$ and $L(t)$ change little over an orbit, we find:

$$\left(\frac{dr}{dt}\right)^2 = \frac{2G\kappa(t)}{\alpha-1}(r_a^{\alpha-1} - r^{\alpha-1}) - L^2(t)(r^{-2} - r_a^{-2}). \tag{3.15}$$

The above relationship tell us how the pericenters r_p evolve with time. Defining $y \equiv r_p/r_a$ and evaluating the above at $r = r_p$, we find:

$$\frac{1-y^{\alpha-1}}{y^{-2}-1} \equiv A(y) = \frac{(\alpha-1)L^2(t)}{2G\kappa(t) r_a^{\alpha+1}(t)} \tag{3.16}$$

In Chapter I, by analyzing the radial action, we found that when $y \ll 1$, $\kappa(t) r_a^{\alpha+1}(t) =$ const. Therefore, for $\varpi < 0$, eq. (3.16) implies that y will decrease over time. However, for $\varpi > 0$, $\kappa(t) r_a^{\alpha+1}(t) =$ const and eq. (3.16) imply that y will increase over time and will at one point violate $y \ll 1$. Since we only consider bound orbits, the constraint $y \leq 1$ holds. At late times, as the angular momentum continues to increase for $\varpi > 0$, $y \sim 1$, orbits become approximately circular, the radial action vanishes, and $L^2(t) \sim \kappa(t) r_a^{\alpha+1}(t)$. Hence halos with $\varpi < 0$ will have orbits that become more radial over time ($y \ll 1$) while halos with $\varpi > 0$ will have orbits that become more circular over time ($y \sim 1$). The above insight leads to the following constraint.

$$q = \begin{cases} \frac{1}{\alpha+1}\{2\varpi + \frac{2}{3n}[\alpha(1+n)-3]\} & \text{if } \varpi \geq 0 \\ \frac{2}{3n(\alpha+1)}\left[\alpha(1+n)-3\right] & \text{if } \varpi < 0 \end{cases} \tag{3.17}$$

For the specific case, $\varpi < 0$, taking advantage of $y \ll 1$, the adiabatic invariance arguments above, and eqs. (3.1) and (3.4), we can rewrite eqn. (3.16) in the form $y(t, t_*) = y_0(t/t_*)^l$, where:

$$l = \begin{cases} \varpi & \text{if } \alpha > 1, \\ 2\varpi/(\alpha+1) & \text{if } \alpha < 1. \end{cases} \tag{3.18}$$

and $y_0 r_*$ is the pericenter of a mass shell at turnaround. The special case $\alpha = 1$ will be addressed later.

We next calculate the kinetic energy profiles. After a few orbits, shells oscillate at a much higher frequency than the growth rate of the halo. When calculating the internal mass profile, this allows us to weight each mass shell based on how much time it spends interior to a certain scale (Fillmore & Goldreich, 1984). Likewise, when calculating the total internal kinetic energy profile, we can weight each mass shell by both a time-averaged v_t^2 (or v_r^2) and a factor that accounts for how often the shell lies interior to a certain scale. For a derivation, please see the Appendix.

Using eqs. (3.15) and (3.16), the kinetic energy weighting $P_i(r/r_a, y)$ at time t for a mass shell with apocenter distance r_a, pericenter yr_a, below r, is:

$$\begin{aligned} P_i(u,y) &= 0 && (u < y) \\ P_i(u,y) &= \frac{I_i(u,y)}{I(1,y)} && (y < u \leq 1) \\ P_i(u,y) &= \frac{I_i(1,y)}{I(1,y)} && (u > 1) \end{aligned} \tag{3.19}$$

where

$$I_t(u,y) = \frac{1}{2}\left(\frac{Br_*^2}{t_* r_a}\right)^2 \left(\frac{t}{t_*}\right)^{2\varpi} \int_y^u \frac{dv}{v^2 f(v,y)} \tag{3.20}$$

$$I_r(u,y) \propto \frac{r_{ta}^2}{t^2}\left(\frac{r_a}{r_{ta}}\right)^{\alpha-1} \int_y^u f(v,y)dv \tag{3.21}$$

$$I(u,y) = \int_y^u \frac{dv}{f(v,y)} \tag{3.22}$$

and

$$f(v,y) \equiv \begin{cases} ((1-v^{\alpha-1}) - A(y)(v^{-2}-1))^{1/2} & \text{if } \alpha > 1, \\ ((v^{\alpha-1}-1) + A(y)(v^{-2}-1))^{1/2} & \text{if } \alpha < 1. \end{cases} \tag{3.23}$$

The index $i = \{r, t\}$ is used for shorthand to represent either the radial or tangential direction and the dependence of r_a and r_p on t_* is implicit. Eq. (3.21) is not an equality since $G\kappa(t) \propto r_{ta}^{3-\alpha}/t^2$. Moreover, the proportionality constant varies for different radial regimes in the halo.

Similar to the treatment in Chapter I, self consistency demands that:

$$\left(\frac{r}{r_{ta}}\right)^{\alpha_i} = \frac{K_i(r,t)}{K_i(r_{ta},t)} \propto \int_0^{M_{ta}} \frac{dM_*}{M_{ta}} \frac{t^2}{r_{ta}^2} P_i\left(\frac{r}{r_a(t,t_*)}, y(t,t_*)\right) \tag{3.24}$$

where dM_* is the mass of a shell that turned around at t_* and M_{ta} is the current turnaround mass. The above is not an equality, even for the tangential kinetic energy, because of a proportionality constant, similar to $\mathcal{M}(1)$, that is not included. See the Appendix for details. Its numerically computed value does not affect the asymptotic slopes α_i. Noting from eq. (3.3) that

$$\frac{dM_*}{d\ln t_*} = (3\beta-2)M_{ta}\left(\frac{t}{t_*}\right)^{3\beta-2}, \tag{3.25}$$

using eq. (3.14) and transforming integration variables to $u \equiv r/r_a$, we find:

$$\left(\frac{r}{r_{ta}}\right)^{\alpha_i - k} \propto \frac{t^2}{r_{ta}^2} \int_{r/r_{ta}}^{\infty} \frac{du}{u^{1+k}} P_i(u, y(t, t_*)) \tag{3.26}$$

where $k = (3\beta - 2)/(\beta - q)$. As u increases, the above integral sums over shells with smaller t_*. Since the pericenter of a shell evolves with time, the second argument of P_i depends on u. The dependence varies with torque model (sign of ϖ); hence we've kept the dependence on u implicit. Next we analyze the above for certain regimes of r/r_{ta}, and certain torquing models, in order to constrain the relationship between α_i and k.

3.3.1 Inner Solution; Negative Torque

For $\varpi < 0$, particles lose angular momentum over time. When probing scales $r/r_{\rm ta} \ll y_0$, mass shells with $t_* \ll t_{ta}$ only contribute. As a result, $y(t, t_*) \ll 1$. Using eq. (3.18), we then find:

$$y(t, t_*) = y_0 \left(\frac{t}{t_*}\right)^l = y_0 \left(\frac{r}{u r_{\rm ta}}\right)^{\delta} \tag{3.27}$$

where $\delta \equiv l/(q - \beta)$ and $u \equiv r/r_a$. For bound mass shells, $q - \beta < 0$. Therefore, since $\delta > 0$, the first argument of P_i in eq. (3.26) increases while the second decreases as we sum over shells that have turned around at earlier and earlier times ($u \to \infty$). For $r/r_{\rm ta} \ll y_0$, mass shells which most recently turned around do not contribute to the kinetic energy inside $r/r_{\rm ta}$ since we are probing scales below their pericenters. Mass shells only begin to contribute when the two argument of P_i are roughly equal to each other. This occurs around:

$$u = y_1 \equiv \left(y_0 (r/r_{\rm ta})^{\delta}\right)^{1/(1+\delta)} \tag{3.28}$$

Hence, we can replace the lower limit of integration in eq. (3.26) with y_1. We next want to calculate the behavior of eq. (3.26) close to y_1 in order to determine whether the integrand is dominated by mass shells around y_1 or mass shells that have turned around at much earlier times. The first step is to calculate the behavior of $P_i(u, y)$

for $u \approx y$. We find:

$$P_t(u,y) \propto \frac{r_{ta}^2}{t^2}\left(\frac{r}{ur_{ta}}\right)^{l_t} u^{1/2}(1-y/u)^{1/2} \times \begin{cases} y^{-3/2} & \text{if } \alpha > 1, \\ y^{-1-\alpha/2} & \text{if } \alpha < 1. \end{cases} \tag{3.29}$$

$$P_r(u,y) \propto \frac{r_{ta}^2}{t^2}\left(\frac{r}{ur_{ta}}\right)^{l_r} u^{3/2}(1-y/u)^{3/2} \times \begin{cases} y^{-1/2} & \text{if } \alpha > 1, \\ y^{-1+\alpha/2} & \text{if } \alpha < 1. \end{cases} \tag{3.30}$$

where $l_t = 2(1+\varpi-q-\beta)/(q-\beta)$ and $l_r = \alpha - 1$. Given the above, we evaluate the indefinite integral in eq. (3.26), noting that y is a function of u (eq. 3.27). For $u \sim y_1$, we find:

$$\frac{t^2}{r_{ta}^2}\int \frac{du}{u^{1+k}} P_t\left(u, y_0\left(\frac{r}{ur_{\rm ta}}\right)^{\delta}\right) \propto (u/y_1-1)^{3/2}\left(\frac{r}{r_{ta}}\right)^{l_t} \times \begin{cases} y_1^{-1-k-l_t} & \text{if } \alpha > 1, \\ y_1^{-1/2-k-l_t-\alpha/2} & \text{if } \alpha < 1. \end{cases} \tag{3.31}$$

$$\frac{t^2}{r_{ta}^2}\int \frac{du}{u^{1+k}} P_r\left(u, y_0\left(\frac{r}{ur_{\rm ta}}\right)^{\delta}\right) \propto (u/y_1-1)^{5/2}\left(\frac{r}{r_{ta}}\right)^{l_r} \times \begin{cases} y_1^{1-k-l_r} & \text{if } \alpha > 1, \\ y_1^{1/2-k-l_r+\alpha/2} & \text{if } \alpha < 1. \end{cases} \tag{3.32}$$

Following the logic in Chapter I, if we keep u/y_1 fixed and the integrand blows up as $y_1 \to 0$, then the left hand side of eq. (3.26) must diverge in the same way as the right hand side shown in eqs. (3.31) and (3.32). Therefore, using eq. (3.28):

$$\alpha_t - k - l_t = \begin{cases} -\delta(1+k+l_t)/(1+\delta) & \text{if } \alpha > 1, \\ -\delta(1/2+k+l_t+\alpha/2)(1+\delta) & \text{if } \alpha < 1. \end{cases} \tag{3.33}$$

$$\alpha_r - k - l_r = \begin{cases} \delta(1-k-l_r)/(1+\delta) & \text{if } \alpha > 1, \\ \delta(1/2-k-l_r+\alpha/2)(1+\delta) & \text{if } \alpha < 1. \end{cases} \tag{3.34}$$

Otherwise, if the integrand converges, then the right hand side is proportional to $(r/r_{ta})^{l_i}$. Therefore, the left hand side must also have the same scaling, which implies $\alpha_i = k + l_i$. Solving the above system of equations for α_i simplifies dramatically since we have already solved for $\{\alpha, k, q\}$ in Chapter I. Rewritten below for convenience, we found:

$$\begin{aligned} \text{For } n &\leq 2: \\ \alpha &= \frac{1+n-\sqrt{(1+n)^2+9n\varpi(n\varpi-2)}}{3n\varpi} \\ k &= \frac{1+n+3n\varpi-\sqrt{(1+n)^2+9n\varpi(n\varpi-2)}}{n\varpi(4+n)} \\ q &= \frac{1+n-3n\varpi-\sqrt{(1+n)^2+9n\varpi(n\varpi-2)}}{3n} \\ \text{For } n &\geq 2: \\ \alpha &= k = \frac{3}{1+n}\,, \quad q = 0. \end{aligned} \tag{3.35}$$

Using eq. (3.35) to solve for α_i and making sure the solution is consistent, (ie: using eqs. (3.33) and (3.34) only if the integrand diverges as $y_1 \to 0$), we find:

$$
\begin{aligned}
\text{For } n &\leq 2: \\
\alpha_t &= \alpha_r = \frac{12 - 9n\varpi - 2\sqrt{(1+n)^2 + 9n\varpi(n\varpi - 2)}}{1 + n + \sqrt{(1+n)^2 + 9n\varpi(n\varpi - 2)}} \\
\text{For } n &\geq 2: \\
\alpha_t &= \frac{(4+n)(3n\varpi + 2n - 10)}{2(1+n)(3n\varpi - n - 4)} \\
\alpha_r &= \frac{5-n}{1+n}.
\end{aligned}
\tag{3.36}
$$

The above solutions are continuous at $n = 2$. Taking the no-torque limit ($\varpi \to 0$), we find $\alpha_t = \alpha_r = (5-n)/(1+n)$ for all n. Assuming virial equilibrium, one would predict $\alpha_i = 2\alpha - 1 = (5-n)/(1+n)$. Hence, in the no-torque limit, both the radial and tangential kinetic energy are virialized. However, when $\varpi < 0$, only the radial kinetic energy for $n \geq 2$ is virialized. All other profiles are out of virial equilibrium because they are dominated by shells which recently turned around and hence have not had time to virialize. Since all collapsed objects today have $n < 2$, this model predicts unvirialized halos when particles lose angular momentum after turnaround.

3.3.2 Inner Solution; Positive Torque

For $\varpi > 0$, the angular momentum of particles increase with time. As mentioned above, when probing scales $r/r_{\rm ta} \ll y_0$, mass shells with $t_* \ll t_{ta}$ only contribute. As a result, $y(t, t_*) \sim 1$. In other words, the orbits are roughly circular. We can therefore replace the lower limit of integration in eq. (3.26) with 1 since mass shells will only start contributing to the sum when $u \sim y \sim 1$. Hence, the right hand side of eq. (3.26) is proportional to $(r/r_{ta})^{l_i}$, which implies $\alpha_i = k + l_i$. Using the results from Paper 1, reproduced below for convenience,

$$
\alpha = k = \frac{3}{1 + n - 3n\varpi}\ , \quad q = 2\varpi\ , \quad \text{for } 0 \leq n \leq 3,
\tag{3.37}
$$

we find:

$$\alpha_t = \alpha_r = \frac{5 - n + 3n\varpi}{1 + n - 3n\varpi}\,, \qquad \text{for } 0 \leq n \leq 3. \tag{3.38}$$

The no-torque case, $\varpi = 0$, is consistent with the analysis in the prior subsection. The singularity $\varpi = (1+n)/3n$, as discussed in Chapter I, corresponds to orbits that are not bound. Hence we only consider $\varpi < (1+n)/3n$. Eq. (3.38) shows that the halo, for $\varpi \geq 0$, is in virial equilibrium ($\alpha_i = 2\alpha - 1$). This is expected since the velocity profiles are dominated by mass shells that have turned around at $t \ll t_{ta}$.

3.3.3 Outer Solution

In this regime, we are probing scales larger than the pericenters of the most recently turned around mass shells. As a result, $P_i(u, y)$ is dominated by the contribution from the integrand when $u \gg y$. Therefore:

$$P_t(u,y) \;\propto\; \frac{r_{ta}^2}{t^2}\left(\frac{r}{ur_{ta}}\right)^{l_t} \times \begin{cases} y^{-1} & \text{if } \alpha > 1, \\ y^{-(\alpha+1)/2} & \text{if } \alpha < 1. \end{cases} \tag{3.39}$$

$$P_r(u,y) \;\propto\; \frac{r_{ta}^2}{t^2}\left(\frac{r}{ur_{ta}}\right)^{l_r} \times \begin{cases} u & \text{if } \alpha > 1, \\ u^{(\alpha+1)/2} & \text{if } \alpha < 1. \end{cases} \tag{3.40}$$

Plugging in the above into eq. (3.26), using the results of Chapter I shown below for convenience,

$$\begin{aligned} \alpha &= 1\,, \quad k = \frac{6}{4+n}\,, \quad q = \frac{n-2}{3n}\,, \quad \text{for } n \leq 2 \\ \alpha &= k = \frac{3}{1+n}\,, \quad q = 0\,, \qquad\qquad\quad \text{for } n \geq 2 \end{aligned} \tag{3.41}$$

and utilizing the same divergence and convergence arguments above, we find:

$$\begin{aligned}
\text{For } n &\leq 2: \\
\alpha_t &= 0, \qquad \alpha_r = 1 \\
\text{For } n &\geq 2: \\
\alpha_t &= \begin{cases} 0 & \text{if } \varpi < \frac{5-n}{3n}, \\ \frac{5-n-3n\varpi}{1+n} & \text{if } \frac{5-n}{3n} \leq \varpi < \frac{1+n}{3n}. \end{cases} \\
\alpha_r &= \frac{5-n}{1+n}.
\end{aligned} \tag{3.42}$$

The above solutions are continuous at $n = 2$. The upper limit $(1 + n)/3n$ on ϖ enforces that orbits are bound ($\varpi < \beta/2$). For $n \leq 2$, $\varpi > (5 - n)/3n$ results in unbound orbits and hence is not considered. The radial kinetic energy follows the same profile expected from virial equilibrium ($\alpha_r = 2\alpha - 1$), even though recently turned around mass shells dominate the kinetic energy for $n < 2$. We believe this is a result of angular momentum not playing a dynamical role at these scales. Using this logic, and as eq. (3.42) reveals, this is consistent with the the tangential kinetic energy not being virialized ($\alpha_t \neq 2\alpha - 1$). Taking the limit of eq. (3.36) as $\varpi \to -\infty$, we recover the same expressions as eq. (3.42) for α_r. This is expected since in this limit, particles lose their angular momentum instantly, resulting in purely radial orbits. We do not expect to recover the same expressions for α_t since the tangential kinetic energy vanishes in this limit.

Eqs. (3.35), (3.37) and (3.41) determine how quickly the mass inside a fixed radius grows as a function of time ($\kappa(t)$ defined in eq. 3.11). When $q = 0$, apocenters of mass shells settle down to a constant fraction of their turnaround radii, leading to a constant mass inside a fixed radius. For cosmologically relevant structures ($n < 1.4$), this occurs on small scales for $\varpi = 0$. When $q < 0$, inward migration leads to an increasing mass inside a fixed radius. When $q > 0$, outward migration leads to a decreasing mass inside a fixed radius.

This section assumed $\alpha \neq 1$ and yet, for certain parts of parameter space, eqs. (3.35), (3.37) and (3.41) give $\alpha = 1$. However, since the solutions are continuous as $\alpha \to 1$ from the left and right, then the results hold for $\alpha = 1$ as well.

3.4 Comparison with N-body Simulations

In this section, using the analytic results derived above to gain intuition, we first analyze how ϖ influences the anisotropy and pseudo-phase-space density profiles and then compare our numerically computed profiles to recent N-body simulations of galactic size halos (Navarro et al., 2010).

As described in Chapter I, the mass of a halo is not well defined when our model is applied to cosmological structure formation since it is unclear how the spherical top hat mass which characterizes the halo when it is linear relates to the virial mass which characterizes the halo when it is nonlinear. For halos today with galactic size virial masses, we assume the model parameter n which characterizes the initial density field, is set by a spherical top hat mass of $10^{12} M_{\odot}$. Specifying the top hat mass also sets model parameters B and p. For explicit expressions used to calculate model parameters n, p, and B, please see Chapter I.

When analyzing the influence of ϖ, we use model parameters: $n = 0.77$, $p = 2n$, and $B_{1.5} = 0.39$. When comparing to N-body simulations, we use model parameters $n = 0.77$, $p = 2n$, $\varpi = 0.12$, and $B_{1.5}$ ($B_{2.3}$) $= 0.39$ (0.26). This value of ϖ ensures $\rho \propto r^{-1}$ on small scales and, as shown in Chapter I, this range in B gives good agreement with the Einasto and NFW profiles (Navarro et al., 1996).

For the N-body comparisons, we average ρ, σ_t^2, and σ_r^2 in 50 spherical shells equally spaced in $\log_{10} r$ over the range $1.5 \times 10^{-4} < r/r_v < 3$, where r_v satisfies $M(r_v, t) = 800\pi r_v^3 \rho_B(t)/3$. This is the same procedure followed with the recent Aquarius simulation (Navarro et al., 2010). We also calculate r_{-2}, the radius where $r^2\rho$ reaches a maximum. This radius, as well as the virial radius r_v, are commonly referred to in simulation papers. As discussed in Chapter I, the density profile is isothermal for our halo over a range of r. Moreover, the maximum peaks associated

with the caustics are unphysical. So, we choose a value of r_{-2} in the isothermal regime that gives good agreement with empirical density profiles. Changing r_{-2} does not change our interpretation of the results. We find $r_{-2}/r_{ta} = 0.07$ (0.05) for $B_{1.5}$ ($B_{2.3}$). For reference, we find the dimensionless radius of first pericenter passage (y_0) to be 0.042 (0.026) for $B_{1.5}$ ($B_{2.3}$).

As mentioned previously, N-body simulations have finite dynamic range. The innermost radius where the simulation results can be trusted is set by the total number of particles (Power et al., 2003). The recent Aquarius simulations characterize their innermost radius based on the convergence of the circular velocity, at a particular radius, for the same halo simulated at different resolutions (Navarro et al., 2010). The notation $r^{(1)}_{\rm conv}$ ($r^{(7)}_{\rm conv}$) corresponds to the smallest radius such that the circular velocity has converged to 10% (2.5%) or better at larger radii. When these radii are showed in the figures, we use the values quoted in Table 2 of (Navarro et al., 2010) for halo Aq-A-2 ($r^{(1)}_{\rm conv}/r_{-2} = 0.022$ and $r^{(7)}_{\rm conv}/r_{-2} = 0.052$) since all six halos were simulated at this resolution.

3.4.1 Anisotropy Profile

Here we analyze the velocity anisotropy $\beta_v \equiv 1 - \sigma_t^2/2\sigma_r^2$ for galactic size halos, where the tangential and radial velocity dispersions are defined in eqs. (3.9) and (3.10) respectively. Based on the analysis in Section 3.3, we expect β_v to asymptote to a constant for $r/r_{ta} \ll y_0$ since $\sigma_t^2 \propto \sigma_r^2$ and β_v to increase for $y_0 \ll r/r_{ta} \ll r_v/r_{ta}$ since $\sigma_t^2/\sigma_r^2 \propto r^{-1}$. Moreover, for radii larger than the first shell crossing ($r \sim r_v$), $\sigma_r^2 = 0$ since only one shell contributes to the dispersion. Hence, in this radial range, $\beta_v = -\infty$.

In the top panel of Figure 3-1 we plot the velocity anisotropy for galactic size halos with varying ϖ. In the bottom panel, we plot the smoothed velocity anisotropy for model parameters that give good agreement with density profiles from simulated galactic size halos. The downward spikes in both panels are caustics which exist because of unphysical radially cold initial conditions. In both panels, as analytically predicted, the velocity anisotropy asymptotes at small radii, increases at intermediate

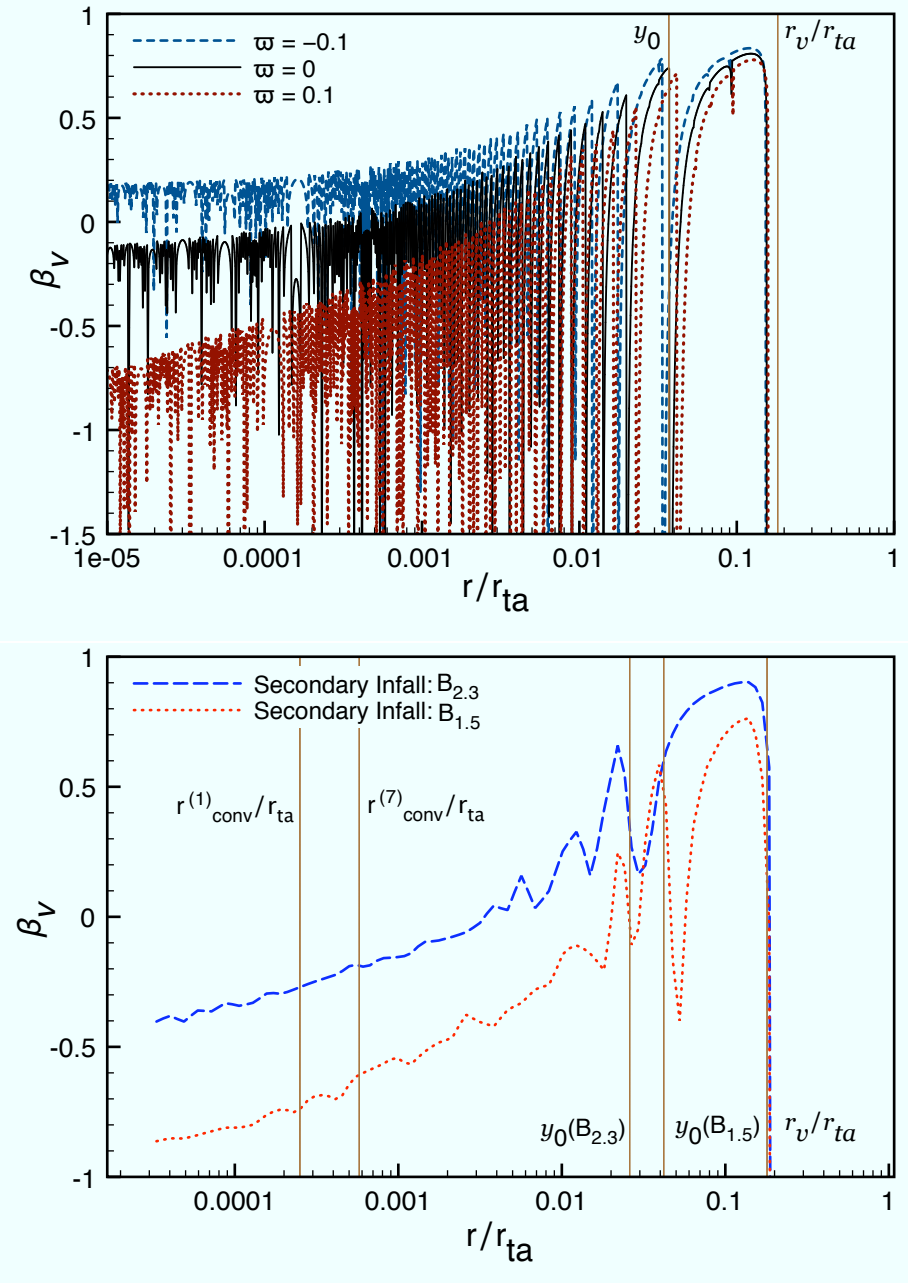

Figure 3-1: The top panel shows the velocity anisotropy profile for a self-similar halo with model parameters $n = 0.77$, $p = 2n$, $B_{1.5} = 0.39$, and varying ϖ. Smaller ϖ leads to halos with more radial orbits at a particular radius. The bottom panel shows the smoothed velocity anisotropy profile for a self-similar halo with model parameters $n = 0.77$, $p = 2n$, $\varpi = 0.12$, and $B_{1.5}$ ($B_{2.3}$) $= 0.39$ (0.26). Smaller B leads to a larger peak width and more radial orbits. The profile is qualitatively similar to results from N-body simulations. The dimensionless radius of first pericenter passage (y_0) and the virial radius (r_v) are labeled for clarity. The convergence radii for the Aquarius halo Aq-A-2 (Navarro et al., 2010) are labeled for reference.

radii, and then drops off near the virial radius.

The top panel shows that ϖ affects the radius of first pericenter passage (y_0), the amplitude of β_v close to the virial radius, as well as the asymptotic value of β_v at small radii. This behavior is intuitive since smaller values of ϖ give rise to halos populated with less circularized orbits at a given radius. Note however that the envelope of the anisotropy profile begins to increase and become more radially dominated for $r/r_{ta} < y_0$, contradicting our analytic analysis. More specifically, for $\varpi = -0.1$, $\beta_v \sim 0.2$ for $r/r_{ta} < 0.001$, and starts to increase at $r/r_{ta} \sim 0.001$ when it should start increasing at $r/r_{ta} \sim y_0$, according to Section 3.3. This is a result of assumptions used to calculate α_r breaking down. This is more apparent for $\varpi > 0$ since the orbital period is longer. However, as $r \to 0$, the assumptions become more valid.

In the bottom panel, we show how model parameter B affects the velocity anisotropy. As discussed in Chapter I, smaller B leads to orbits that take longer to circularize and density profiles with a larger isothermal region (smaller y_0). The bottom panel should be compared to Figures 9 and 10 of (Navarro et al., 2010). Though our model cannot address structure outside r_v, the graphs are qualitatively very similar. The width of the peak predicted in our model agrees with results from N-body simulations. This should be expected since the parameter B was chosen so that the width of the isothermal region in the density profiles agree. However, our model over predicts the velocity anisotropy close to r_v and under predicts the velocity anisotropy at small radii. In other words, at large scales the halo is populated with too many radial orbits while on small scales the halo is populated with too many circular orbits.

This trend is most clearly seen in Figure 3-2. There we plot the local velocity anisotropy versus the logarithmic slope of the density profile for a galactic size halo with $B_{2.3} = 0.26$ as well as a universal relationship relating these two quantities that was derived by Hansen & Moore (2006). The open circles correspond to $1.5\times10^{-4}\ r_v < r < r_{-2}$ while the filled circles correspond to $r_{-2} < r < r_v$. This figure should be compared to Figure 11 of (Navarro et al., 2010). In the Aquarius simulation paper, the Hansen & Moore prediction agrees well with N-body results for $r < r_{-2}$. However,

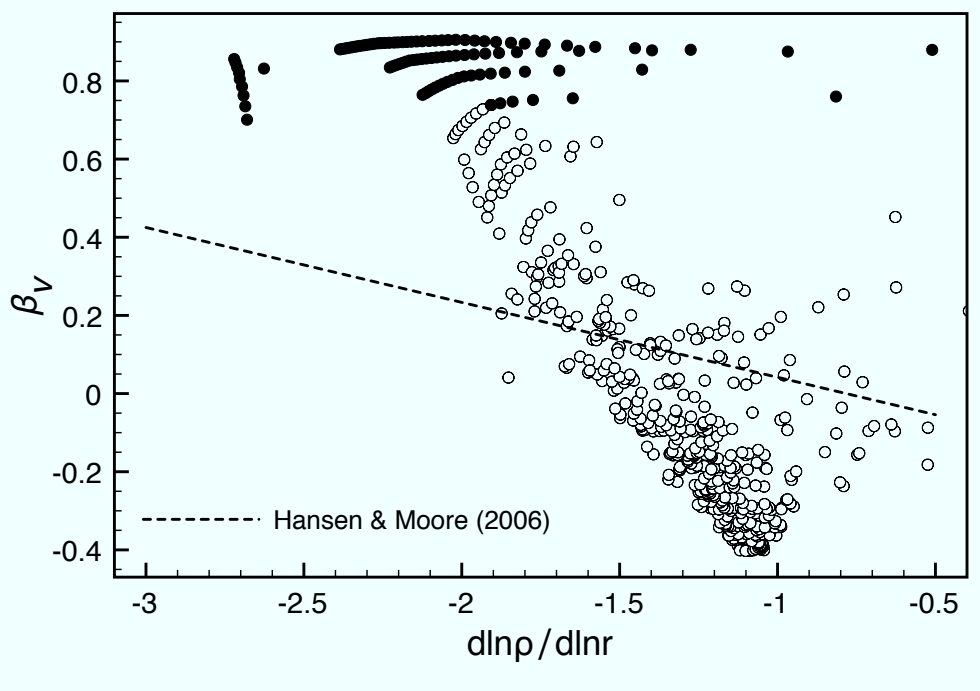

Figure 3-2: The local logarithmic slope of the density profile plotted against the velocity anisotropy. The relationship relating these two quantities that was proposed by Hansen & Moore (2006) is also showed. Open circles correspond to $1.5 \times 10^{-4}\ r_v < r < r_{-2}$ while closed circles correspond to $r_{-2} < r < r_{200}$. Unlike N-body simulations, our self-similar model does not fit the trend proposed by Hansen & Moore for $r < r_{-2}$. This reveals a shortcoming of the model.

in our Figure 3-2, while there is a clear trend between the local velocity anisotropy and the logarithmic slope of the density profile, that trend does not match the derived relationship. Note though that our model, just as the Aquarius simulation claimed, does show deviations from the Hansen & Moore trend for $r_{-2} < r < r_v$. In our model, this deviation is caused by a vanishing radial velocity dispersion. For simulated halos, other effects like non-sphericity or non-self-similarity may also play a role.

The self-similar model's inability to match the amplitude of the velocity anisotropy seen in N-body simulations reveals a weakness in the model. Clearly, it is unphysical for all particles in a particular shell to have the same amplitude of angular momentum and the same radial velocity. In reality, a given shell should have a radial velocity dispersion and should have a distribution of angular momentum that evolves with time. This possibility will be discussed again in Section 3.5.

3.4.2 Pseudo-Phase-Space Density Profile

Here we analyze the pseudo-phase-space density profiles ρ/σ^3 and ρ/σ_r^3 for galactic size halos, where $\sigma^2 \equiv \sigma_r^2 + \sigma_t^2$. Taylor and Navarro claimed that the pseudo-phase-space density roughly follows the power law $r^{-1.875}$ for all halos (Taylor & Navarro, 2001). Surprisingly, this power law matches predictions made by Bertschinger (1985) for purely radial self-similar collapse onto a spherical top hat perturbation. Taylor and Navarro's claim has been verified numerically (Navarro et al., 2010; Rasia et al., 2004; Dehnen, 2000; Faltenbacher et al., 2007; Vass et al., 2009; Wang & White, 2009), however recently the highest resolution simulations have seen evidence for departures from this power law near their innermost resolved radii (Ludlow et al., 2010).

Based on the analysis in Section 3.3, we expect the power law exponent to depend on $\{n, \varpi\}$ for $r/r_{ta} \ll y_0$. With model parameters $\{n, \varpi\}$ which give $\rho \propto r^{-1}$ for galactic size halos, the extended secondary infall model predicts $\rho/\sigma^3 \propto \rho/\sigma_r^3 \propto r^{-5/2}$. This is expected for a virialized halo ($\varpi > 0$) with $\rho \propto r^{-1}$. For $y_0 \ll r/r_{ta} \ll r/r_v$, the model predicts $\rho/\sigma^3 \propto r^{-2}$ if the radial velocity dispersion dominates and $\rho/\sigma^3 \propto r^{-1/2}$ if the tangential velocity dispersion dominates.

In the left panels of Figure 3-3, we plot ρ/σ^3 and ρ/σ_r^3 for galactic size halos with

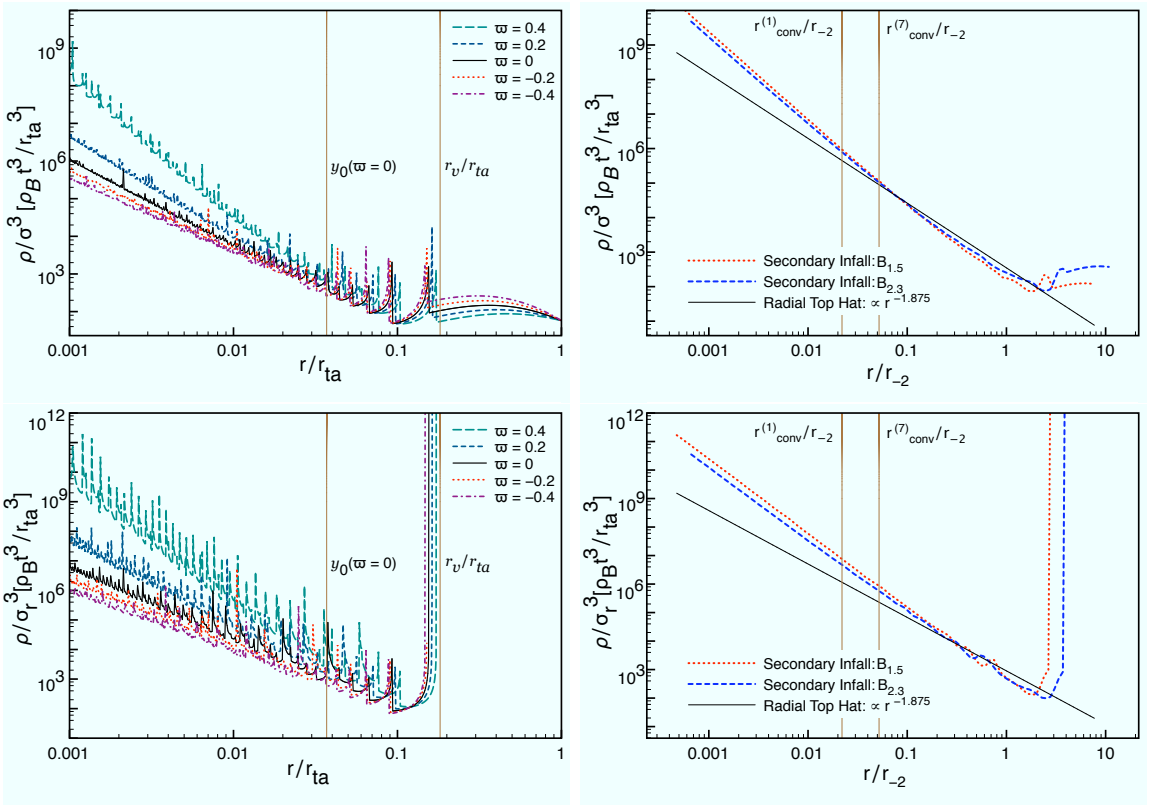

Figure 3-3: The left panels show ρ/σ^3 and ρ/σ_r^3, for a self-similar halo with model parameters $n = .77$, $p = 2n$, $B_{1.5} = 0.39$, and varying ϖ. The numerically calculated slopes match analytic predictions. First pericenter passage (y_0) for $\varpi = 0$ and the virial radius (r_v) are labeled for clarity. The right panels shows the smoothed pseudo-phase-space density profiles, with the radius scaled to r_{-2}, for model parameters that give good agreement to density profiles from galactic size simulated halos. We also plot the radial top hat prediction. The self-similar model predicts that simulations should see deviations from the radial top hat power law at $r/r_{-2} \sim 3 \times 10^{-2}$ for ρ/σ^3 and deviations at $r/r_{-2} \sim 10^{-1}$ for ρ/σ_r^3. The convergence radii for the Aquarius halo Aq-A-2 (Navarro et al., 2010) are labeled for reference.

varying ϖ. In the right panels, we plot the smoothed pseudo-phase-space densities, with the radius scaled by r_{-2}, for model parameters that give good agreement with density profiles from simulated galactic size halos. In addition, we overlay the radial top hat solution. Scaling the radius to r_{-2} causes the first pericenter (y_0) of both models to roughly overlap, leading to less difference in the amplitude of the pseudo-phase-space density at small radii.

The left panels show that the asymptotic slopes vary with ϖ. The numerically

computed slopes match analytic predictions. The panels for ρ/σ_r^3 blow up at radii close to the virial radius since σ_r vanishes. The right panels should be compared to Figure 13 of (Navarro et al., 2010). The extended secondary infall model predicts that simulations of galactic size halos should see significant deviations from Taylor and Navarro's claim at $r/r_{-2} \sim 3 \times 10^{-2}$ when analyzing ρ/σ^3 and $r/r_{-2} \sim 10^{-1}$ when analyzing ρ/σ_r^3. Looking at the residuals in Figure 13 of (Navarro et al., 2010), this prediction seems plausible. If higher resolution simulations do not show deviations from Taylor and Navarro's claim, then this secondary infall model would be proven incorrect since the model cannot consistently reproduce both the density and velocity profiles of simulated halos.

As shown in Section 3.3, for cosmological initial conditions ($n < 2$), ρ, σ_t^2 and σ_r^2 have power laws that are independent of initial conditions and torqueing parameters in the regime $y_0 \ll r/r_{ta} \ll r_v/r_{ta}$. This implies that the pseudo-phase-space density is universal on these scales. This universality on intermediate scales may have played a role in Taylor and Navarro's initial claim.

Figure 3-4 shows the difference of the pseudo-phase-space density power law exponent from the radial top hat solution, on small scales, as a function of model parameters n and ϖ. The range in n corresponds to $10^9 < M/M_\odot < 10^{15}$. The range in ϖ ensures that all orbits are bound. According to the extended secondary infall model, positive ϖ is necessary for $n > .5$ in order to have $\rho \propto r^{-1}$ on small scales (Zukin & Bertschinger, 2010a). If all halos have $\rho \propto r^{-1}$ on small scales, then halos with $M > 10^9 M_\odot$ will have $\rho/\sigma^3 \propto r^{-5/2}$ while halos with $M < 10^9 M_\odot$ will have pseudo-phase-space density exponents that vary with halo mass. If on the other hand, ϖ is constant for all halos, then as Figure 3-4 shows, the power law will vary with mass.

3.5 Discussion

N-body simulations have revealed a wealth of information about the velocity profiles of dark matter halos. In an attempt to gain intuition for their results, we've

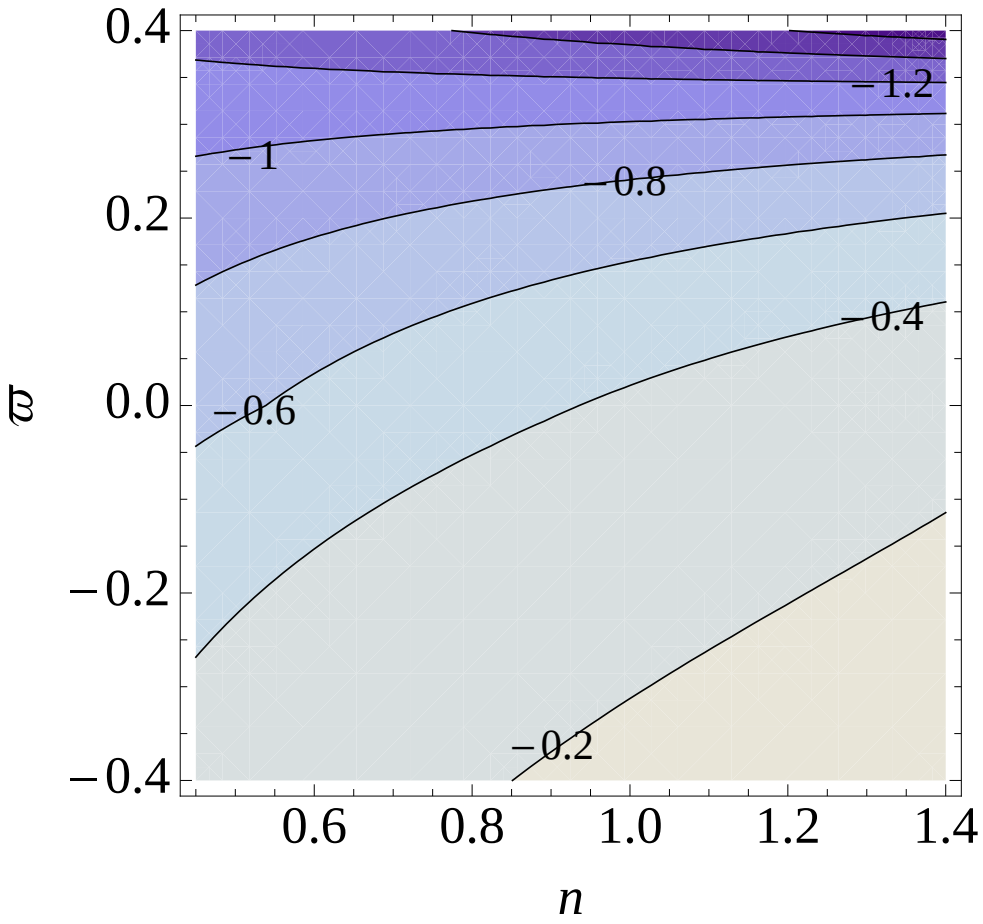

Figure 3-4: A contour plot of $d\ln(\rho/\sigma^3)/d\ln r + 1.875$, which shows the deviation in the pseudo-phase-space density power law exponent, at small scales, from the radial top hat solution.

used a generalized self-similar secondary infall model which takes into accounts tidal torques. The model assumes that halos self-similarly accrete radially cold mass shells. Moreover, each shell is composed of particles with the same amplitude of angular momentum. While the model is simplistic, it does not suffer from resolution limits and is much less computationally expensive than a full N-body simulation. Moreover, it is analytically tractable. Using this model we were able to analytically calculate the radial and tangential kinetic energy profiles for $r/r_{ta} \ll y_0$ and $y_0 \ll r/r_{ta} \ll r/r_v$, where y_0 is the dimensionless radius of first pericenter passage, r_v is the virial radius, and r_{ta} is the current turnaround radius.

It is clear from our analysis that angular momentum plays a fundamental role in

determining the velocity structure of the halo. The amplitude of angular momentum at turnaround sets the transition scale (y_0) between different power law behaviors in the tangential and radial kinetic energy profiles. Also, for collapsed objects today ($n < 2$), ϖ, the parameter that quantifies how particles are torqued after turnaround, influences the slopes of both the radial and kinetic velocity dispersions at small radii. Moreover, both the amplitude of angular momentum at turnaround and ϖ affect the asymptotic value of the velocity anisotropy profile at small radii.

For $\varpi < 0$, the self-similar halo is not virialized on small scales since the radial and tangential kinetic energy is dominated by mass shells which have not had time to virialize. On the other hand, for $\varpi \geq 0$, the halo is virialized since the dominant mass shell have had time to virialize. As shown in Chapter I, $\rho \propto r^{-1}$ requires $\varpi > 0$ for $M/M_{\odot} > 10^9$. Hence, positive ϖ is favored in order to reproduce N-body simulation density profiles. Quantifying ϖ requires analyzing N-body simulations and is beyond the scope of this work. However constraining ϖ with simulations will provide a test for this extended secondary infall model.

Our model predicts that the pseudo-phase-space density profile is universal on intermediate and large scales. This could potentially play a role behind the claimed universality of the pseudo-phase-space density (Taylor & Navarro, 2001). Since we do not understand how ϖ depends on halo mass, it is impossible to rule out universality on small scales, since ϖ can potentially conspire to erase initial conditions. However, if galactic size halos have $\rho \propto r^{-1}$, then regardless of universality, the model predicts $\rho/\sigma^3 \propto r^{-5/2}$. While hints of deviations from the radial top hat solution have been seen in recent simulations (Ludlow et al., 2010), higher resolution simulations are needed to better test the model.

While our self-similar model has its clear advantages, it is also unphysical. First, all particles in a given mass shell have the same radial velocity. This leads to caustics. The same tidal torque mechanisms which cause a tangential velocity dispersion (Hoyle, 1951), should give rise to a radial velocity dispersion. Second, while qualitatively similar, the comparison of the model's predicted velocity anisotropy to N-body simulation results reveals that our treatment of angular momentum is too simplistic.

The model predicts too many radial orbits at large radii and too many circular orbits at small radii. In reality, each shell is composed of a distribution of angular momentum that evolves with time. In order to properly take these two effects into account, one would need a statistical phase space description of the halo that includes sources of torque. Ma & Bertschinger (2004) provided such an analysis in the quasilinear regime. Therefore, a natural extension of this secondary infall model, which could potentially reproduce both position and velocity space information of N-body simulations, would be to generalize Ma & Bertschinger's analysis to the nonlinear regime and impose self-similarity.

Chapter 4

Universality in Dark Matter Halos

4.1 Introduction and Background

N-body simulations have revealed that the density (ρ) (Navarro et al., 1997, 1996) and pseudo-phase space density (ρ/σ^3) profiles (Navarro et al., 2010; Ludlow et al., 2010) of pure dark matter halos are approximately universal. Universality, in this context, means that aside from scalings in amplitude and size, these profiles follow the same shape regardless of halo mass, initial conditions, merger history and environment. This empirical finding implies that information is lost. One way for the system to lose information is through dynamical processes like diffusion. Another way occurs while post-processing the halos where for instance calculating a halo's density profile involves averaging over all angular information. In this Chapter we will analyze the origin of this universality by trying to understand the role that dynamical processes and phase-space averaging plays. We use numerical and analytic techniques. While this Chapter does not give the complete answer, it gives new perspectives and provides promising ways to further explore the question of universality.

Diffusion takes place in systems where the mean free path is much smaller than the size of the system of interest. For example, in the sun, the mean free path for a photon is approximately 1 cm while the radius of the sun $\sim 7 \times 10^{10}$ cm. A canonical example to describe diffusion, that will be informative for later parts of this Chapter,

is Brownian motion. We'll restrict ourself to motion in one dimension for convenience. Generalizing to three dimensions is straightforward. A particle suspended in a heat bath has the following equation of motion:

$$\frac{dv}{dt} = -\gamma v + \Gamma(t) \tag{4.1}$$

where v is the velocity of the particle, γ is the drag coefficient that characterizes the friction acting on the particle when it moves fast relative to the particles in the heat bath, and Γ is a stochastic force associated with random kicks from the heat bath. We further characterize Γ by the following properties:

$$\langle \Gamma(t) \rangle = 0 \qquad \langle \Gamma(t)\Gamma(t') \rangle = 2D\delta(t - t') \; , \tag{4.2}$$

where angle brackets denote time averages and δ is a Dirac delta function. The first equality is expected since stochastic kicks from the heat bath are equally likely in any direction. The second equality states that the stochastic forces acting at two different times are uncorrelated. This is expected since the particles in the heat bath randomize themselves on timescales much smaller than times at which we observe the random-walking particle. The proportionality constant D is known as the diffusion coefficient.

Eq. 4.1 is a Langevin equation and tracks individual particle trajectories. Another description of Brownian motion, which is Eulerian in nature, analyzes evolution at a fixed velocity. The Klimontovich density f_K, defined below, connects the Lagrangian and Eulerian descriptions. We have:

$$f_K(v, t) = \sum_i \delta(v - v_i(t)) \; , \tag{4.3}$$

where v_i is the velocity of the ith particle in the system. Taking an ensemble average of the Klimontovich density's evolution equation, it can be shown that the ensemble phase space density $f \equiv \langle f_K \rangle$ follows a Fokker-Planck equation:

$$\frac{\partial f}{\partial t} = \frac{\partial}{\partial v}\left(\gamma v f + D\frac{\partial f}{\partial v}\right) \tag{4.4}$$

where γ and D were previously defined. The above derivation requires that $\Gamma(t)$ is a gaussian random process and that higher moments, such as $\langle\Gamma(t_1)\Gamma(t_2)\Gamma(t_3)\rangle$ are negligible compared to the second moment defined in eq. (4.2). Assuming an equilibrium solution for the phase space density, we find $D = \gamma kT/m$, where T is the temperature of the heat bath and m is the mass of the particle. This relationship between the drag and diffusive term is expected from the fluctuation dissipation theorem. Assuming $f(t = 0) = \delta(v - v_0)$, the Green's function solution to eq. (4.4) is

$$f(v,t) = \frac{1}{(2\pi\sigma^2(t))^{1/2}} \exp\left(-\frac{[v - v_0(t)]^2}{2\sigma^2(t)}\right) , \tag{4.5}$$

where:

$$\sigma^2(t) = \frac{D}{\gamma}(1 - e^{-2\gamma t}) \tag{4.6}$$

and the centroid satisfies $\dot{v}_0 = -\gamma v_0$. Eq. (4.5) is only valid for constant D. It represents a gaussian whose centroid follows the trajectory expected without stochastic forces. Initially, the standard deviation $\sigma \propto t^{1/2}$, which is expected in the diffusive regime and characteristic of random walks. When $t = 1/\gamma$, however, the drag term becomes important; this causes the width to asymptotically approach the equilibrium temperature of the heat bath, $\sigma^2 = kT/m = D/\gamma$.

Given this description of Brownian motion, where the dynamics forces particles to lose memory of their initial conditions, we now apply the above formalism to dark matter halos. More specifically, we can test the Green's function solution by calculating the standard deviation of different phase space bins as a function of time and comparing with eq. (4.6). Moreover, given the assumptions made in order to derive a Fokker-Planck equation for particles interacting with a heat bath, we can analyze whether those same assumptions apply for the phase space evolution of nonlinear

halos.

In Section 4.2, motivated by the phase space evolution of particles interacting with a heat bath, we calculate the evolution of phase space bins in N-body simulations. In order to understand the results in Section 4.2, we run similar phase space evolution experiments on artificially constructed halos. In Section 4.3 we introduce the Fractal Halo Model – an important component to building artificially constructed halos – that gives a prescription for populating halos with subhalos. We then show the evolution of phase space bins for the artificial halos in Section 4.4. In Section 4.5 we discuss analytic approaches to understanding nonlinear halo evolution and conclude in Section 4.6.

4.2 N-Body Experiments

As described in Section 4.1, the Green's Function solution of the Fokker-Planck equation implies that the standard deviation of a localized phase space bin will evolve as $\sigma \propto t^{1/2}$ for $t\gamma \ll 1$. This is equivalent to claiming that particles which interact with a heat bath initially lose information diffusively. Hence, one way to conclude if particles in dark matter halos lose information diffusively is to measure the evolution of localized phase space bins using cosmological N-body simulations.

4.2.1 Background

Ideally, we would track the evolution of bins in the full six dimensional phase space $\{\boldsymbol{x}, \boldsymbol{v}\}$. However, the bins need to have enough particles > 100 so that Poisson errors are less that 10% and the bins must be localized since we're probing the diffusion coefficient at a phase space point. The localization is also necessary since non-diffusive effects can dominate the evolution of a bin. For instance, if we were to bin in coordinate space and the radial extent of a bin is large, then the difference in force between the edges of the bin based only on the smooth gravitational field will dominate over any stochastic forces. As a result, it is best to bin particles using phase space coordi-

nates that are approximately conserved since diffusive terms will then dominate the bin's evolution.

Dark matter halos at late times are approximately spherically symmetric and have roughly time-independent potentials. Therefore we bin particles only according to their magnitude of angular momentum L and energy E and neglect all other phase space variables. Without wanting to resort to simulations with billions of particles, we can increase the number of particles in each bin by ensemble averaging over halos. In practice this means choosing all halos within a certain mass range, calculating every particle's energy and angular momentum relative to the center of each particle's respective halo, and binning this set of $\{E, L\}$. Note that ensemble averaging over halos makes the assumption of constant L more valid. More specifically, an ensemble averaged halo will be spherically symmetric since there are no preferred directions in the universe.

4.2.2 Simulation and Analysis Details

To perform the N-body simulations, we generate uniform resolution initial conditions with GRAFIC2 (Bertschinger, 2001) at a redshift of $z = 127$, evolve the particles to $z = 0$ using an unreleased version of GADGET (Springel, 2005), and identify halos using SUBFIND (Springel et al., 2001). Since particles in N-body simulations – even for the highest resolution cosmological simulations – have masses of $\sim 10^4 M_\odot$, particles will undergo artificial numerical relaxation. The convergence study by Power et al. (2003) showed that the mass profile of individual halos converge at radii $r > r_{\rm conv}$. The convergence radius $r_{\rm conv}$ is found by equating the two-body relaxation time $t_{\rm rel}/t_{\rm orb} = (N/\ln N)$ with the Hubble time, where $t_{\rm orb}$ is the orbital time at $r_{\rm conv}$ and N is the number of particles internal to $r_{\rm conv}$. Note that this study only looked at the convergence properties of the internal mass profile.

For the purposes of phase-space evolution, artificial two-body relaxation is particularly important because it leads to diffusive-like behavior of phase space bins. In order

to make sure that artificial numerical effects are not responsible for the trends we measure with N-body simulations, we performed six different cosmological simulations of varying resolution. Three of the simulations were the same realization of a periodic 50 Mpc box, with $\{128^3, 256^3, 512^3\}$ particles respectively. The last three simulations were different realizations of $\{25, 75, 100\}$ Mpc periodic boxes all with 512^3 particles. To have good timing resolution, we output ~ 90 snapshots from $z \sim 0.2$ to today. Each snapshot contains every particle's position, velocity, potential, a unique ID, as well as the force acting on that particle. The unique ID allows particles to be tracked through time.

Given the simulation snapshots as well as the group catalog, it is then straightforward to track the evolution of phase space bins. First we pick out all particles in halos of mass $10^{12} M_\odot/h < M < 10^{13} M_\odot/h$ from the group catalog. We then trace these particles back to $z \sim 0.2$ and sort particles according to their energy E and angular momentum L into equal mass bins. Since we analyze halos of different size, we normalize each particle's energy by $v_{\rm max}^2$ and each particle's angular momentum by $r_{\rm max} v_{\rm max}$, where $v_{\rm max}$ is the maximum circular velocity of each halo (at $z = 0$) and $r_{\rm max}$ is the radius at which this occurs. These values are calculated by SUBFIND and stored in the group catalog. In addition, we choose $z \sim 0.2$ since most halos only grow through minor mergers afterward (Fakhouri et al., 2010). Major mergers and violent relaxation, which will be mentioned in Section 4.5, complicate the analytic framework significantly. We associate each binned particle at $z \sim 0.2$ with a binID. Then for later snapshots, after identifying each particle and their bin, we compute each bin's mean and standard deviation of E and L.

Before showing results, it is important to briefly mention a technical aside. In order to calculate a given particle's energy and angular momentum relative to the halo it is necessary to know the halo's center as well as central potential. Both of these quantities are calculated using a Shrinking Spheres approach, which is typical in the simulation community. First the center of mass of all the particles in a given halo is

calculated. Then we calculate a new center of mass based on all particles within the virial radius of the first center of mass. We then iterate this procedure, shrinking the radius each time by 10% and using the previously calculated center. We stop once the number of particles counted $\sim 10\%$ the total number of particles in the halo. We did this for each of our snapshots. We then take the central potential to be the average potential of all of these innermost particles. The above routine reproduced the centers of all halos calculated using SUBFIND to within 3 softening lengths. Since halos are not spherically symmetric, this method is meant to identify the center of the halo with the most concentrated region.

4.2.3 Results

In Figures 4-1 and 4-2, the evolution of the mean (left column) and standard deviation (right column) of E (upper row) and L (lower row) for a random set of phase space bins is shown with thin lines. In the figures, t_i is the time corresponding to the first analyzed snapshot ($z \sim 0.2$) where the phase space is binned, and H_0 is the hubble parameter. All standard deviations have been normalized to the same value at $z = 0$ in order to better see the trends. The thick lines in the right column of both figures correspond to eq. (4.6) – the Fokker Planck expectation of the evolution of a phase space bin's standard deviation – with γ chosen to give the 'best' fit by eye. Figure 4-1 shows the evolution of phase space bins for a low resolution simulation of a 50 Mpc box with 128^3 total particles while Figure 4-2 is calculated using a higher resolution simulation of a 50 Mpc box with 512^3 total particles. We've decomposed phase space into the same number of bins for both simulations and have set up initial conditions so that both simulations are realizations of the same universe.

The evolution of the average E and L is a proxy for drag terms. This is equivalent to measuring the frictional damping (γv in eq. 4.4) in Brownian motion. In both simulations, most bins maintain a constant L. This implies that an ensemble averaged halo is approximately spherically symmetric. The high L bins lose angular momentum, while the very low L bins gain. The high L bins correspond to particles in the

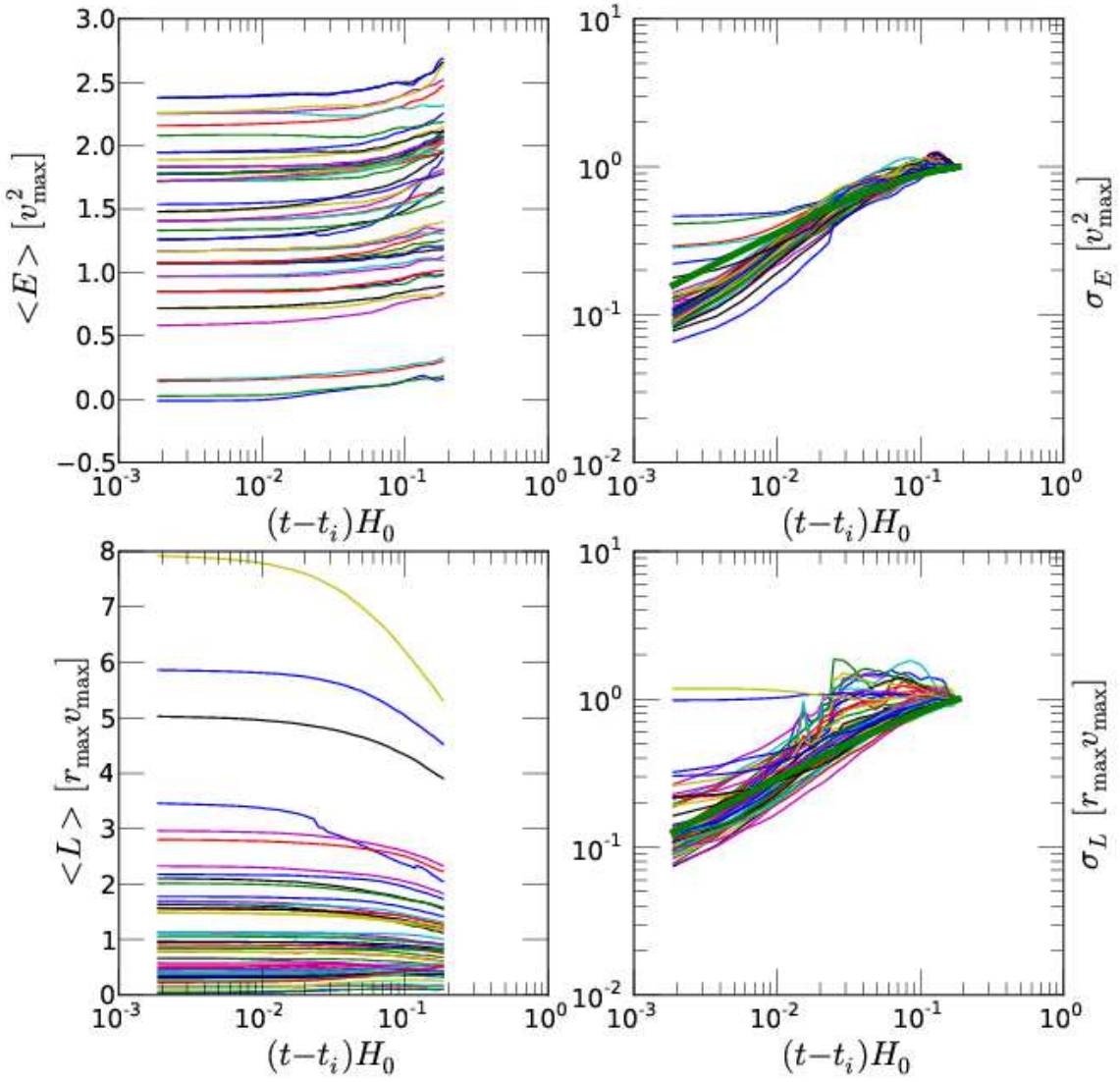

Figure 4-1: Evolution of the mean (left column) and standard deviation (right column) of E and L for a random set of phase space bins (shown with thin lines). The standard deviations have all been normalized to the same value today. The thick line in the right column figures corresponds to $\sigma \propto (1 - e^{-2\gamma t})^{1/2}$, which is expected for Fokker Planck behavior. The parameter γ was chosen to give the 'best' fit by eye. The above was calculated using a low resolution cosmological simulation of a 50 Mpc box with 128^3 particles.

outskirts of the halos. Their tidal forces play a large role and particles can either be disassociated from the halo or fall deeper into the halos. Since the particles examined are all part of the halo, then we are selectively choosing the particles that remain bound. Hence, they have either lost or maintained their same angular momentum,

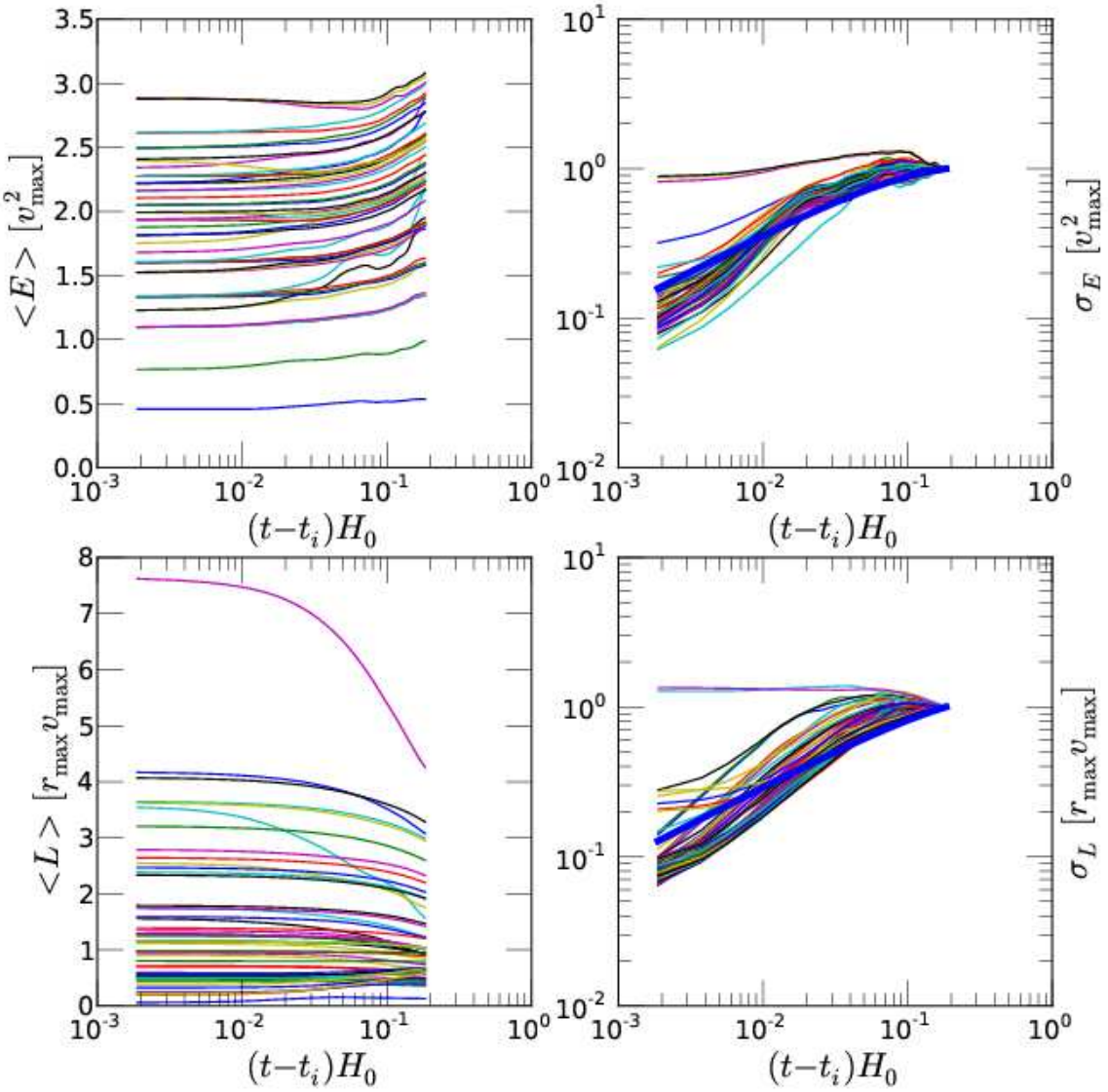

Figure 4-2: Evolution of the mean (left column) and standard deviation (right column) of E and L for a random set of phase space bins (shown with thin lines). The standard deviations have all been normalized to the same value today. The thick line in the right column figures corresponds to $\sigma \propto (1 - e^{-2\gamma t})^{1/2}$, which is expected for Fokker Planck behavior. The parameter γ was chosen to give the 'best' fit by eye. The above was calculated using a high resolution cosmological simulation of a 50 Mpc box with 512^3 particles.

leading to the observed decrease. For the very low L bins, particles can only gain angular momentum, hence the observed increase.

Both simulations show that the average E of all bins slightly increases with time. Since we only bin particles associated with the smooth component of the $z = 0$ halos, this slight increase may be a result of substructures kicking the smooth component to higher energies as they fall deeper into the potential well.

The evolution of σ_L looks approximately the same for both simulations. The higher resolution figure has smoother bin evolution, as expected, since each bin contains more particles. In addition, both simulations show evidence for diffusive-like behavior initially, followed by a plateauing where – analogous to the Brownian motion case – the bin reaches the system's 'angular momentum temperature.' The evolution of σ_E looks different in both simulations, however. While there is diffusive-like behavior initially, followed by a plateau in both cases, the plateau occurs more quickly in the simulation with more particles. The simulation with more particles has a smaller softening length and more power on small scales in the initial conditions, which implies particles feel larger forces. Hence this discrepancy is a result of the larger forces, which causes the higher resolution particles to reach the 'equilibrium temperature' more quickly. More importantly, this implies that close interactions play a large role in the evolution of a particle's energy. This may not be surprising given that the Coulomb logarithm of momentum-transfer cross sections implies that interactions are important at all scales smaller than the system size. It would be informative to see how the best fit D and γ for evolution in L and E depend on softening length and number of particles.

4.2.4 Summary

The above results imply that N-body simulations lose information diffusively when ensemble and phase-space averaged. This is not expected. For the Brownian motion example discussed previously, the stochastic force has a correlation time that is small compared to the time in between observations. For a globular cluster, the local potential in the neighborhood of each star fluctuates on time scales much smaller than an orbital time. For particles in a halo, the force is dominated by the smooth halo, substructure and external tides. These sources do not fluctuate on short time

scales, making the above results surprising. In the remaining sections of this Chapter, we'll discuss different approaches to understanding this counter intuitive behavior.

4.3 Fractal Halo Model

As described above, diffusion takes place in simulated dark matter halos. However, understanding the source of this diffusion is difficult since a given N-body simulation takes into account all interactions and different competing effects cannot be independently adusted. One way to gain intuition for the physical mechanisms causing diffusion is to evolve particles in artificially constructed halos, where the different potential sources of diffusion can be controlled. From a simplistic point of view, there are three potential sources of diffusion. The shape of the halo, as well as external tidal fields, can cause diffusion in angular momentum and substructure can cause diffusion in both energy and angular momentum. One of the ingredients necessary to construct these artificial halos is the spatial distribution of substructure. The Fractal Halo Model which was developed by Ed Bertschinger and will be discussed below, gives a prescription for calculating the spatial distribution of substructure. Parts of the description below were heavily borrowed from a set of notes by Ed.

4.3.1 Background and Formalism

The Fractal Halo Model assumes that a given halo can be decomposed into a smooth component and subhalos. We impose that each subhalo is a scaled version of the parent halo and can therefore be similarly decomposed into a smooth component and subhalos with the decomposition continuing ad infinitum, as in a fractal. Figure 4-3 shows a schematic representation.

More formally, we can represent the density ρ of an nth level halo (ρ_n), where $n = 0$ (4) is the top (bottom) of the pyramid depicted in Figure 4-3, recursively as:

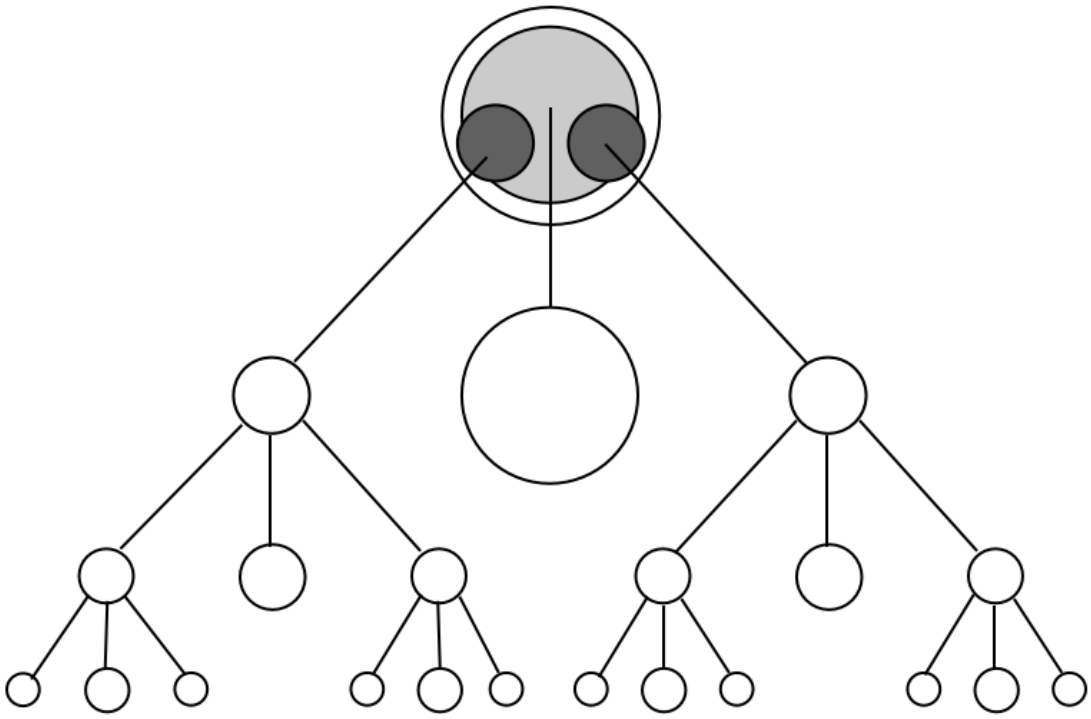

Figure 4-3: A schematic representation of the Fractal Halo Model.

$$\rho_n(\boldsymbol{x}) = \rho_d(\boldsymbol{x}) + A \sum_i \rho_{n+1}\left(\frac{\boldsymbol{x} - \boldsymbol{x}_{i,n}}{b}\right) \tag{4.7}$$

In the above ρ_d is the density for the diffuse component, $A < 1$ and $b < 1$ are constants that scale the amplitude of the density and size of the subhalos, and $\boldsymbol{x}_{i,n}$ labels the center of the ith subhalo for level n. Note that eq. (4.7) enforces that all subhalos for the level n halo have identical mass and size. This is not physical since parent halos have been shown to have subhalos with a distribution of masses (Springel et al., 2008). However it is a good starting point and can be generalized in the future. For example, A and b could be random variables drawn from some specified distributions, and this may still be analytically tractable.

The fractal halo's density depends on the diffuse density distribution ρ_d and the random locations of subhalos $\boldsymbol{x}_{i,n}$. In order to determine the probabilistic distribution that governs the location of subhalos, we'll assume that at each level, an ensemble

average over subhalos gives a universal profile $\bar{\rho}$. More formally:

$$\langle \rho_n(\boldsymbol{x}) \rangle = \bar{\rho}(\boldsymbol{x}) \qquad \text{for all } n \tag{4.8}$$

Next we impose that subhalos occupy their parent halo as a Poisson point process with spatial density $p(\boldsymbol{x})$ chosen so that eq. (4.32) is satisfied. For a Poisson process, the probability to find a subhalo centered in d^3x about $\boldsymbol{x}$ is $p(\boldsymbol{x})d^3x$. In addition, for a Poisson process (Scherrer & Bertschinger, 1991), the single sum appearing in eq. (4.7) when ensemble averaged becomes:

$$\langle \sum_i \rangle = \int d^3x_{i,m} p(\boldsymbol{x}_{i,m}). \tag{4.9}$$

The spatial probability density p has the following normalization:

$$N \equiv \int d^3x \; p(\boldsymbol{x}) \tag{4.10}$$

where N is the average number of subhalos at each level. Taking an ensemble average of eq. (4.7) and using eqs. (4.8-4.9), we find:

$$\bar{\rho}(\boldsymbol{x}) = \rho_d(\boldsymbol{x}) + A \int d^3x' p(\boldsymbol{x}') \bar{\rho} \left(\frac{\boldsymbol{x} - \boldsymbol{x}'}{b} \right). \tag{4.11}$$

Since eq. (4.11) involves the convolution of the spatial probability density $p(\boldsymbol{x})$, it is easiest to solve for $p(\boldsymbol{x})$ in Fourier space algebraically, take the inverse Fourier transform, and use eq. (4.10) as a consistency check. Using the following Fourier convention:

$$p(\boldsymbol{x}) = \int \frac{d^3k}{(2\pi)^3} \; p(\boldsymbol{k}) \; e^{i\boldsymbol{k}\cdot\boldsymbol{x}} \qquad p(\boldsymbol{k}) = \int d^3x \; p(\boldsymbol{x}) \; e^{-i\boldsymbol{k}\cdot\boldsymbol{x}} \tag{4.12}$$

and taking the Fourier transform of eq. (4.11), we find:

$$Ab^3 p(\boldsymbol{k}) = \frac{\bar{\rho}(\boldsymbol{k}) - \rho_d(\boldsymbol{k})}{\bar{\rho}(b\boldsymbol{k})} \; . \tag{4.13}$$

Taking the limit as $k \to 0$, and assuming the total mass of the halo M is finite, we

find:

$$M = \frac{M_d}{1-\epsilon}, \qquad \epsilon \equiv NAb^3 \tag{4.14}$$

where M_d is the mass of the diffuse component of the halo and ϵ is the mass fraction of the halo in substructure. In order to solve for $p(\boldsymbol{k})$ in eq. (4.13), the last ingredient is to specify $\rho_d(\boldsymbol{k})$. As a starting point, we'll assume:

$$\rho_d(\boldsymbol{x}) = (1-\epsilon)\bar{\rho}(\boldsymbol{x}) \; . \tag{4.15}$$

As we discuss further in Section 4.3.4, eq. (4.15) is not physical, since tidal destruction will leave little substructure intact close to the center of a parent halo. However, it is a good starting point and generalizations will be discussed in Section 4.3.5. Combining eqs. (4.13-4.15), we find:

$$p(\boldsymbol{k}) = \frac{N\bar{\rho}(\boldsymbol{k})}{\bar{\rho}(b\boldsymbol{k})} \; . \tag{4.16}$$

Eq. (4.16) fully specifies the spatial substructure distribution. In Section 4.3.3, we discuss numerically calculating the substructure distribution as well as its analytic behavior. We then compare to results from N-body simulations in Section 4.3.4 and discuss possible generalization in Section 4.3.5.

4.3.2 Relevance of Model

With the above model in mind, it is worthwhile to ask whether describing halos as fractals is realistic. Springel et al. (2008) used a suite of cosmological 'Zoom-In' simulations to analyze subhalo density distributions and sub-subhalo distributions. With their high resolution Zoom-In halo, they were able to identify multiple generations of subhalos within subhalos. For one subhalo in particular, they found four generations of substructure, which is equivalent to the $n = 4$ level described in the Fractal Halo Model. The number of generations identified is limited by the resolution of the simulation.

Subhalo density profiles, according to their paper, were well described by both Einasto and NFW profiles. This is consistent with the Fractal Halo Model which claims that subhalo density distributions are a scaled down version of their parent halos (eq. 4.8). In order to make the Fractal Halo Model more realistic, however, subhalos should have a distribution of scaling parameters b so that subhalos do not all have the same mass.

The mass function of sub-subhalos follows the same functional form as the mass function for subhalos. However it is smaller in amplitude – by a factor of 2 to 3 – relative to the predicted value based on scaling arguments using the parent halo. In the context of the Fractal Halo Model, this would mean that the $N_{n+1} = N_n/2$, where N_n is the average number of subhalos at level n.

Another probe analyzed by Springel et. al. was the mass fraction of sub-subhalos in subhalos. They compared this value to the mass fraction of subhalos in the main halo internal to the radius where the main halo's density equals the subhalo's density. They found that the mass fraction of sub-subhalos in subhalos was once again consistently smaller than the mass fraction of subhalos in the main halo. Note that they did not analyze the spatial distribution of sub-subhalos because of what I'm assuming is low number statistics.

The reason for these trends, according to Springel et. al., is that sub-subhalo abundances are decreased relative to the main halo because of tidal effects. In addition sub-subhalos are not replenished by the infall of new sub-subhalos, like in the case of the parent halo. As a result, the Fractal Halo Model, needs to be generalized in order to better reflect the nature of dark matter halos. Note however that the model is useful since it provides an upper limit on the influence of sub-subhalos.

4.3.3 Implementation and Analytic Behavior

In order to calculate $p(\boldsymbol{k})$, given eq. (4.16), we need to specify the scaling parameter b that sets how spatially large substructure is relative to the parent halo, the universal density profile $\bar{\rho}$, and the average number of subhalos N for each level. We'll choose an NFW profile (Navarro et al., 1997) with a exponential cutoff beyond the virial radius so that the total mass is finite and $\bar{\rho}(\boldsymbol{k} = 0)$ does not diverge. We have:

$$\bar{\rho}(\boldsymbol{y}) = \frac{\rho_s}{y(1+y)^2} \exp\left[-\frac{y^2}{2(3c)^2}\right] \ . \tag{4.17}$$

In the above, $\boldsymbol{y} \equiv \boldsymbol{r}/r_s$, $y = |\boldsymbol{y}|$, r_s is the scale radius where the NFW profile becomes isothermal, ρ_s is four times the density at the scale radius, and $c \equiv r_v/r_s$, where r_v is the virial radius of the halo. In Figure 4-4, we plot the Fourier transform of $\bar{\rho}$ in blue, for $c = 10$. This concentration value is motivated by values measured from N-body simulations (Navarro et al., 2010). The behavior of the density's Fourier transform is straightforward to understand. Since the density is spherically symmetric, the three dimensional Fourier transform can be reduced to a one dimensional integral. More specifically:

$$\begin{aligned} \bar{\rho}(z) &= 4\pi\rho_s r_s^3 \int_0^\infty \frac{y^2}{y(1+y)^2} \frac{\sin(yz)}{yz} \exp\left[-\frac{y^2}{2(3c)^2}\right] dy \\ &\approx 4\pi\rho_s r_s^3 \int_0^{\pi/z} \frac{y^2}{y(1+y)^2} \exp\left[-\frac{y^2}{2(3c)^2}\right] dy \end{aligned} \tag{4.18}$$

where $z \equiv kr_s$. In going from the first to second line, we approximate $\sin(yz)/yz$ as a filter which cuts off all contributions to the integral for $yz > \pi$. The integral in eq. (4.18) is proportional to the internal mass below a radius π/z. Therefore for an NFW profile, we expect $\bar{\rho}(z) \propto 1/z$ for $z \sim 1$ and $\bar{\rho}(z) \propto 1/z^2$ for $z \gg 1$. This is explicitly show in Figure 4-4 with the dashed red and dotted yellow lines, respectively. Moreover, the constant behavior for $z \ll 1$ reflects the finite mass of the halo.

Since $\bar{\rho}(k) \propto 1/k^2$ for $kr_s \gg 1$, we expect (based on eq. 4.16) that $p(kr_s) = Nb^2$ for

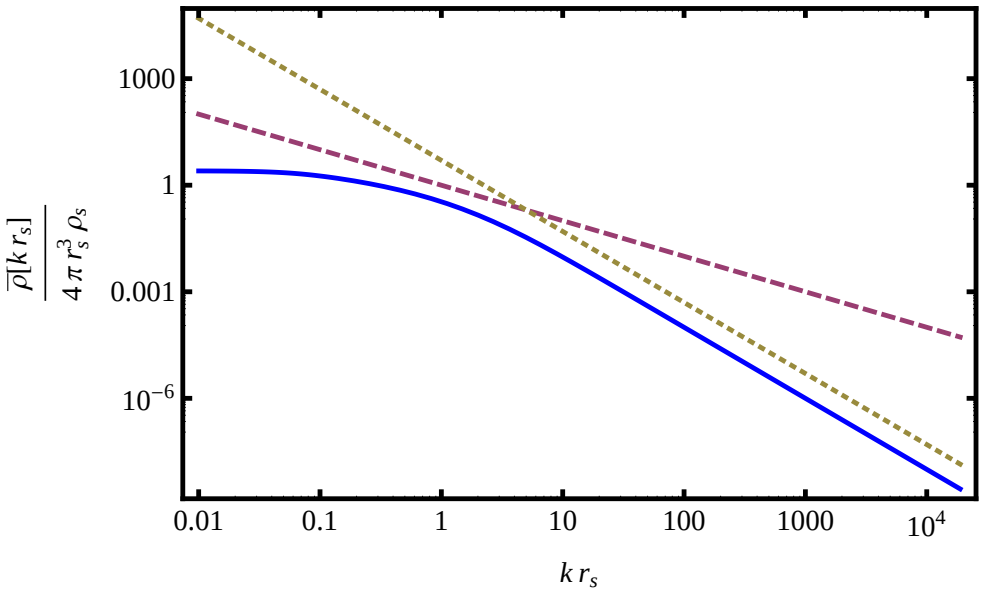

Figure 4-4: The Fourier transform of our cutoff NFW profile $\bar{\rho}$ is shown in solid blue. The red dashed line shows the $\propto 1/k$ behavior near $kr_s \sim 1$, while the dotted yellow line shows the $\propto 1/k^2$ behavior for $kr_s \gg 1$. For the above calculation, we've chosen $c = 10$.

$bkr_s \gg 1$. This leads to a singularity at the origin for the spatial probability density. However, this contribution of power at infinitely large wavenumbers is unphysical since N-body simulations cut off power at wavenumbers larger than the simulation's Nyquist frequency, which is defined by the box size and the number of particles. To mimic this effect, and avoid singularities, we redefine $p(k)$ to be:

$$p(\boldsymbol{k}) = \frac{N\bar{\rho}(\boldsymbol{k})}{\bar{\rho}(b\boldsymbol{k})} \exp[-k^2 s^2/2] \tag{4.19}$$

where s is the simulation's softening length. In Figure 4-5, for $b = 0.1$ and $s = 10^{-3}\ r_s$, we plot $p(k)$ in blue. Given the analytic structure of $\bar{\rho}(k)$ discussed above, it is straightforward to understand the behavior of $p(k)$. However, the scalings in different wavenumber regimes will depend on b. Without the high wavenumber cutoff, for $b = 1$, $p(k) = N$ over all wavenumbers. For $b \ll 1$, $p(k)$ will transition through the following power laws $\{k^0, k^{-1}, k^{-2}, k^{-1}, k^0\}$ as k increase, with $p(k) = \{N, Nb^2\}$ for $kr_s\{\ll, \gg\}1$. As b increases, the range over which $p(k) \propto k^{-2}$ disappears, followed by

the range over which $p(k) \propto k^{-1}$. For $b = 0.1$, which is analyzed in Figure 4-5, the k^{-2} behavior is not present, but the constant trends at both low and high wavenumber are present (b^2 shown by the dotted yellow line), as well as the $1/k$ behavior (red dashed line).

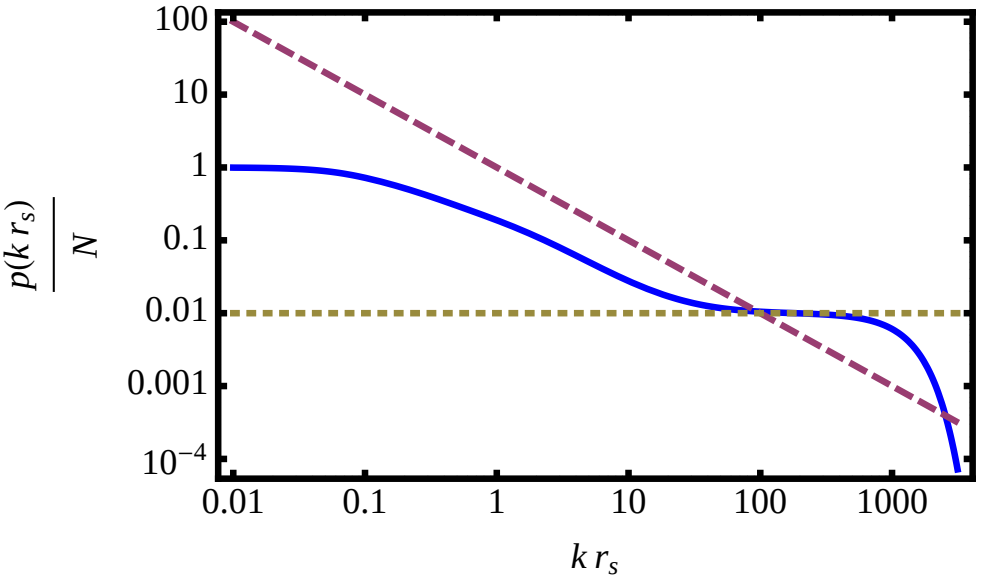

Figure 4-5: The Fourier transform of the spatial substructure probability density p is shown in solid blue. The red dashed line shows the $\approx 1/k$ behavior that spans a range in wavenumber that depends on the scaling parameter b. The Fourier transform asymptotes to b^2 (dotted yellow line) before the exponential cutoff. For the above calculation, we've chosen $c = 10$, $b = 0.1$, and $s = 10^{-3} r_s$.

Next we take the Fourier transform of $p(k)$ and show the spatial probability density for substructure in Figure 4-6, for $c = 10$, $b = 0.1$, and $s = 10^{-3} r_s$, in solid blue. Since we've imposed spherical symmetry, we can once again understand the behavior of this curve analytically by reducing the three dimensional inverse Fourier transform into a one dimensional integral over an approximate filter. We have:

$$p(y) = \frac{1}{2\pi^2}\frac{1}{r_s^3}\int_0^\infty z^2 p(z)\frac{\sin(yz)}{yz}dz \approx \frac{1}{2\pi^2}\frac{1}{r_s^3}\int_0^{\pi/y} z^2 p(z)dz \tag{4.20}$$

where once again $y \equiv r/r_s$ and $z \equiv k r_s$. As expected, since $p(z) \propto 1/z$ over a large

part of the domain for this particular choice of b, we should expect $p(y) \propto 1/y^2$. This is depicted explicitly in Figure 4-6 with the dashed red line. For $y \sim 10$, the behavior transitions to $1/y^3$ since $p(z)$ is approximately constant at $z \sim 0.1$. The behavior for $y \ll 1$ is caused by the gaussian cutoff introduced in Fourier space. Multiplying a function in Fourier space by a gaussian will cause a convolution of a gaussian with the inverse Fourier transform of the function. Hence, we see the gaussian behavior at small scales. The sharp cutoff at large scales is caused by the gaussian cutoff we imposed in real space that enforced the halo to have finite mass.

It is interesting to mention that the derived $1/y^2$ scaling gives rise to the same amount of mass in substructure for all radial bins of the same width. Since there is less volume in radial shells at smaller radii, there will be more overlap of substructure at smaller radii. Note though that this scaling does not hold for all b, as mentioned above. For $b \ll 1$ there will be a region where $p(y) \propto 1/y$.

Last, in Figure 4-7 we show how varying a subhalo's size relative to the parent halo (b) affects the spatial probability density. The area under each curve is equal to the probability of finding a single subhalo in a given radial range. Most of the subhalos will occupy the outer parts of the halo. However, there is a fairly significant probability of substructure existing in the interior of the halo when $x \ll r_s$. This is not physical however, since the model doesn't take into account tidal affects. Moreover, the bump at small radii is associated with the gaussian cutoff in Fourier space. Since the same cutoff is used for every b, the bumps occupy the same radial range. Note that because of artificial two body relaxation in N-body simulations, scales below $x/r_s \sim 0.01$ (for the highest resolution simulations) are not trusted because quantities like the circular velocity have not converged. The red, blue and yellow curves correspond to $b = \{0.5, 0.1, 0.05\}$ respectively. As expected, models with larger b will give a larger contribution at small radii since their $p(k)$ did not drop off as significantly with larger wavenumber. In addition, models with larger b flatten out more quickly on large scales since their $p(k)$ transition away from a constant value at a longer wavenumber.

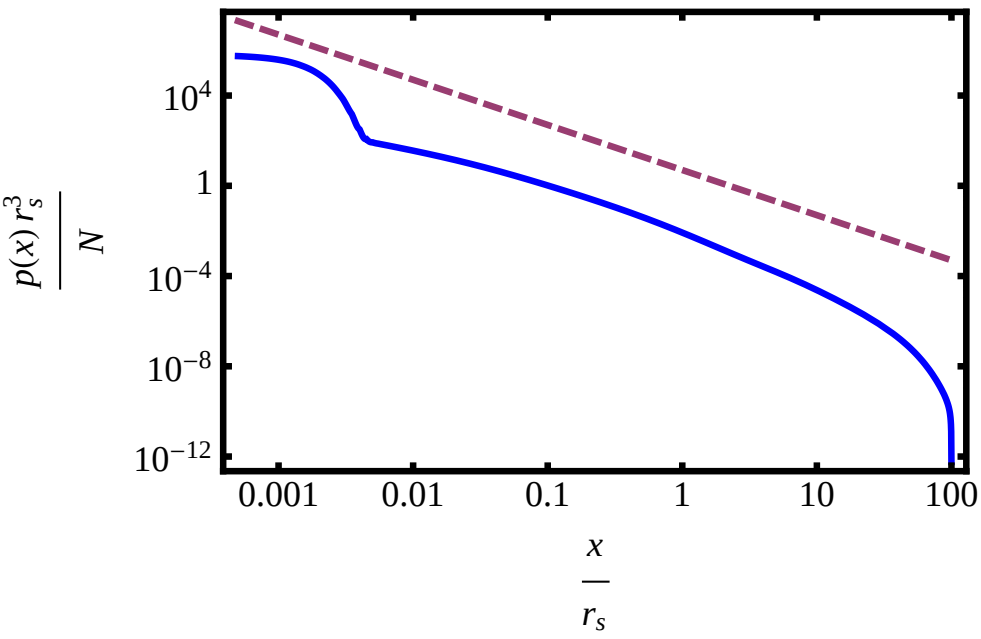

Figure 4-6: The spatial probability density $p(x)$ for the location of substructures is shown in solid blue. The red dashed line shows the $\approx 1/k^2$ behavior. The structure at small scales is caused by the high wavenumber gaussian cutoff we introduced. The structure at large scales is caused by the gaussian filter we applied to the original density distribution so that the halo has finite mass. For the above calculation, we've chosen $c = 10$, $b = 0.1$, and $s = 10^{-3} r_s$.

4.3.4 Comparison with N-body Simulations

Given the above predictions for the subhalo spatial distribution, it would be informative to compare to results from N-body simulations. In 2008, a suite of zoom-in high resolution simulations, known as the Aquarius Project, were performed that simulated a cosmological box with varying resolution. Internal to the Lagrangian volume of a galactic size halo, the simulation had high resolution, using particle masses $\sim 10^4 M_\odot/h$. External to the Lagrangian volume, the simulation had poorer resolution, using larger particle masses the further away the particles were from the high resolution halo.

With this set of simulations, as well as a subhalo finder, Volker Springel and his collaborators calculated the spatial distribution of substructure (Springel et al., 2008).

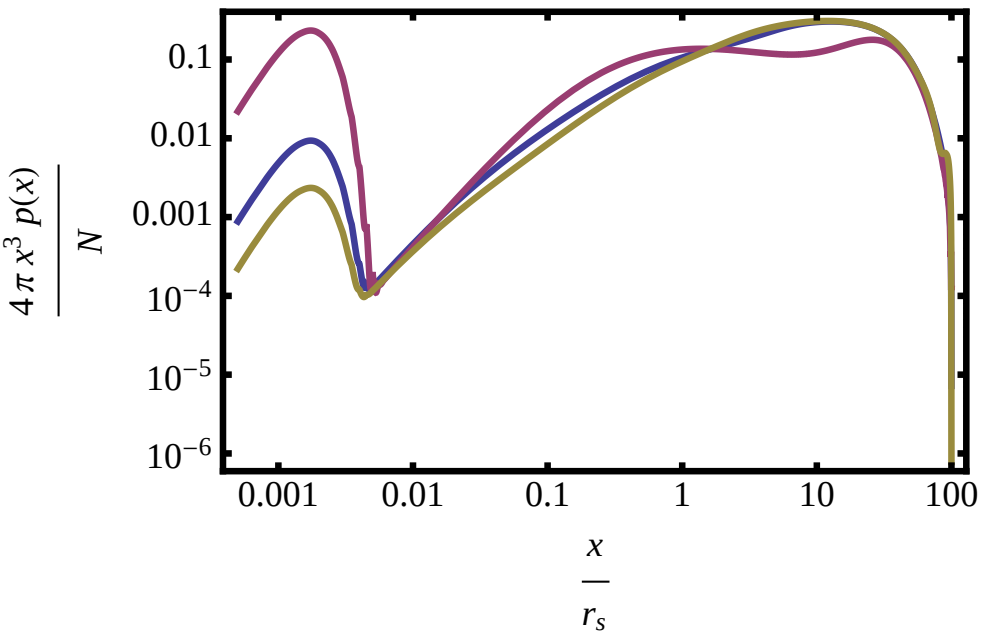

Figure 4-7: The variation of the spatial probability density for different size subhalos. The red, blue and yellow curves correspond to $b = \{0.5, 0.1, 0.05\}$ respectively. The area under each curve is equal to the probability of finding a single substructure in a given radial range. While most subhalos will occupy the outskirts of the halo, the excess in probability on small scales is unphysical and related to the model not taking into account tidal disruption. The peak at small radii is sourced by the gaussian cutoff imposed in Fourier space.

They found that the substructure number density profiles – equivalent to the quantity $p(x)$ discussed above – for subhalos in different mass bins follows an Einasto profile, shown by the dashed green line in Figure 4-8. The plot is normalized to the average number of substructures within r_{50} of the simulation. The fractal halo model's prediction for $b = \{0.5, 0.1, 0.05\}$ is shown in solid red, blue and yellow, respectively. While the distributions resemble each other in the outskirts of the halo, the fractal halo model overestimates the probability for substructure to lie in the interior of the halo because the model does not take into account tidal disruption. In addition, for the scales of interest shown in Figure 4-8, different values of b will give power laws at least as steep as $1/r$. Since the empirical Einasto profile however already asymptotes to shallower logarithmic slopes at $\sim$ 100 kpc, we expect the Fractal Halo model to

generically over predict the amount of substructure for all values of b.

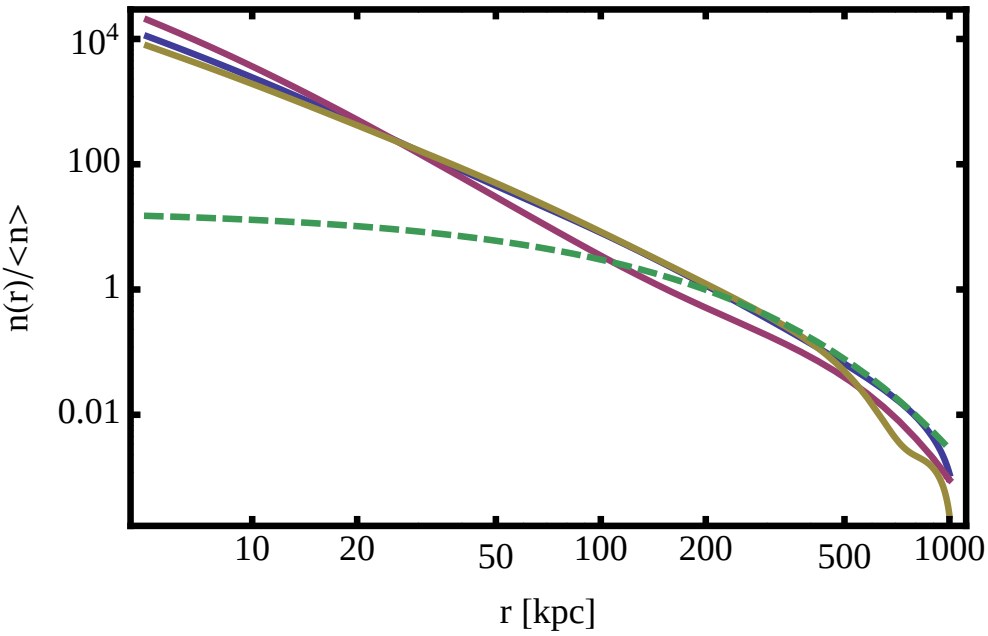

Figure 4-8: The substructure number density profile, normalized to the mean number of substructures within r_{50} for the Fractal Halo model, shown in red, blue and yellow for $b = \{0.5, 0.1, 0.05\}$ respectively. The analogous quantity, shown in dashed green, calculated using a suite of high resolution N-body simulations. While the distributions resemble each other in the outskirts of the halo, the fractal halo model overestimates the probability for substructure to lie in the interior of the halo because the model does not take into account tidal disruption.

4.3.5 Possible Generalization

Since the Fractal Halo Model overestimates the probability for substructure to lie in the interior of the halo, as we see with Figure 4-8, it would be informative to add new physics to the model in order to understand trends seen in N-body simulations. The key assumption that leads to this overestimate is shown in eq. (4.15). There we imposed that the density of the diffuse component was proportional to the density of the universal profile for all radii. Since the assumed universal density profile is not constant with radius, subhalos will be tidally disrupted by different amounts depending on their location. More specifically, subhalos close to the center will be

disrupted more than subhalos in the outskirts. One way to take this into account is to generalize eq. (4.15) in the following way:

$$\rho_d(\boldsymbol{x}) = [1 - \epsilon(x)]\bar{\rho}(\boldsymbol{x}) \tag{4.21}$$

where now ϵ is a function of position. Physically we'd expect $\epsilon \to 0$ as $x \to 0$. Moreover, since we reproduced the spatial distribution seen in N-body simulations in the outskirts of the halo, we should maintain that $\epsilon = \text{const}$ for $x \gg r_s$. Note that this would not decrease N at successive levels. It would simply change the spatial distribution of substructure.

A natural way to calculate $\epsilon(x)$ is to first start with our initial solution $\epsilon = \text{const}$ and break up the halo into spherical bins. For each bin, tabulate and store the mass in the smooth component and the mass in substructure. Then, assuming a single subhalo occupies the center of a given bin, calculate what fraction of the subhalo's mass is tidally lost because of the smooth potential, take that fraction away from the mass in substructure and add it to the mass in the diffuse halo. Then, given the new tabulated mass in the diffuse and subhalo components for each spherical bin, it is straightforward to convert this to a local density and infer $\epsilon(x)$. I plan to pursue this generalization, as well as allow for N to vary with n, in the future.

4.4 Simple Numerical Experiments

Here we discuss the simple numerical experiments we perform using artificially constructed halos. These experiments attempt to give intuition about the diffusion, in N-body simulations, discussed in Section 4.2. For these artificially constructed halos, we control the shape, substructure distribution, as well as the ensemble averaging. Hence we can independently vary different potential sources of diffusion in order to gauge each source's importance.

4.4.1 Background and Implementation

Our artificial halos, as described in Section 4.3, are composed of a diffuse density component ρ_d and substructure ρ_s. Both the diffuse component and the substructure are described by NFW profiles. While the substructure is a scaled version of the NFW profile, in both size and amplitude, we allow the diffuse component to be triaxial. Note that we do not place subhalos within subhalos. In other words, we truncate the model at $n = 1$. Including sub-subhalos will be pursued in the future. The NFW profile is reproduced below for convenience:

$$\bar{\rho}(\boldsymbol{y}) = \frac{\rho_s}{y(1+y)^2} \exp\left[-\frac{y^2}{2(3c)^2}\right] \tag{4.22}$$

where $\boldsymbol{y} \equiv \boldsymbol{r}/r_s$, r_s is the scale radius of the NFW profile, ρ_s is proportional to the density at the scale radius and we've introduced an exponential cutoff past the virial radius $r_v \equiv cr_s$ so that the halo has finite mass. Given the above profile, and imposing a total mass fraction ϵ in substructure, the density distribution for an individual subhalo centered at $\boldsymbol{x}_i \equiv \boldsymbol{y}_i r_s$, according to the Fractal Halo Model, is:

$$\rho_s(\boldsymbol{y}) = \frac{\epsilon}{Nb^3}\, \bar{\rho}\left(\frac{\boldsymbol{y} - \boldsymbol{y}_i}{b}\right) \tag{4.23}$$

where N is the number of subhalos and b is the scaling parameter described in the prior section. For a triaxial diffuse component, we impose axis ratios a_i. Then defining:

$$m^2(\boldsymbol{y}, \tau) = a_1^2 \sum_i \frac{y_i^2}{\tau + a_i^2}, \tag{4.24}$$

where τ is introduced for later convenience, we describe the diffuse component by:

$$\rho_d(\boldsymbol{y}) = (1 - \epsilon)\, \bar{\rho}\big[m(\boldsymbol{y}, 0)\big]\ . \tag{4.25}$$

To construct an artificial halo, we choose specific axis ratios, sample the spatial density distribution for subhalos (calculated in the previous section) N times and set the other phase space variables for the center of each subhalo. The $\{\theta, \phi\}$ coordinates are randomly chosen to uniformly sample 4π steradians. The velocity in each direction

is sampled from a gaussian distribution with standard deviation equal to the circular velocity – for a particle orbiting only a spherical diffuse component – at that radius. We will generalize this isotropic velocity distribution to allow for anisotropy in the future. If we want an ensemble of halos, we repeat this process multiple times. The subhalo centers evolve as if they were point particles orbiting only the diffuse component. Taking into account interactions between subhalos does not influence the results. In addition, tidal affects, as mentioned in the prior section, are ignored.

Given an ensemble of artificially constructed halos, we now mimic the analysis in Section 4.2 and construct bins in $\{E, L\}$ space. We first choose the phase space information for $\sim 10^7$ test particles. This number is approximately the same number of particles analyzed in the high resolution N-body simulations, hence we expect similar statistics for each bin. The radius of each particle is sampled from a distribution set by the NFW profile. The $\{\theta, \phi\}$ coordinates uniformly sample 4π steradians and the velocity in each direction is sampled from a gaussian distribution with standard deviation equal to the circular velocity – at the particle's radius – for an NFW profile. In addition, each particle is randomly assigned to a halo of the ensemble.

Given the full phase space information of every particle, and the halo to which every particle is assigned, it is straightforward then to calculate each particle's E and L relative to the halo's center. We normalize E and L by $v_{\rm max}^2$ and $r_{\rm max} v_{\rm max}$ respectively, with these values taken from a simulated high resolution halo (Navarro et al., 2010). The gravitational potential is calculated for the artificially constructed halo with substructure, not the ensemble averaged smooth halo. This $\{E, L\}$ phase space is then binned and each particle is tagged with a bin ID. Then all particles are evolved forward, with forces sourced by the diffuse component and subhalos, and the bin statistics – just as in the N-body analysis – are tracked as a function of time. Note that we do not use the same GADGET code to calculate potentials and evolve particles since our forces are derived from smooth halos and subhalos, while the GADGET code's forces are derived from discrete particles.

For completeness, the acceleration $\boldsymbol{A}$ and potential Φ (relative to the center) of a particle at position $\boldsymbol{y}$ caused by the diffuse triaxial halo is given by (Binney & Tremaine, 2008; Chandrasekhar, 1987):

$$A_i(\boldsymbol{y}) = -2\pi G r_s a_1 a_2 a_3 \int_0^\infty \frac{(1-\epsilon)\,\bar{\rho}\big[m(\boldsymbol{y},\tau)\big]}{\sqrt{(\tau+a_1^2)(\tau+a_2^2)(\tau+a_3^2)}} \frac{y_i}{\tau+a_i^2} d\tau \quad (4.26)$$

$$\Phi(\boldsymbol{y}) = \pi G r_s^2 \frac{a_2 a_3}{a_1} \int_0^\infty \frac{\psi[m(\boldsymbol{y},\tau)\big]}{\sqrt{(\tau+a_1^2)(\tau+a_2^2)(\tau+a_3^2)}}\, d\tau \quad (4.27)$$

where:

$$\psi(m) = \int_0^{m^2} dm^2 (1-\epsilon)\bar{\rho}(m) \quad (4.28)$$

The integrand sums the contribution of all shells internal to the outermost surface at $\tau = 0$. Similar to the spherical case, a Birkhoff-type theorem applies for triaxial systems in Newtonian gravity and only mass surfaces interior to $m(\boldsymbol{y}, 0)$ contribute to the force.

4.4.2 Results

With the above framework, in an attempt to mimic the N-body simulation behavior described in Section 4.2, we vary the structure of these artificially constructed halos and keep track of the evolution of a random set of phase space bins. Figures 4-9 through 4-11 each show a grid of four plots. On the left column of each figure we show the evolution of the average E and L for different phase space bins, where t_i is the time at which the particles are initially binned. On the right column of each figure, we show the evolution of the standard deviation in E and L for different bins. Each bin's standard deviation is normalized to its value at the final time. The thick red line is what is expected for Fokker Planck behavior: $\sigma \propto (1 - e^{-2\gamma t})^{1/2}$. We chose γ (for both the spread in L and E) to give the 'best' fit by eye. We ensemble average by assigning particles to one of a possible 400 different halo realizations.

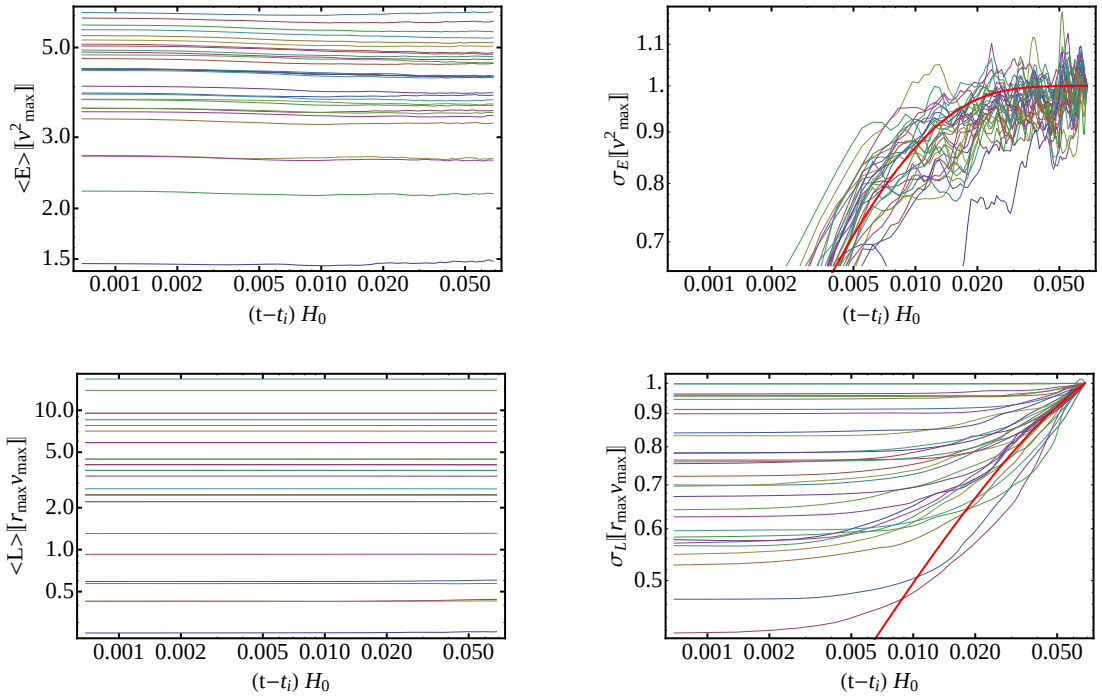

Figure 4-9: The evolution of statistics describing a random set of phase space bins for an artificial halo with 10 subhalos and a spherical diffuse component. The different thin lines represent different bins. The left column shows the evolution of the average E and L of each bin. The right column shows the evolution of the standard deviation in E and L of each bin. The standard deviations are normalized to their value at the final time. The thick red line denotes the expected Fokker Planck behavior.

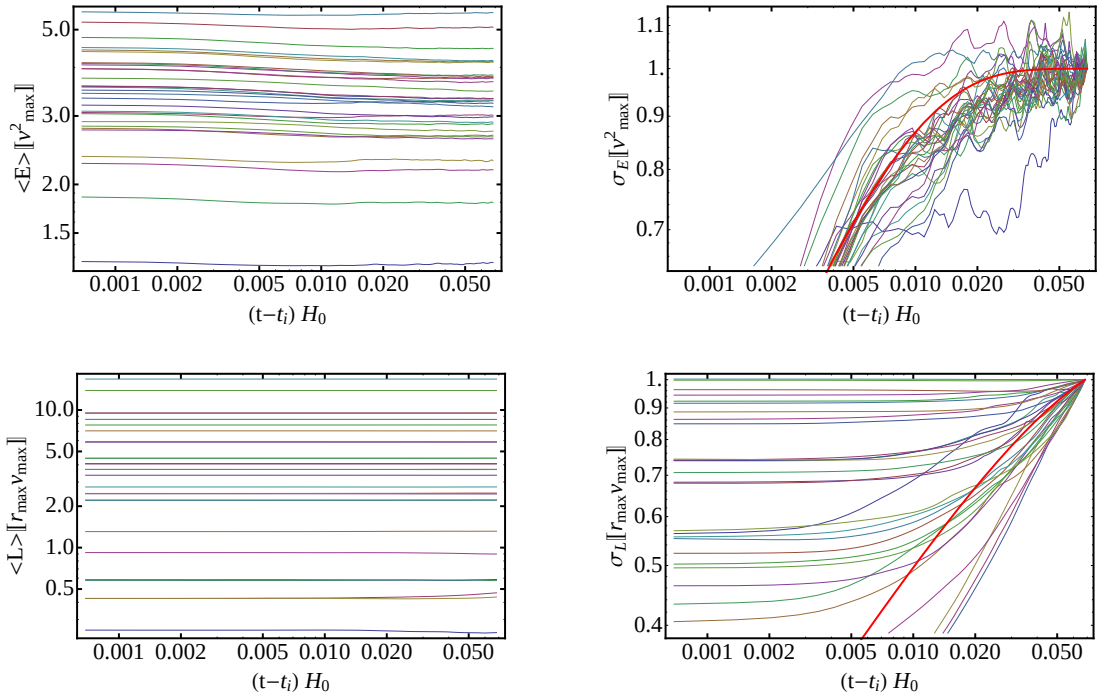

Figure 4-10: The evolution of statistics describing a random set of phase space bins for an artificial halo with 10 subhalos and a triaxial diffuse component. The different thin lines represent different bins. The left column shows the evolution of the average E and L of each bin. The right column shows the evolution of the standard deviation in E and L of each bin. The standard deviations are normalized to their value at the final time. The thick red line denotes the expected Fokker Planck behavior.

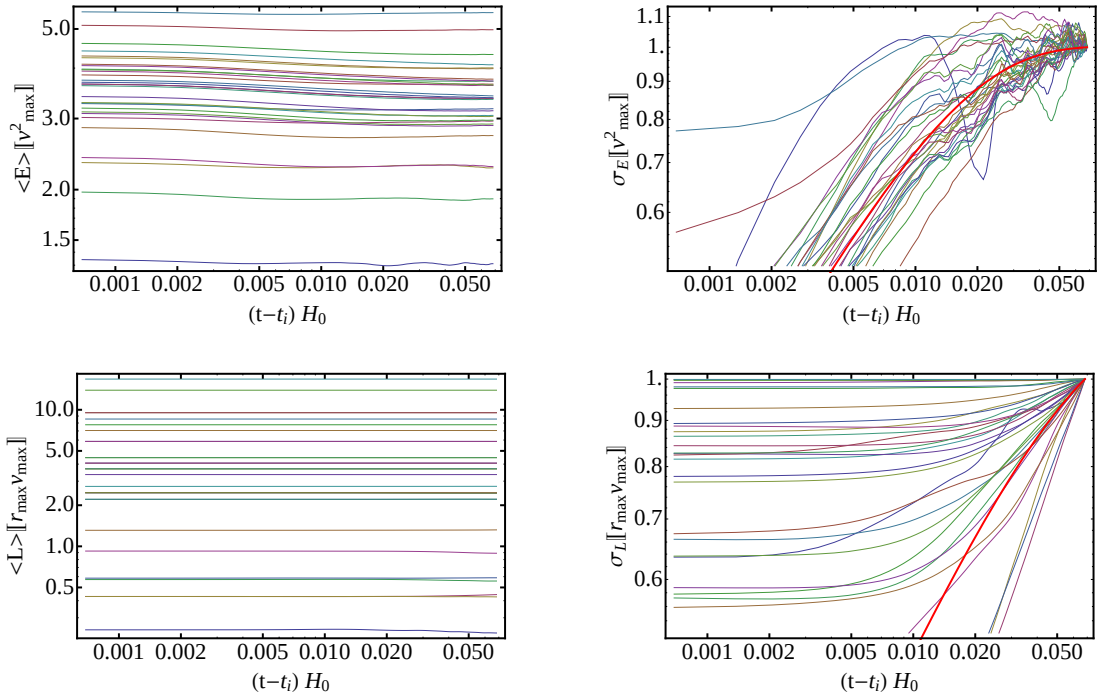

Figure 4-11: The evolution of statistics describing a random set of phase space bins for an artificial halo with 100 subhalos and a triaxial diffuse component. The different thin lines represent different bins. The left column shows the evolution of the average E and L of each bin. The right column shows the evolution of the standard deviation in E and L of each bin. The standard deviations are normalized to their value at the final time. The thick red line denotes the expected Fokker Planck behavior.

Figures 4-9 and 4-10 show the evolution of phase space bins in artificial halos made of 10 subhalos, with a spherical and triaxial diffuse component, respectively. The triaxial component has axis ratios $(1 : 0.85 : 0.7)$. As expected, in both figures, the average E and L do not vary significantly. This is an indication that we have ensemble averaged over enough halos. It is interesting to point out that the average E and L of bins in the artificially constructed halos is larger than those of the simulated halos in Figures 4-1 and 4-2. It is likely that assuming a gaussian isotropic distribution overestimates the energy and angular momentum.

In Figures 4-9 and 4-10 we see similar behavior for σ_E. The bins all diffuse initially and then reach the temperature of the halo and cannot diffuse anymore. This is just as eq. (4.6) predicts. For σ_L, however, bins do not diffuse. It is surprising how little subhalos perturb a particle's angular momentum. Moreover, triaxiality, while it gives rise to more bins that diffuse, does not source enough torque to reproduce the behavior in N-body simulations.

Figure 4-11 shows the evolution of phase space bins in artificial halos made of 100 subhalos, with a triaxial diffuse component. We do not show the case for artificial halos with 100 subhalos and a spherical diffuse component because it does not reveal any new information. Once again, the triaxial component has axis ratios $(1 : 0.85 : 0.7)$. We see similar features to those for the halos with 10 subhalos. Now, however, the diffusion in σ_E takes place for a longer period of time. This is expected. With the same mass fraction in substructure for all halos, the artificial halos with 100 subhalos will give smaller kicks to the particles than the halos with 10 subhalos. Hence, it takes longer for the bins to reach the temperature of the halo. Also note that with more smaller mass subhalos, the angular momentum diffuses less since the system is more spherically symmetric.

4.4.3 Implications and Future Directions

The above analysis implies that triaxiality and substructure do not provide enough torque to account for the angular momentum diffusion measured in simulations. Another possible source of torque is the tidal field from external halos. We can verify this claim using N-body simulations. SUBFIND outputs a group catalog for the N-body simulation at $z = 0$ (Springel et al., 2001). This catalog finds all particles in a given group, where a group is defined using the friends of friends algorithm. Then within each group, all bound structures are identified. The largest bound structure is equivalent to the diffuse component in the Fractal Halo Model while the smaller structures are associated with our subhalos. Therefore, using the group catalog, as well as the snapshot with every particle's full phase space information, it is straightforward to measure the importance of different sources of torque. We simply separately calculate the amplitude of torque in a particular halo at varying radii sourced by the diffuse component τ_d, the subhalos $\tau_{\rm sub}$, and particles outside the group $\tau_{\rm ex}$.

In Figure 4-12, we plot $\tau_d/\tau_{\rm ex}$ in the left column and $\tau_{\rm sub}/\tau_{\rm ex}$ as a function of radius for three different randomly chosen halos (different rows) from one of our high resolution N-body simulations. The first, second and third rows correspond to halos with mass $\{3.5, 1.8, 1.0\} \times 10^{12} M_\odot/h$ respectively. The vertical dashed line shows r_{200} for each halo. For all halos, the external torques are more significant than the torque from subhalos. Moreover, the external torque is non-negligible ($\sim 10\%$) relative to the torque from the diffuse component on scales as small as $r_{200}/10$, where most of the particles reside for a galactic size halo.

This importance of external torques in the nonlinear regime is not stressed in the literature. Normally the total angular momentum of halos is assumed constant in the nonlinear regime since the halo approximately decouples itself from the background (Doroshkevich, 1970; Peebles, 1969). Numerical experiments, in addition, have approximately verified this claim (White, 1984; Book et al., 2011). However, Figure 4-12

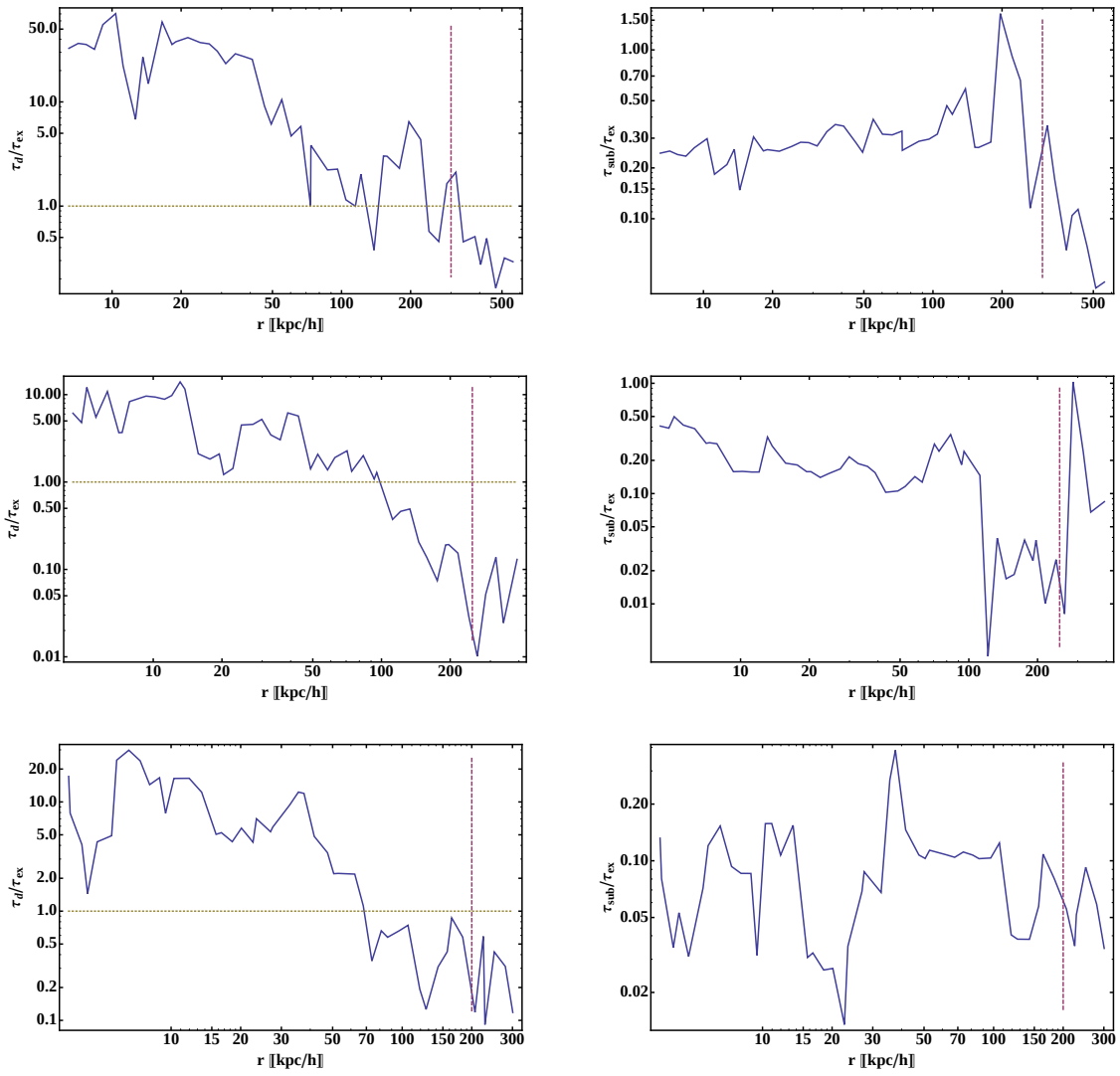

Figure 4-12: In the left column, we plot the ratio of the amplitude of torque from the diffuse component to the torque from particles outside of the halo ($r > r_{200}$). In the right column, we plot the ratio of torque caused by substructure to torque from particles outside the halo. These figures are calculated using one of our high resolution N-body simulations. The different rows correspond to halos of different mass: $\{3.5, 1.8, 1.0\} \times 10^{12} M_{\odot}/h$, from top to bottom. The dashed line in each figure labels r_{200} for each halo.

suggests that the total angular momentum should fluctuate at about the 10% level today. It is reasonable then to expect the halo's angular momentum to fluctuate at higher levels at earlier times, when it is not as relaxed. A more detailed investigation will be pursued in the future but it should be stressed that large scale external tides need to be included in N-body simulations. In other words, small simulated boxes do not represent the dynamics accurately.

The above numerical experiments requires a number of extensions. First, particles need to be sampled from a more accurate phase space distribution. It is possible that particles aren't diffusing because they are moving too fast to couple strongly with the substructure and diffuse components. One way to make sure the particles and subhalos have equilibrated is to only bin phase space and start tracking bin statistics after the particles and subhalos have undergone a few orbits. Another extension necessary is that subhalos need to be sampled from a more accurate spatial distribution. The Fractal Halo Model predicts too many subhalos at small radii because tidal interactions are not taken into account. Subhalos at small radii do not significantly affect the angular momentum of particles at large radii because they orbit on a faster timescale and can be approximated as a spherically symmetric perturbation. The Fractal Halo model also needs to be generalized to allow for a distribution of subhalo masses. This increases the asymmetry in the system and should lead to larger torques. Last, given the importance of external torques, it would be natural to include a model for the large scale tidal field.

4.5 Analytic Modeling

Section 4.2 of this chapter revealed that when projecting the full phase space coordinates of particles in an ensemble-averaged halo onto their energy E and angular momentum L, phase space bins evolve as if the particles were random walking in $\{E, L\}$ space. In Section 4.4, we recreated some aspects of this behavior using more controlled numerical experiments involving artificially constructed halos. This subsec-

tion focuses on building up an analytic framework that describes these trends. First we will give background on the analytic formalism, showing how collisional terms that may give rise to diffusion arise in the evolution of a halo's phase space density. Then we will estimate the amplitude of collisional terms relative to other terms that determine the evolution of the halo's phase space density. Last, we will discuss different approaches to understanding the emergence of random walk behavior in halo evolution.

4.5.1 Background

This section largely follows Section 2 of (Ma & Bertschinger, 2004). We first start with the Klimontovich density f_K, which represents the phase space density for an individual halo.

$$f_K(\boldsymbol{r}, \boldsymbol{v}, t) = m \sum_i \delta_D[\boldsymbol{r} - \boldsymbol{r}_i(t)] \delta_D[\boldsymbol{v} - \boldsymbol{v}_i(t)] \tag{4.29}$$

In the above m is the mass of each particle and $\boldsymbol{r}_i$ and $\boldsymbol{v}_i$ are the radius and velocity of particle i respectively. As is expected, the Klimontovich density satisfies the Vlasov equation.

$$\frac{\partial f_K}{\partial t} + \boldsymbol{v} \cdot \frac{\partial f_K}{\partial \boldsymbol{r}} + \boldsymbol{g}_K \cdot \frac{\partial f_K}{\partial \boldsymbol{v}} = 0 \tag{4.30}$$

where

$$\boldsymbol{g}_K(\boldsymbol{r}, t) = -Gm \sum_i \frac{\boldsymbol{r} - \boldsymbol{r}_i}{|\boldsymbol{r} - \boldsymbol{r}_i|^3} = -G \int d^6 w' f_K(\boldsymbol{w}', t) \frac{\boldsymbol{r} - \boldsymbol{r}'}{|\boldsymbol{r} - \boldsymbol{r}'|} \tag{4.31}$$

and we've introduced $\boldsymbol{w} = \{\boldsymbol{r}, \boldsymbol{v}\}$ for convenience. Equation (4.30) is exact, conserves phase space volume, and keeps track of all phase space information in the halo. In other words, given f_K at a particular instance of time, we have enough information to solve for f_K at another time. Doing so would be equivalent to performing an N-body simulation. In order to make progress analytically, one approach is to perform an averaging procedure in the hope that the evolution of the averaged quantities will

depend on less information. This averaging approach is commonly applied when systems have many ($\sim$ Avogadro's number) degrees of freedom.

For instance, consider a gas of thermalized identical particles interacting at room temperature. Understanding the velocity of an individual gas particle requires knowing the particle's initial position and velocity as well as the position and velocity of every other particle that collided with it. On the other hand, the velocity distribution of an ensemble of gas particles requires only knowledge of the temperature of the gas.

With this statistical approach in mind, we define the following ensemble average:

$$f(\boldsymbol{w}, t) = \langle f_K(\boldsymbol{w}, t) \rangle \ . \tag{4.32}$$

An ensemble average can either be thought of as averaging over different instances of a given halo, or averaging over different halos in a large cosmological volume. Since eq. (4.30) is not linear in f_K, because of the gravitational field's dependence on the phase space density, we also define the ensemble average of a product of Klimontovich densities. We have:

$$\langle f_K(\boldsymbol{w}_1, t) f_K(\boldsymbol{w}_2, t) \rangle \equiv \delta_D(\boldsymbol{w}_1 - \boldsymbol{w}_2) f(\boldsymbol{w}_1, t) + f_2(\boldsymbol{w}_1, \boldsymbol{w}_2, t) \tag{4.33}$$

where:

$$f_2(\boldsymbol{w}_1, \boldsymbol{w}_2, t) \equiv f(\boldsymbol{w}_1, t) f(\boldsymbol{w}_2, t) + f_{2c}(\boldsymbol{w}_1, \boldsymbol{w}_2, t) \ . \tag{4.34}$$

In eq. (4.33), the Dirac delta function corresponds to the case where two points lie on top of one particle. Distinct particles give rise to f_2, which can be rewritten to be of the form shown in eq. (4.34). The two-point correlation function f_{2c}, defined in eq. (4.34), represents the additional probability that the two particle's phase space coordinates influence each other. Given eqs. (4.32-4.34) and taking an ensemble average of eq. (4.30), we find:

$$\frac{\partial f}{\partial t} + \boldsymbol{v} \cdot \frac{\partial f}{\partial \boldsymbol{r}} + \boldsymbol{g} \cdot \frac{\partial f}{\partial \boldsymbol{v}} = -\frac{\partial}{\partial \boldsymbol{v}} \cdot \boldsymbol{F} \ , \tag{4.35}$$

where

$$\boldsymbol{g}(\boldsymbol{r}, t) = -G \int d^6 w' f(\boldsymbol{w}', t) \frac{\boldsymbol{r} - \boldsymbol{r}'}{|\boldsymbol{r} - \boldsymbol{r}'|^3} \tag{4.36}$$

and the correlated force density $\boldsymbol{F}$ is:

$$\boldsymbol{F}(\boldsymbol{w}, t) = -G \int d^6 w' f_{2c}(\boldsymbol{w}, \boldsymbol{w}', t) \frac{\boldsymbol{r} - \boldsymbol{r}'}{|\boldsymbol{r} - \boldsymbol{r}'|^3} \tag{4.37}$$

In the above, we've assumed that all forces are relative to the center. In other words, the halo is always centered at $\boldsymbol{r} = 0$. Notice that the ensemble-averaged phase space density f no longer satisfies the Vlasov equation. More specifically, because of the collisional term $\boldsymbol{F}$, evolution no longer conserves the phase space volume. This should be expected. Before averaging, f_K describes a Hamiltonian system where every particle in the halo evolves according to the same potential. After ensemble averaging though, every particle that samples f comes from a different halo and hence evolves according to a different potential. Therefore, the system is no longer Hamiltonian and phase space conservation should not be expected.

Eq. (4.35) is the first equation in the BBGKY hierarchy. In order to solve for f, $\boldsymbol{F}(\boldsymbol{w}, t)$ is required. Knowledge of $\boldsymbol{F}$ requires evolving the second equation in the hierarchy, which in turn depends on the next hierarchical equation. One way to proceed is to close the hierarchy at the nth level by assuming the $(n+1)$st correlation function vanishes. However, for gravitational systems this is not justified in the nonlinear regime because of gravity's tendency to strongly cluster particles. Another possibility is to explicitly solve for $F(\boldsymbol{w}, t)$ from first principles in the quasi-linear regime. This was done in (Ma & Bertschinger, 2004). There they found that a Fokker-Planck equation governed the evolution of f. This is fairly significant and a little surprising. In the quasi-linear regime, each particle deterministically evolves according to a fixed potential. After ensemble averaging, however, deterministic trajectories became

stochastic in nature.

Here we pursue understanding phase space evolution with a different approach. In order to get intuition for the importance of the collisional term ($\boldsymbol{F}$) in eq. (4.35), we calculate it assuming the Fractal Halo Model that was described in detail in Section 4.3. Note that this is not self consistent because the phase space density f and the correlated force density $\boldsymbol{F}$ derived from the Fractal Halo Model will not simultaneosly satisfy eq. (4.35). However, it provides a way to gain better understanding.

4.5.2 Calculating the Correlated Force Density

Reproduced here for convenience, the Fractal Halo Model assumes the density profile for a level n halo can be represented by the following:

$$\rho_n(\boldsymbol{x}) = \rho_d(\boldsymbol{x}) + A \sum_{\{i,n\}} \rho_{n+1} \left(\frac{\boldsymbol{x} - \boldsymbol{x_{i,n}}}{b} \right) \tag{4.38}$$

For definitions and more background, please refer to Section 4.3. If we impose that the ensemble average of all halos, at each level n, gives rise to a universal profile $\bar{\rho}$ and that the location of each subhalo satisfies a Poisson point process, then as previously shown, we can numerically calculate the spatial probability density $p(\boldsymbol{x})$ of substructure.

For a spatial Poisson process, ensemble averages over sums like that shown above are given by:

$$\left\langle \sum_{\{i,m\}} \right\rangle = \int d^3x_{i,m}\, p(\boldsymbol{x}_{i,m}) \tag{4.39}$$

$$\left\langle \sum_{\{i,m\}} \sum_{\{j,n\}} \right\rangle = \int d^3x_{i,m}\, p(\boldsymbol{x}_{i,m}) \int d^3x_{j,n}\, p(\boldsymbol{x}_{j,n}) + N\delta_{ij}\delta_{mn} \int d^3x_{i,m}\, p(\boldsymbol{x}_{i,m}) \tag{4.40}$$

where

$$N \equiv \int d^3x\; p(\boldsymbol{x}) \tag{4.41}$$

is the average number of subhalos at each level. Given the above definitions, it is now straightforward to calculate the two-point correlation function. For now, we will neglect velocity space information. We find:

$$\begin{aligned}
\Big\langle \rho_n(\boldsymbol{x}_1)\rho_n(\boldsymbol{x}_2)\Big\rangle &= \left\langle \left[\rho_d(\boldsymbol{x}_1) + A\sum_{i,n}\rho_{n+1}\left(\frac{\boldsymbol{x}_1-\boldsymbol{x}_{i,n}}{b}\right)\right]\left[\rho_d(\boldsymbol{x}_2) + A\sum_{j,n}\rho_{n+1}\left(\frac{\boldsymbol{x}_2-\boldsymbol{x}_{j,n}}{b}\right)\right]\right\rangle \\
&= \rho_d(\boldsymbol{x}_1)\rho_d(\boldsymbol{x}_2) + A\rho_d(\boldsymbol{x}_2)\int d^3x'\; p(\boldsymbol{x'})\bar{\rho}\left(\frac{\boldsymbol{x}_1-\boldsymbol{x'}}{b}\right) \\
&+ A\rho_d(\boldsymbol{x}_1)\int d^3x'\; p(\boldsymbol{x'})\bar{\rho}\left(\frac{\boldsymbol{x}_2-\boldsymbol{x'}}{b}\right) \\
&+ A^2\left[\int d^3x' d^3x'' p(\boldsymbol{x'})p(\boldsymbol{x''})\bar{\rho}\left(\frac{\boldsymbol{x}_1-\boldsymbol{x'}}{b}\right)\bar{\rho}\left(\frac{\boldsymbol{x}_2-\boldsymbol{x''}}{b}\right)\right. \\
&+ \left. N\int d^3x' p(\boldsymbol{x'})\bar{\rho}\left(\frac{\boldsymbol{x}_1-\boldsymbol{x'}}{b}\right)\bar{\rho}\left(\frac{\boldsymbol{x}_2-\boldsymbol{x'}}{b}\right)\right] \\
&= \bar{\rho}(\boldsymbol{x}_1)\bar{\rho}(\boldsymbol{x}_2) + NA^2\int d^3x' p(\boldsymbol{x'})\bar{\rho}\left(\frac{\boldsymbol{x}_1-\boldsymbol{x'}}{b}\right)\bar{\rho}\left(\frac{\boldsymbol{x}_2-\boldsymbol{x'}}{b}\right)
\end{aligned} \tag{4.42}$$

Therefore, given eqs. (4.33) and (4.34), the two-point density correlation function ρ_{2c} is given by:

$$\rho_{2c}(\boldsymbol{x}_1,\boldsymbol{x}_2) = NA^2\int d^3x' p(\boldsymbol{x'})\bar{\rho}\left(\frac{\boldsymbol{x}_1-\boldsymbol{x'}}{b}\right)\bar{\rho}\left(\frac{\boldsymbol{x}_2-\boldsymbol{x'}}{b}\right)\;. \tag{4.43}$$

The above form is expected since the amplitude of ρ_{2c} depends on how significantly substructures overlap. Since, we impose a gaussian cutoff past the virial radius of $\bar{\rho}$ in order to ensure a finite mass, eq. (4.43) will only be non-negligible when the substructures are close together. Approximately, we find:

$$\rho_{2c}(\boldsymbol{x}_1, \boldsymbol{x}_2) \approx NA^2 \begin{cases} p(\boldsymbol{x}_1) \int d^3x \; \bar{\rho}^2 \left(\frac{\boldsymbol{x}}{b}\right) & \text{if } |\boldsymbol{x}_1 - \boldsymbol{x}_2| \ll br_s, \\ b^3 M \bar{\rho} \left(\frac{|\boldsymbol{x}_2 - \boldsymbol{x}_1|}{b}\right) [p(\boldsymbol{x}_1) + p(\boldsymbol{x}_2)] & \text{if } |\boldsymbol{x}_1 - \boldsymbol{x}_2| \gg br_s, \end{cases} \tag{4.44}$$

where M is the mass of the halo and r_s is the scale radius of the NFW profile. The above approximation assumes that the spatial probability density $p(x)$ does not vary significantly over the subhalos, which is true for $b \ll 1$. Eq. (4.44), together with the analysis of the spatial substructure probability density in Section 4.3 fully characterizes ρ_{2c}.

Given the above we can now move on to calculating the correlated force density $\boldsymbol{F}$ defined in eq. (4.37). We'd like to compare $\boldsymbol{F}$ to $\boldsymbol{g}f$ for different radii in order to determine the importance of collisional terms sourced by substructure. Assuming the following form for the phase space density f:

$$f(\boldsymbol{w}, t) = \frac{\bar{\rho}(r)}{(2\pi)^{3/2}[\sigma_x^2(r)\sigma_y^2(r)\sigma_z^2(r)]^{1/2}} \exp\left(-\frac{v_x^2}{2\sigma_x^2(r)}\right) \exp\left(-\frac{v_y^2}{2\sigma_y^2(r)}\right) \exp\left(-\frac{v_z^2}{2\sigma_z^2(r)}\right) , \tag{4.45}$$

implies that comparing $\boldsymbol{F}$ to $\boldsymbol{g}f$, after integrating over velocity information, is equivalent to comparing $\boldsymbol{F}^\rho \equiv \int \boldsymbol{F} d^3v$ to $\boldsymbol{g}\bar{\rho}$ where:

$$\begin{aligned} \boldsymbol{F}^\rho(\boldsymbol{r}, t) &\equiv -G \int d^3r' \rho_{2c}(\boldsymbol{r}, \boldsymbol{r}', t) \frac{\boldsymbol{r} - \boldsymbol{r}'}{|\boldsymbol{r} - \boldsymbol{r}'|^3} \\ &= -GNA^2 \int d^3r' \int d^3r'' p(\boldsymbol{r}'') \bar{\rho}\left(\frac{\boldsymbol{r} - \boldsymbol{r}''}{b}\right) \bar{\rho}\left(\frac{\boldsymbol{r}' - \boldsymbol{r}''}{b}\right) \frac{\boldsymbol{r} - \boldsymbol{r}'}{|\boldsymbol{r} - \boldsymbol{r}'|^3} . \end{aligned} \tag{4.46}$$

Transforming coordinates to $\boldsymbol{r}' = \boldsymbol{r} + \boldsymbol{x}$ and $\boldsymbol{r}'' = \boldsymbol{r} + \boldsymbol{y}$, we have:

$$\boldsymbol{F}^\rho(\boldsymbol{r}, t) = GNA^2 \int d^3x \int d^3y \; p(\boldsymbol{r} + \boldsymbol{y}) \; \bar{\rho}\left(\frac{y}{b}\right) \bar{\rho}\left(\frac{\boldsymbol{y} - \boldsymbol{x}}{b}\right) \frac{\boldsymbol{x}}{x^3} . \tag{4.47}$$

First consider the interior integral. As discussed above, the integral over the product of densities will only be non-negligible when the separation between halo centers $x \ll br_s$. In this regime, we can put an upper limit of the integral over v. We have:

$$\int d^3y\; p(\boldsymbol{r}+\boldsymbol{y})\; \bar{\rho}\left(\frac{y}{b}\right) \bar{\rho}\left(\frac{\boldsymbol{y}-\boldsymbol{x}}{b}\right) < p(\boldsymbol{r}-\boldsymbol{x}/2) \int d^3y\; \bar{\rho}^2(y/b) \equiv Bb^3 p(\boldsymbol{r}-\boldsymbol{x}/2)\;. \tag{4.48}$$

I've chosen to evaluate the spatial probability density at $\boldsymbol{r}-\boldsymbol{x}/2$ since this is where the two densities overlap the most. Given the above, we can now calculate an upper limit to $\boldsymbol{F}^{\rho}$. We find:

$$\begin{aligned}
\boldsymbol{F}^{\rho}(\boldsymbol{r},t) &< GAB\epsilon \int d^3x\; p(\boldsymbol{r}-\boldsymbol{x}/2)\frac{\boldsymbol{x}}{x^3} \\
&\approx GAB\epsilon \int d^3x\; \left[p(r) - \frac{1}{2}\frac{dp}{dr}\hat{\boldsymbol{r}}\cdot\boldsymbol{x}\right]\frac{\boldsymbol{x}}{x^3} \\
&= -\frac{\pi GAB\epsilon b^2 r_s^2}{3}\frac{dp}{dr}\hat{\boldsymbol{r}} \\
&= -\frac{\pi GB\epsilon^2 r_s^2}{3b}\frac{d\tilde{p}}{dr}\hat{\boldsymbol{r}}\;.
\end{aligned} \tag{4.49}$$

In the above, we've assumed $x \ll r$, which is valid for $b \ll 1$, and limited the integration volume to a radius of br_s, since subhalos separated by more than this distance will have a negligible ρ_{2c}. In addition, we've used the previously defined $\epsilon \equiv NAb^3$, the mass fraction of substructure in the halo, and we've defined $\tilde{p} \equiv p/N$ so that $\int d^3x\; \tilde{p}(x) = 1$. Note that the zeroth order contribution vanishes because of isotropy. This comes about since test particles will be equally likely to be kicked in any direction.

Eq. (4.49) implies that for a fixed mass fraction in substructure ϵ, the amplitude of this collisional term can be increased arbitrarily by decreasing b and keeping Nb^3 constant. In other words, collisions are more important if you split up the substructure into more smaller mass subhalos, because there are more locations where overlap

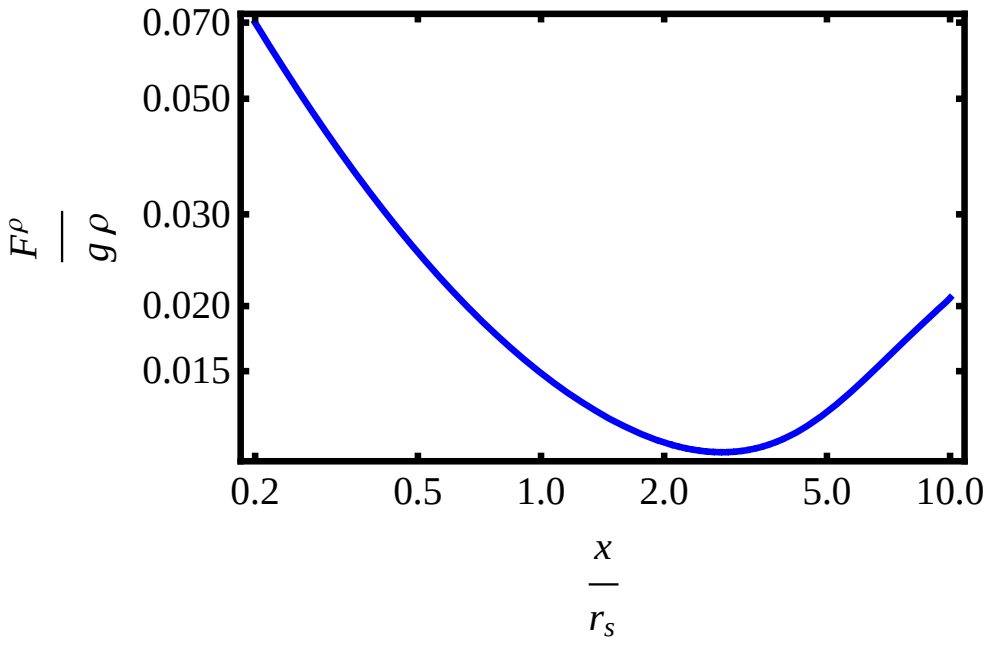

Figure 4-13: The above shows $\boldsymbol{F}^\rho/\boldsymbol{g}\rho$ for $b = 0.1$, $c = 10$ and $\epsilon = 0.1$. In this radial regime, the spatial probability density $dp/dx \propto 1/x^3$ while $\boldsymbol{g}\rho$ transitions from $\propto 1/x^2$ behavior to $\propto \ln x/x^5$ with increasing radius. While the above shows that the collisional term is not important for this set of Fractal Halo model parameters, splitting up the substructure into more smaller mass subhalos will increase the amplitude of $\boldsymbol{F}^\rho$ relative to $\boldsymbol{g}\rho$.

occurs. Note though that the scalings of $\boldsymbol{F}^{\rho}$ will vary with b. It is surprising that eq. (4.49) is purely set by the spatial probability density.

In Figure 4-13, we show the ratio of $\boldsymbol{F}^{\rho}/\boldsymbol{g}\rho$ for $b = 0.1$, $c = 10$ and $\epsilon = 0.1$. We limit the plot to this domain since the approximations used to calculate $\boldsymbol{F}^{\rho}$ break down when $x \sim br_s$. Moreover, as discussed previously, the spatial probability density is not representative of actual halos for $x \ll r_s$. In this radial regime, the spatial probability density $dp/dx \propto 1/x^3$ while $\boldsymbol{g}\rho$ transitions from $\propto 1/x^2$ behavior to $\propto \ln x/x^5$ with increasing radius, which causes the dip around $x \sim r_s$. More intuitively, since $p \propto 1/x^2$, there is the same mass in substructure in different equally spaced radial bins. Therefore, subhalos overlap more at smaller radii, – since there is less volume – and we should expect the correlated force to increase. At large radii, we get an increase again because of the strong decrease in ρ. The increase in the correlated force implies that subhalos source strong time dependent potential fluctuations at small radii. These could potentially be just as effective at disrupting subhalos as the tidal field from the parent halo.

4.5.3 Approaches to Understanding the Emergence of Fokker-Planck Behavior

As mentioned previously, averaging plays a large role in statistical approaches to physics. For the Brownian motion example, deriving the Fokker-Planck equation required time averaging. Diffusion came about because the correlation time of the stochastic force field from the heat bath was assumed negligible compared to observational time steps. As a result, for Brownian motion, time averages and ensemble averages are interchangeable. Hence, the system is ergodic, leading to a simplified analysis.

For a dark matter halo, dynamics takes place on many timescales, ranging from the

orbital time of particles in dense substructure all the way to the Hubble time – the timescale on which the external tidal field evolves. Moreover, the phase space is higher dimensional than in the Brownian motion case, leading to more information per particle. Analogous to the Brownian motion case, in order to simplify the dynamics and develop an analytic framework for understanding nonlinear halo evolution, we will need to take advantage of time and phase-space averaging. The first step, then, is to understand the ergodicity of a nonlinear halo. For simplicity, we'll once again use the Fractal Halo Model, which was described in detail in Section 4.3, to develop intuition.

The force acting on a test particle in a halo at $\boldsymbol{r}$ and time t is:

$$\boldsymbol{g}(\boldsymbol{r},t) = -Gm\sum_i \frac{\boldsymbol{r}-\boldsymbol{r}_i(t)}{|\boldsymbol{r}-\boldsymbol{r}_i(t)|^3} \tag{4.50}$$

where m is the mass of each particle, and $\boldsymbol{r}_i(t)$ tracks the position of each particle. We can rewrite this force trivially in the following way:

$$\boldsymbol{g}(\boldsymbol{r},t) \equiv \boldsymbol{g}_0(\boldsymbol{r},t) + \triangle\boldsymbol{g}(\boldsymbol{r},t) \tag{4.51}$$

where

$$\boldsymbol{g}_0(\boldsymbol{r},t) = -GM(r,t)\frac{\boldsymbol{r}}{r^3} \tag{4.52}$$

and eq. (4.51) defines $\triangle\boldsymbol{g}$. In the above, $\boldsymbol{g}_0$ is the force sourced by the smooth spherically symmetric halo, where $M(r,t)$ is the internal mass of the smooth halo at radius r and time t. Moreover, $\triangle\boldsymbol{g}$ is the force sourced by the perturbation on top of this smooth component. The ergodicity of the system can then be tested by creating histograms of $\triangle\boldsymbol{g}$ with the different elements of the histogram sampled using different averaging procedures.

To construct these histograms, we use the Fractal Halo Model to populate a halo with N subhalos. Then we calculate $\triangle\boldsymbol{g}$ by taking the difference between the actual force

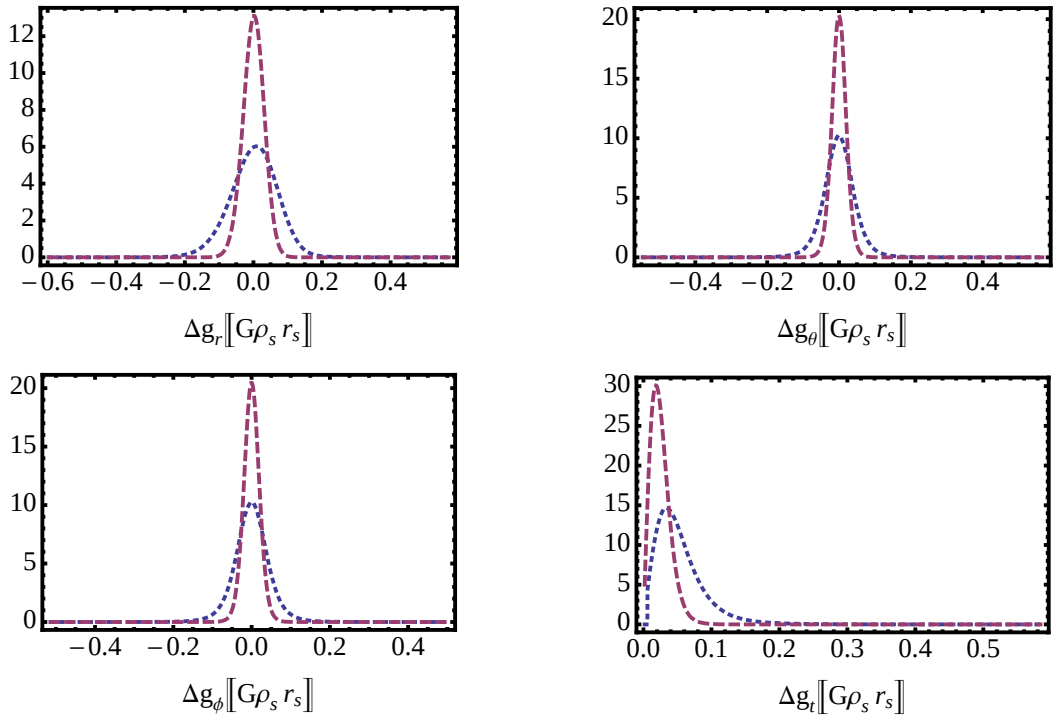

Figure 4-14: Normalized histograms of different components of $\triangle \boldsymbol{g}$ evaluated at a fixed phase space point, with $r = r_s$, for different realizations of subhalo positions. The above histograms give statistics associated with ensemble averaging. They were generated from 10^6 samples. The dotted curves corresponds to halos with $N = 101$ subhalos while the dashed curves correspond to halos with $N = 501$ subhalos. In both cases, the halos contained 10% mass in substructure.

acting at $\boldsymbol{r}$ – sourced by substructure and the diffuse component ρ_d – and the force at $\boldsymbol{r}$ assuming the smooth ensemble density $\bar{\rho}$.

Figure 4-14 shows the normalized histograms associated with ensemble averaging. Different histograms correspond to different components of $\triangle \boldsymbol{g}$, with the tangential component labeled by $\triangle g_t$. Each element of the histograms (10^6 samples) is evaluated at a fixed phase space point, with $r = r_s$, but for different realizations of subhalo positions. The dotted curves correspond to halos with $N = 101$ subhalos while the dashed curves correspond to halos with $N = 501$ subhalos. In both cases, the halos contained 10% mass in substructure. The distributions for $\triangle g_r$, $\triangle g_\theta$ and $\triangle g_\phi$ are all nearly gaussian while a Rayleigh distribution describes $\triangle g_t$. This is expected.

Different ensembles are independent and not correlated. Hence these distribution should describe a random variable $\triangle \boldsymbol{g}$, which is the sum of kicks that depend on the random locations of substructures. From the Central Limit Theorem, since the position of each subhalo is independent, we'd expect, for large N, to reproduce a Gaussian.

Moreover, the variance of the above gaussian distributions $\sigma^2 \propto 1/N$. This can be understood from random walk arguments. The random variable $\triangle \boldsymbol{g}$ is equivalent to a random walk of N steps, where each step is associated with the force from a single subhalo. For N subhalos, in halos of a fixed subhalo mass fraction, each step $l \propto 1/N$. Therefore the standard deviation after N steps is $l\sqrt{N} \propto 1/\sqrt{N}$, recovering the observed trend. Physically this makes sense. Not only are the kicks smaller, with larger N, but more subhalos lead to halos that are more spherically symmetric causing smaller deviations from $\boldsymbol{g}_0$.

Figure 4-15 shows the equivalent of Figure 4-14 but for phase space averaging. In this case, the different components of $\triangle \boldsymbol{g}$ are evaluated at $r = r_s$, with randomly chosen $\{\theta, \phi\}$ in a single realization of a halo. All other properties of the figures are the same. It is immediately clear that these distributions are not gaussian. This implies that the different elements in each histogram are not statistically independent. In other words, there are non-negligible correlations between the forces acting in a halo at the same radius but different $\{\theta, \phi\}$. Hence, phase space averaging and ensemble averaging are not equivalent. It should be stressed that the system does become more uncorrelated for larger N. This is expected since more kicking sources will decrease the correlation 'phase'. In other words, imagine choosing a particular location and find the closest subhalo. Now calculate the smallest angle the particle needs to traverse until the force is dominated by a new subhalo. The average value of this smallest angle, which I believe is a measure of a correlation 'phase', will be smaller if there are more subhalos. Note that, we've verified that phase space and ensemble averaging concurrently results in gaussian distributions.

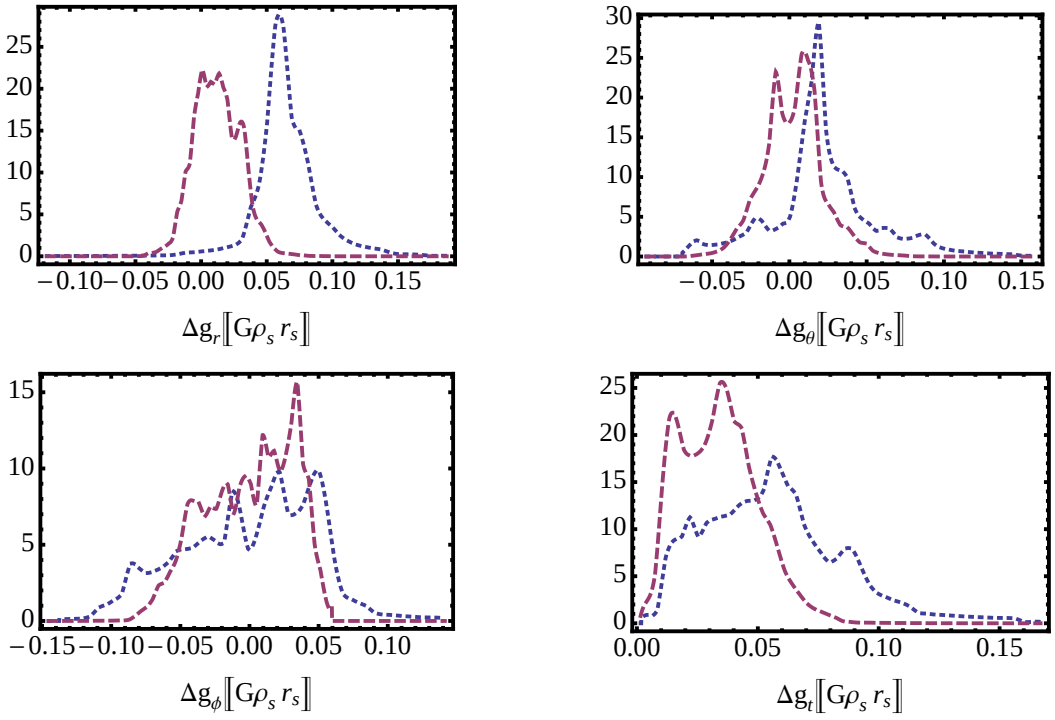

Figure 4-15: Normalized histograms of different components of $\triangle \boldsymbol{g}$ evaluated at $r = r_s$, with randomly chosen $\{\theta, \phi\}$ in a single realization of a halo. The above histograms give statistics associated with phase space averaging over angles. They were generated from 10^6 samples. The dotted curves corresponds to a halo with $N = 101$ subhalos while the dashed curves corresponds to a halo with $N = 501$ subhalos. In both cases, the halos contained 10% mass in substructure.

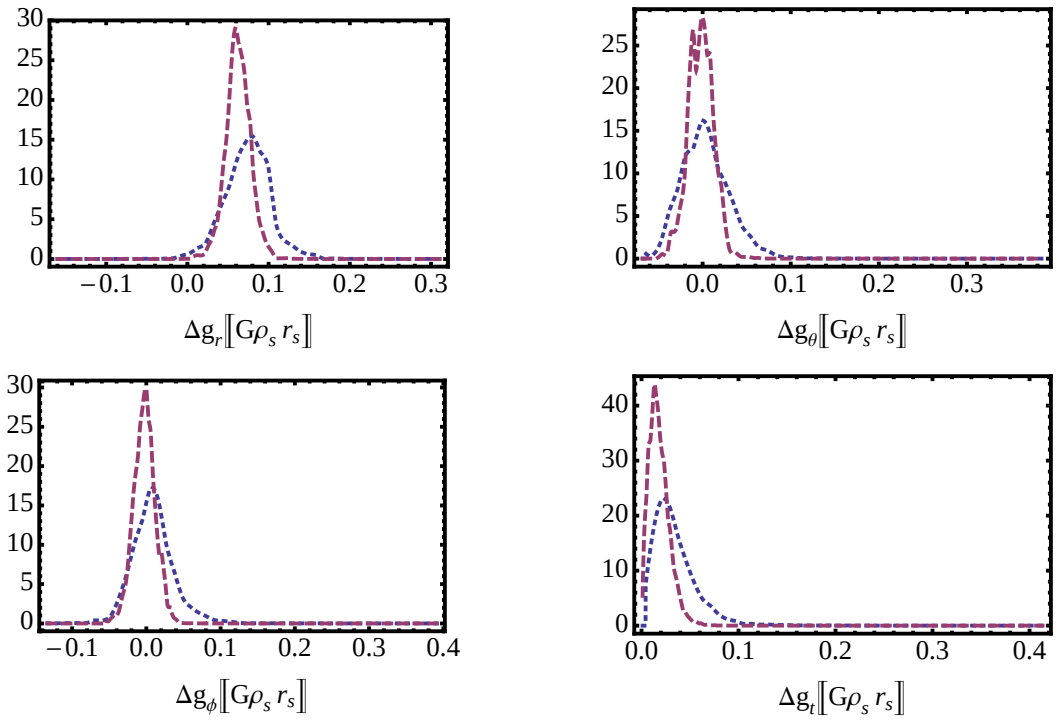

Figure 4-16: Normalized histograms of different components of $\triangle \boldsymbol{g}$ evaluated at a fixed phase space point, with $r = r_s$, in a single realization of a halo, but at different times. The subhalos evolved in the smooth diffuse component of the halo for $\sim 50 t_{\rm orb}$ where $t_{\rm orb}$ is the orbital period at r_s for a particle on a circular orbit. The above histograms give statistics associated with time averaging. They were generated from 10^6 samples evenly spaced in time. The dotted curves corresponds to a halo with $N = 101$ subhalos while the dashed curves corresponds to a halo with $N = 501$ subhalos. In both cases, the halos contained 10% mass in substructure.

Figure 4-16 shows the equivalent of Figure 4-14 but for time averaging. In this case, the different components of $\triangle \boldsymbol{g}$ are evaluated at a fixed phase space point, with $r = r_s$, and evenly spaced times as the subhalos orbit in the halo. The subhalos evolve in the smooth diffuse component for a time $\sim 50\ t_{\rm orb}$ where $t_{\rm orb}$ is the orbital period at r_s for a particle on a circular orbit. All other properties of the figures are the same. While the correlation time is clearly not negligible, it is interesting to note that the distributions are more gaussian then the phase space averaging case shown in Figure 4-15. The degree to which the above distributions are gaussian depends on the time steps of observations. Similar to the phase space averaging, the correlation time is roughly equivalent to the time it takes a new subhalo to dominate the force. This will be smaller for a larger number of subhalos.

Based on the above analysis, it seems that analytically it is necessary to ensemble average since the dynamics simplifies the most in that case. Moreover, in order for diffusion to take place, the forces in the halo need to be separated between those that occur on timescales much smaller than some prescribed time step and those that are larger. The dynamics occurring on smaller timescales will lead to diffusive behavior while the dynamics on longer timescales will need to be accounted for deterministically. Note however, that small correlation times are not a necessary condition for diffusive behavior. This will be discussed briefly in the Discussion section below.

4.6 Discussion

In this Chapter, we tried to understand why the density and pseudo-phase-space density profiles of dark matter halos are approximately universal. Our starting point was the evolution of a dark matter halo's phase space density. Motivated by Brownian motion, we showed that – when ensemble and phase space averaged – N-body simulations show evidence that their phase space densities diffuse. This is significant since this diffusion provides a mechanism for halos profiles to lose information and become universal.

In order to understand the source of this diffusion we performed numerical experiments on artificially constructed halos, for which we could control the halo's shape and substructure distribution. We found that substructure sources approximately the same amount of energy diffusion as seen in N-body simulations. However, substructure and the shape of the halo could not source enough diffusion in angular momentum. This implies that the external tides sourced by large scale structure is important for particle evolution even in a nonlinear halo.

Last, with the above results and framework we began to probe how best to describe this diffusive process analytically. In deriving a diffusion equation, averaging procedures are extremely important. For the case of Brownian motion, the system is ergodic since time averages are equivalent to ensemble averages. For a dark matter halo, we explored three different averaging procedures. We showed that ensemble averages are not equivalent to phase space averaging over the $\{\theta, \phi\}$ coordinates. In addition, we showed that the extent to which time averages and ensemble averages are equivalent depends on the time step between observations as well as the substructure distribution.

The above work needs to be generalized so that the artificially constructed halos are better representations of simulated halos. However, given this generalization, one potential approach to making a coherent picture will be to explicitly calculate the correlation time in halos. Understanding how this time depends on position in the halo and substructure distribution will then reveal in what limit diffusion is relevant.

Note though, that while each particle random walking would give rise to Fokker-Planck like behavior, that is not a required condition. More specifically, deterministic trajectories, when suitably averaged over can lead to diffusive dynamics, as was shown in the quasi-linear regime by Ma & Bertschinger (2004). The source of this diffusion is a correlation between the gravity and velocity fields. Therefore, another

potential way to understand universality is to model this correlation. This requires analyzing the statistics of the gravity and velocity fields and how they vary over different averaging procedures, as was explored partially in Section 4.5.3. Using both these approaches may provide an improved analytic description and shed light on the origin of universality.

Chapter 5

Conclusion

In this thesis we used a combination of analytic and numerical tools to gain intuition about different empirical results seen in N-body simulations. First, using a generalized model of halo formation known as Secondary Infall we analyzed the structure of halos, focusing on their density, anisotropy and pseudo-phase-space density profiles. We analytically showed that – within the context of our model – the inner slope of the density and pseudo-phase-space density profiles depends on how particles are torqued throughout evolution. In other words, angular momentum plays an important role in setting the structure of the halo at small radii. In addition, we found evidence for universality on intermediate scales since the structure of the halo, in this radial regime, does not depend on initial conditions or evolution history. Last, our predictions for the velocity anisotropy profile qualitatively matched expectations from N-body simulations. Differences between predictions of our model and simulated halos can be attributed to our assuming that all shells are radially cold and all particles in a shell have the same amplitude of angular momentum.

Because of restrictive assumptions inherent to the Secondary Infall model, and hoping to understand the origin of a halo's universality, we next focused on modeling a nonlinear halo's phase-space evolution. We first showed that – after ensemble and phase-space averaging – halos from N-body simulations undergo diffusion. This implies that a Fokker-Planck equation should describe a nonlinear halo's phase space

evolution. Analytically calculating the diffusion coefficients in the Fokker-Planck equation requires understanding the source of the diffusion. So, we tried to reproduce the diffusion observed in the N-body simulations by evolving particles in artificially constructed halos, where we controlled the halo shape and substructure distribution. We found that large scale tidal fields play a non-negligible role for the diffusion in angular momentum. Last, averaging and ergodicity are important in deriving a Fokker-Planck equation. So, we tested the ergodicity of dark matter halos by making histograms under different averaging schemes. We found that the extent to which time averages can be replaced with ensemble averages depends on the time steps in between samples. In other words, if the time step is larger than the correlation time, then the system is ergodic.

We believe the above provides the starting ingredients necessary to formalize an analytic description of nonlinear halo formation. The next steps include understanding what sets the correlation time in a halo and modeling the correlation between the gravity and velocity fields. With these advances, we'll have a description of halo evolution that is different in approach than most other studies. Moreover, with the diffusion coefficients in hand, we can directly calculate a time scale associated with when the system relaxes. Hence, we'll be able to conclusively say whether or not we expect universality in dark matter halos.

In summary, over the past 20 years, computer simulations have revealed many interesting properties of dark matter halos. Analytic modeling of these systems have, however, fallen behind. As a result, a gap exists in our understanding of halo formation since simulation results cannot be understood from a completely analytic framework. This thesis, we believe, has made steps to help bridge this gap.

Appendix A

Supplement to Chapter 2

A.1 Calculating $n_{\rm eff}$

The effective primordial power spectral index, $n_{\rm eff}$, relates our model parameter n to the halo mass M. The effective index is defined by:

$$n_{\rm eff} \equiv -2\frac{d\ln\sigma_R}{d\ln R} - 3 \tag{A.1}$$

where

$$\sigma_R^2 \equiv \int \frac{d^3k}{(2\pi)^3} P(k) W_R^2(k) \tag{A.2}$$

and

$$W_R(k) \equiv 3\frac{\sin(kR) - (kR)\cos(kR)}{(kR)^3}. \tag{A.3}$$

The scale R is set by the top hat mass of the halo ($M = 4\pi\rho_{m0}R^3/3$), where ρ_{m0} is the dark matter background density today. The power spectrum today, $P(k)$, is given by (Takada et al., 2006):

$$P(k) = \left(\frac{2k^2}{5H_0^2\Omega_m}\right)^2 P_{\mathcal{R}}(k) T^2(k) D^2(a=1) \tag{A.4}$$

where

$$\frac{k^3 P_{\mathcal{R}}(k)}{2\pi^2} = \triangle^2_{\mathcal{R}}(k_0)\left(\frac{k}{k_0}\right)^{n_s-1}, \tag{A.5}$$

D is the linear growth factor normalized so that $D/a \to 1$ as $a \to 0$, a is the scale factor, $T(k)$ is the transfer function and we choose cosmological parameters derived from WMAP7: $\triangle^2_{\mathcal{R}}(k_0) = 2.441 \times 10^{-9}$, $h = 0.704$, $\Omega_m = 0.272$, $n_s = 0.963$, with $k_0 = 0.002$ Mpc^{-1} (Komatsu et al., 2010). We calculate $T(k)$ using CMBFAST (Seljak & Zaldarriaga, 1996).

A.2 Tidal Torque Theory

We first derive eq. (2.28) using cosmological linear perturbation theory. Starting with the Zel'dovich approximation (Zel'dovich, 1970), we have:

$$\boldsymbol{r}(\boldsymbol{q}, t) = a(t)\Big(\boldsymbol{q} - D(t)\boldsymbol{\nabla}\phi(q)\Big) \tag{A.6}$$

where $\boldsymbol{r}$ is the physical radius, $\boldsymbol{q}$ is a Lagrangian coordinate, and ϕ, which is time independent, is related to the Newtonian potential Φ through the following:

$$\phi = \frac{1}{4\pi G\rho_m D a^2}\Phi \tag{A.7}$$

where ρ_m is the dark matter background density. The velocity, $\partial\boldsymbol{r}/\partial t$, then is given by:

$$\boldsymbol{v}(\boldsymbol{q}, t) = H(t)\boldsymbol{r}(\boldsymbol{q}, t) - a(t)\dot{D}(t)\boldsymbol{\nabla}\phi(\boldsymbol{q}) \tag{A.8}$$

where $H \equiv d\ln a/dt$ and dots denote derivatives with respect to time. Therefore, to first order in ϕ:

$$(\boldsymbol{r} - \boldsymbol{r}_0) \times (\boldsymbol{v} - \boldsymbol{v}_0) = -a^2\dot{D}(\boldsymbol{q} - \boldsymbol{q_0}) \times (\boldsymbol{\nabla}\phi - \boldsymbol{\nabla}\phi_0) \tag{A.9}$$

where $\boldsymbol{\nabla}\phi_0 \equiv \boldsymbol{\nabla}\phi(\boldsymbol{q}_0)$. Plugging this expression into eq. (2.27), taking an expectation value, defining $\boldsymbol{x} \equiv \boldsymbol{q} - \boldsymbol{q}_0$, rewriting in terms of the velocity perturbation variable $\boldsymbol{\Psi} \equiv -D\boldsymbol{\nabla}\phi$ and using index notation, we find:

$$\langle\tilde{\sigma}^2\rangle = \frac{a^4\dot{D}^2}{D^2}\epsilon_{ijk}\epsilon_{ilm}\int_{V_L} d^3x\rho_m a^3 x_j x_l \Big\langle \Big(\Psi_k(0) - \Psi_k(\boldsymbol{x})\Big)\Big(\Psi_m(0) - \Psi_m(\boldsymbol{x})\Big)\Big\rangle_C \quad \text{(A.10)}$$

where ϵ_{ijk} is the Levi-Civita tensor and V_L is the Lagrangian volume of the halo. We assume V_L is spherical with radius $x_{\rm max}$. Note that to linear order in ϕ, the Lagrangian coordinate $\boldsymbol{x}$ is equivalent to a comoving coordinate. The subscript C denotes an expectation value taken over constrained gaussian fields since we want to average only over peaks in the density field.

Using the formalism developed in (Bardeen et al., 1986), we choose, for simplicity, to use the zeroth and first order derivatives of the smoothed density field to constrain the velocity perturbation. Our treatment and conventions are identical to that used in Appendix A of Ma & Bertschinger (2004). For more details, please refer to this reference. We find:

$$\langle\Psi_i(\boldsymbol{x})\Psi_j(\boldsymbol{x})\rangle_C = \Big(\sigma_\Psi^2 - \frac{\bar{\eta}^2(x)}{\sigma_1^2}\Big)(\delta_{ij} - \hat{x}_i\hat{x}_j) + \left(\sigma_\Psi^2 - \frac{x^2\bar{\eta}^2(x)}{\sigma_0^2} - \frac{\big(\bar{\xi}(x) - 2\bar{\eta}(x)\big)^2}{\sigma_1^2}\right)\hat{x}_i\hat{x}_j \quad \text{(A.11)}$$

$$\langle\Psi_i(\boldsymbol{x})\Psi_j(0)\rangle_C = \Big(\frac{\gamma(x)}{x} - \frac{\bar{\eta}(0)\bar{\eta}(x)}{\sigma_1^2}\Big)\delta_{ij} + \Big(\frac{d\gamma(x)}{dx} - \frac{\gamma(x)}{x} - \frac{x\bar{\eta}(0)}{\sigma_1^2}\frac{d\bar{\eta}(x)}{dx}\Big)\hat{x}_i\hat{x}_j \quad \text{(A.12)}$$

$$\langle\Psi_i(0)\Psi_j(0)\rangle_C = \Big(\sigma_\Psi^2 - \frac{\bar{\eta}^2(0)}{\sigma_1^2}\Big)\delta_{ij} \quad \text{(A.13)}$$

where:

$$\sigma_\Psi^2 \equiv \frac{1}{3}\int \frac{d^3k}{(2\pi)^3} k^{-2} P(k) \tag{A.14}$$

$$\sigma_0^2 \equiv \int \frac{d^3k}{(2\pi)^3} P(k) W_R^2(k) \tag{A.15}$$

$$\sigma_1^2 \equiv \frac{1}{3}\int \frac{d^3k}{(2\pi)^3} k^2 P(k) W_R^2(k) \tag{A.16}$$

$$\bar{\eta}(x) \equiv \int \frac{d^3k}{(2\pi)^3} P(k) W_R(k) \frac{j_1(kx)}{kx} \tag{A.17}$$

$$\bar{\xi}(x) \equiv \int \frac{d^3k}{(2\pi)^3} P(k) W_R(k) j_0(kx) \tag{A.18}$$

$$\gamma(x) \equiv \int \frac{d^3k}{(2\pi)^3} P(k) k^{-3} j_1(kx). \tag{A.19}$$

$W_R(k)$ and $P(k)$ are defined in eq. (A.3) and (A.4) respectively and the spherical Bessel functions are $j_0(x) = x^{-1}\sin x$ and $j_1(x) = x^{-2}(\sin x - x\cos x)$. Eq. (A.12) corrects an error in equation (A15) of Ma & Bertschinger (2004).

Notice from eqs. (A.11) through (A.13) that the expressions separate into terms proportional to δ_{ij} and terms proportional to $\hat{x}_i\hat{x}_j$. The terms proportional to $\hat{x}_i\hat{x}_j$ vanish in eq. (A.10) because of the antisymmetry of the Levi-Civita tensors. Eq. (A.10) then reduces to:

$$\left\langle \tilde{\sigma}^2 \right\rangle_M = 2\frac{a^4\dot{D}^2}{D^2}\int_{V_L} d^3x \rho_m a^3 x^2 f(x,R) \tag{A.20}$$

where

$$f(x,R) = 2\sigma_\Psi^2 - \frac{2\gamma(x)}{x} - \frac{\bar{\eta}^2(x)}{\sigma_1^2} + \frac{2\bar{\eta}(0)\bar{\eta}(x)}{\sigma_1^2} - \frac{\bar{\eta}^2(0)}{\sigma_1^2} \tag{A.21}$$

Last, defining $u = x/x_{\max}$, we find:

$$\left\langle \tilde{\sigma}^2 \right\rangle_M = 6\frac{a^4\dot{D}^2}{D^2} M x_{max}^2 \int_0^1 u^4 f(u x_{\rm max}, R) du \equiv 6a^4\dot{D}^2 M x_{\rm max}^2 A^2(R) \tag{A.22}$$

In the above A has units of Mpc and $x_{\rm max} = R$ since the scale of the galaxy today is equivalent to its lagrangian size to linear order in perturbation theory. Note that f/D^2 is time independent.

Now, we derive eq. (2.30). Consistency with the secondary infall model demands that we assume $\Omega_m = 1$. Equating the time dependence of eq. (2.28) and eq. (2.29) for an Einstein de-Sitter universe ($D = a$) at early times ($r_{\rm max} \propto t^{2/3}$), we find $p = 2n$ where $p = 2\gamma + 4$. Given this relationship, we now equate eq. (2.28) to eq. (2.29) and solve for B. We find:

$$B = \frac{2}{3}\sqrt{2(7-2n)}a^2 \left(\frac{r_{\rm max}}{r_{\rm ta}}\right)^{n-1} \frac{A(R)}{r_{\rm ta}} \tag{A.23}$$

where we've used eqs. (3.3) and (2.18) evaluated at early times to cancel the mass as well as the relationship $r_{\rm max} = a x_{\rm max}$. Now we evaluate eq. (A.23) at early times since tidal torque theory only applies when the halo is linear. To relate $r_{\rm max}$ at some initial time (t_i) to $r_{\rm ta}$ today (t_0), we use the conservation of mass.

$$\frac{4\pi}{3}\rho_B(t_i) r_{\rm max}^3(t_i) = \frac{4\pi}{3}\mathcal{M}(1)\rho_B(t_0) r_{ta}^3(t_0) \tag{A.24}$$

Evaluating eq. (A.23) at t_i with the use of eq. (A.24) and noting that $r_{\rm ta} \propto t^\beta$, we find:

$$B = \frac{2}{3}\sqrt{2(7-2n)}\mathcal{M}(1)^{(n-1)/3}\frac{A(R)}{r_{\rm ta}(t_0)} \tag{A.25}$$

As expected, the time dependence of B vanishes. Last, assuming $r_{\rm ta}(t_0) = R$, we reproduce eq. (2.30). The quantities $n, R, A(R)$ are calculated in an $\Omega_m = 1$ universe

with the same background matter density and power spectrum of ΛCDM today. This ensures that the statistics, mass, and size of halos in both universes are equivalent today.

As mentioned previously, eq. (2.30) overestimates the angular momentum of particles at turnaround by a factor of 1.5 to 2.3. One potential source of error is to assume the lagrangian volume is spherical. Assuming an ellipsoidal lagrangian volume with axis ratios $1 : a : b$, we find that B is at most reduced by 8% when $0.5 < a, b < 1$. The discrepancy may be caused by not including higher order constraints on the smoothed density field. However, comparing B when calculated using zeroth and first order derivative constraints with B when calculated without using constraints results in only percent level differences; so it seems unlikely that constraints would have a significant effect.

N-body simulations use friends-of-friends group finders in order to identify halos and subhalos (Davis et al., 1985; Springel et al., 2008). This algorithm, however, removes particles that are grouped to neighboring halos and hence neglects a contribution to $\tilde{\sigma}^2$. Trying to mimick this selection effect, we replaced eq. (A.20) with

$$\left\langle \tilde{\sigma}^2 \right\rangle_M = 2\frac{a^4\dot{D}^2}{D^2}\int_0^\infty d^3x e^{-x^2/2\bar{R}^2}\rho_m a^3 x^2 f(x,R) \tag{A.26}$$

where $\bar{R} \equiv (2/9\pi)^{1/6}R$ ensures that the mass enclosed within the lagrangian volume is equal to the mass of the halo calculated by the simulation. However, calculating B in this manner leads to overestimating the angular momentum at turnaround by ~ 4, as opposed to ~ 2 beforehand. Since $f(x, R)$ is an increasing function of x ($f \sim x^{1.34}$ near R for $10^{12}M_\odot$ halos), most of the contribution to $A(R)$ comes from close to R. Therefore, while the gaussian cutoff decreases the contribution to B around R, it includes contributions beyond R, leading to a worse estimate. This highlights that B significantly depends on the outer parts of the halo. Hence, overestimating B by ~ 2 is reasonable.

Last, note that the parameter B is set during the linear regime. Assuming that the shell is dominated by substructure at turnaround, nonlinear interactions like dynam-

ical friction and tidal stripping play an important role from the time of turnaround to the first pericenter passage (Gan et al., 2010; Zentner et al., 2005). As time goes on, these effects become less important since substructure in the shell becomes subdominant. Including these extra interactions should lead to smaller estimates of B at first pericenter passage and hence potentially explain our overestimate, but is beyond the scope of this work.

A.3 Evolution After Turnaround

In this Appendix, we use dimensional analysis in order to gain intuition about ϖ, a parameter that describes tidal torque after turnaround. First, consider the time derivative of L^2, where $\boldsymbol{L}$ is the angular momentum per unit mass of a particle with radius r at time t.

$$\frac{dL^2}{dt} = 2\Big(r^2(\boldsymbol{v}\cdot\boldsymbol{a}) - (\boldsymbol{r}\cdot\boldsymbol{a})(\boldsymbol{r}\cdot\boldsymbol{v})\Big) \tag{A.27}$$

In the above, $\boldsymbol{a}$ ($\boldsymbol{v}$) is the acceleration (velocity) of the particle. We now decompose the acceleration vector into a radial ($\hat{\boldsymbol{r}}$) and tangential ($\hat{\boldsymbol{t}}$) component and use this basis to rewrite the velocity vector.

$$\boldsymbol{a} = a_r\hat{\boldsymbol{r}} + a_t\hat{\boldsymbol{t}} \tag{A.28}$$

$$\boldsymbol{v} = v_r\hat{\boldsymbol{r}} + v_t\hat{\boldsymbol{t}} + v_p\hat{\boldsymbol{p}} \tag{A.29}$$

The direction $\hat{\boldsymbol{p}}$ is orthogonal to both $\hat{\boldsymbol{r}}$ and $\hat{\boldsymbol{t}}$. Note that all basis vectors depend on position. Plugging in the above decomposed vectors into eq. (A.27), we find:

$$\frac{dL^2}{dt} = 2r^2 v_t a_t. \tag{A.30}$$

As expected, changes in L^2 are sourced by deviations from spherical symmetry that create nonzero $\boldsymbol{a}_t$. Now, imagine a spherically symmetric halo, roughly described

by our self-similar infall model with $\varpi > 0$, with a clump of mass m in the shell at radius r_2. We assume that m is small enough so that it does not influence the radial equation of motion of the shell at r. We focus on $\varpi > 0$ since this is required in order for the density profile of a $10^{12} M_\odot$ halo to be consistent with the NFW profile (Section 2.6.1).

Next, consider averaging dL^2/dt over an orbital period and over a spherical shell of radius r, in order to compare the change in angular momentum sourced by the clump at r_2 to our model's prescription for angular momentum evolution. For $\varpi > 0$, orbits are roughly circular at late times. Hence, we assume averaging over an orbital period is equivalent to evaluating the right hand side of eq. (A.30) at roughly the apocenter radius of the shell. As described in Section 2.2, the orbital planes of all particles in a shell at r are randomly aligned. Therefore we expect v_t averaged over a sphere to vanish. However, if there exists an excess mass m, then all the particles will be pulled slightly in that direction, leading to a nonzero average. We therefore assume $v_t \propto P a_t$ where P, the orbital period of the particle, is taken to be a dynamical time ($P \propto \rho(r)^{-1/2}$). Last assuming $r \ll r_2$, we find:

$$\left\langle \frac{dL^2}{dt} \right\rangle \propto \frac{r^2 m^2}{r_2^4 \rho^{1/2}}. \tag{A.31}$$

In order for the secondary infall halo model to be consistent, the right hand and left hand side must have the same time scaling. Assuming $m \propto t^\mu$, associating r and r_2 with their respective apocenters, and noting from eq. (3.37) that $r \propto t^{2\varpi}$, $r_2 \propto t^{2\varpi}$, and $\rho \propto t^{-6\varpi}$, we find:

$$\varpi = \frac{1}{3}(1 + 2\mu) \tag{A.32}$$

The same scaling relationship holds for $r \gg r_2$. Hence one could imagine substructure in the shell at r sourcing a change in L^2 of the shell at r_2 and substructure in the shell at r_2 sourcing a change in L^2 of the shell at r. Therefore, a hierarchy of substructure non-spherically distributed, which is subdominant to the monopole contribution of the halo, would result in a halo roughly consistent with our described

secondary infall model.

Eq. (A.32), which is only valid for $\mu > -1/2$ since we assumed $\varpi > 0$, together with eq. (3.37) relates the steepness of the inner density profile to the mass loss rate of substructure. If the clump does not lose mass ($\mu = 0$), then $\varpi = 1/3$ implies $\rho \propto r^0$. If the clump loses mass ($\mu < 0$), eq. (3.37) predicts steeper density profiles. Substructure dominated by baryons will lose less mass than substructure dominated by dark matter, since baryons clump more easily and hence have higher densities. Therefore, according to the above analysis, pure dark matter simulations *should* have steeper density profiles than galaxies which include baryons. This is expected since baryons stir particles around more efficiently, causing larger pericenters and less dense interiors. A more thorough treatment that involves constraining ϖ with simulations is beyond the scope of this paper.

Appendix B

Supplement to Chapter 3

B.1 Deriving the Consistency Relationship

In this Appendix, we derive eq. (3.24). Self-similarity imposes that the total radial (or tangential) kinetic energy at time t contained within radius r is given by:

$$K_i(r,t) = M_{ta}(t)\frac{r_{ta}^2}{t^2}\mathcal{K}_i(\lambda) \tag{B.1}$$

where $i = \{r,t\}$ is used for shorthand to denote the radial or tangential direction. The kinetic energy also obeys the following relationship.

$$K_i(r,t) = \frac{1}{2}\int_0^{M_{ta}} dM_* v_i^2(t,t_*) H\left[r - R(t,t_*)\right] \tag{B.2}$$

where $dM_*, v_i(t,t_*), R(t,t_*)$ is the mass, velocity, and radius of a shell at time t which turned around at t_* and H is the heaviside function. Since, after a short time, shells begin to oscillate on a timescale much shorter than the growth of the halo, we can replace v_i^2 with a time averaged version $\langle v_i^2 \rangle$ and the heaviside function with a weighting that takes into account how often the shell is below r. More specifically, considering a shell with turnaround time t_* such that $r_p(t,t_*) < r < r_a(t,t_*)$, we have:

$$\left\langle v_i^2(t,t_*)\right\rangle \;\rightarrow\; \left(\int_{r_p}^{r} v_i^2 dt\right) / \left(\int_{r_p}^{r} dt\right) \tag{B.3}$$

$$H[r - R(t,t_*)] \;\rightarrow\; \left(\int_{r_p}^{r} dt\right) / \left(\int_{r_p}^{r_a} dt\right) \tag{B.4}$$

where we've left the dependence on t_* implicit. Eq. (B.3) only averages over scales below r since that is where the shell contributes to the kinetic energy. Eq. (B.4) is identical to what is done in Fillmore and Goldreich, in order to analytically calculate the mass profile at small scales (Fillmore & Goldreich, 1984).

Using eqs. (B.3) and (B.4), generalizing to the case where $r < r_p$ and $r > r_a$, plugging into eq. (B.2), dividing by $K_i(r_{ta}, t)$ and assuming a power law for the kinetic energy profiles in the form of eqs. (3.12) and (3.13), we reproduce the consistency equation. The equation has a proportionality constant not only because of eq. (3.21) but also because we do not include $\mathcal{K}_i(1)$. This overall constant does not affect the asymptotic slopes.

Bibliography

Ascasibar, Y., Yepes, G., Gottlöber, S., & Müller, V. 2004, Mon. Not. R. Astron. Soc., 352, 1109

Bardeen, J. M., Bond, J. R., Kaiser, N., & Szalay, A. S. 1986, Astrophys. J., 304, 15

Barnes, J., & Efstathiou, G. 1987, Astrophys. J., 319, 575

Bertschinger, E. 1985, Astrophys. J., 58, 39

—. 2001, Astrophys. J., 137, 1

Binney, J., & Tremaine, S. 2008, Galactic Dynamics: Second Edition, ed. Binney, J. & Tremaine, S. (Princeton University Press)

Book, L. G., Brooks, A., Peter, A. H. G., Benson, A. J., & Governato, F. 2011, Mon. Not. R. Astron. Soc., 411, 1963

Boylan-Kolchin, M., Springel, V., White, S. D. M., & Jenkins, A. 2010, Mon. Not. R. Astron. Soc., 406, 896

Cen, R., Dong, F., Bode, P., & Ostriker, J. P. 2004, ArXiv Astrophysics e-prints

Chandrasekhar, S. 1943, Astrophys. J., 97, 255

—. 1987, Ellipsoidal figures of equilibrium, ed. Chandrasekhar, S.

Cruz, F., Velázquez, H., & Aceves, H. 2007, Revista Mexicana de Astronomia y Astrofisica, 43, 95

Davis, M., Efstathiou, G., Frenk, C. S., & White, S. D. M. 1985, Astrophys. J., 292, 371

de Blok, W. J. G. 2003, in Revista Mexicana de Astronomia y Astrofisica, vol. 27, Vol. 17, Revista Mexicana de Astronomia y Astrofisica Conference Series, ed. V. Avila-Reese, C. Firmani, C. S. Frenk, & C. Allen, 17–18

Dehnen, W. 2000, Astron. J., 119, 800

Del Popolo, A. 2009, Astrophys. J., 698, 2093

—. 2010, Mon. Not. R. Astron. Soc., 1312

Diemand, J., Moore, B., & Stadel, J. 2004, Mon. Not. R. Astron. Soc., 353, 624

Donato, F., Gentile, G., Salucci, P., et al. 2009, Mon. Not. R. Astron. Soc., 397, 1169

Doroshkevich, A. G. 1970, Astrofizika, 6, 581

Fakhouri, O., Ma, C.-P., & Boylan-Kolchin, M. 2010, Mon. Not. R. Astron. Soc., 406, 2267

Faltenbacher, A., Hoffman, Y., Gottlöber, S., & Yepes, G. 2007, Mon. Not. R. Astron. Soc., 376, 1327

Fillmore, J. A., & Goldreich, P. 1984, Astrophys. J., 281, 1

Gan, J., Kang, X., van den Bosch, F. C., & Hou, J. 2010, ArXiv e-prints

Gentile, G., Salucci, P., Klein, U., Vergani, D., & Kalberla, P. 2004, Mon. Not. R. Astron. Soc., 351, 903

Gerhard, O. E., & Binney, J. 1985, Mon. Not. R. Astron. Soc., 216, 467

Gott, III, J. R. 1975, Astrophys. J., 201, 296

Graham, A. W., Merritt, D., Moore, B., Diemand, J., & Terzić, B. 2006, Astron. J., 132, 2701

Gunn, J. E. 1977, Astrophys. J., 218, 592

Gunn, J. E., & Gott, III, J. R. 1972, Astrophys. J., 176, 1

Hansen, S. H., & Moore, B. 2006, New Astronomy, 11, 333

Hayashi, E., Navarro, J. F., & Springel, V. 2007, Mon. Not. R. Astron. Soc., 377, 50

Hiotelis, N. 2002, Astron. Astrophys., 382, 84

Hoffman, Y., & Shaham, J. 1985, Astrophys. J., 297, 16

Hoyle, F. 1951, in Problems of Cosmical Aerodynamics, 195–197

Kalnajs, A. J. 1991, in Dynamics of Disc Galaxies, ed. B. Sundelius, 323–+

Komatsu, E., Smith, K. M., Dunkley, J., et al. 2010, ArXiv e-prints

Le Delliou, M., & Henriksen, R. N. 2003, Astron. Astrophys., 408, 27

Ludlow, A. D., Navarro, J. F., Springel, V., et al. 2010, Mon. Not. R. Astron. Soc., 406, 137

Ma, C., & Bertschinger, E. 2004, Astrophys. J., 612, 28

Merritt, D., & Quinlan, G. D. 1998, Astrophys. J., 498, 625

Milosavljević, M., & Merritt, D. 2003, Astrophys. J., 596, 860

Moore, B., Quinn, T., Governato, F., Stadel, J., & Lake, G. 1999, Mon. Not. R. Astron. Soc., 310, 1147

Navarro, J. F., Frenk, C. S., & White, S. D. M. 1996, Astrophys. J., 462, 563

—. 1997, Astrophys. J., 490, 493

Navarro, J. F., Ludlow, A., Springel, V., et al. 2010, Mon. Not. R. Astron. Soc., 402, 21

Nusser, A. 2001, Mon. Not. R. Astron. Soc., 325, 1397

Peebles, P. J. E. 1969, Astrophys. J., 155, 393

Perlmutter, S., Aldering, G., Goldhaber, G., et al. 1999, Astrophys. J., 517, 565

Power, C., Navarro, J. F., Jenkins, A., et al. 2003, Mon. Not. R. Astron. Soc., 338, 14

Rasia, E., Tormen, G., & Moscardini, L. 2004, Mon. Not. R. Astron. Soc., 351, 237

Ricotti, M., Pontzen, A., & Viel, M. 2007, Astrophys. J. Lett., 663, L53

Riess, A. G., Filippenko, A. V., Challis, P., et al. 1998, Astron. J., 116, 1009

Rubin, V. C., & Ford, Jr., W. K. 1970, Astrophys. J., 159, 379

Ryden, B. S., & Gunn, J. E. 1987, Astrophys. J., 318, 15

Salucci, P., Lapi, A., Tonini, C., et al. 2007, Mon. Not. R. Astron. Soc., 378, 41

Scherrer, R. J., & Bertschinger, E. 1991, Astrophys. J., 381, 349

Seljak, U., & Zaldarriaga, M. 1996, Astrophys. J., 469, 437

Sesana, A., Haardt, F., & Madau, P. 2007, Astrophys. J., 660, 546

Sikivie, P., Tkachev, I. I., & Wang, Y. 1997, Phys. Rev. D, 56, 1863

Springel, V. 2005, Mon. Not. R. Astron. Soc., 364, 1105

Springel, V., White, S. D. M., Tormen, G., & Kauffmann, G. 2001, Mon. Not. R. Astron. Soc., 328, 726

Springel, V., Wang, J., Vogelsberger, M., et al. 2008, Mon. Not. R. Astron. Soc., 391, 1685

Takada, M., Komatsu, E., & Futamase, T. 2006, Phys. Rev. D, 73, 083520

Taylor, J. E., & Navarro, J. F. 2001, Astrophys. J., 563, 483

Vass, I. M., Valluri, M., Kravtsov, A. V., & Kazantzidis, S. 2009, Mon. Not. R. Astron. Soc., 395, 1225

Vogelsberger, M., Mohayaee, R., & White, S. D. M. 2010, ArXiv e-prints

Wang, J., & White, S. D. M. 2009, Mon. Not. R. Astron. Soc., 396, 709

White, S. D. M. 1984, Astrophys. J., 286, 38

White, S. D. M., & Zaritsky, D. 1992, Astrophys. J., 394, 1

Williams, L. L. R., Babul, A., & Dalcanton, J. J. 2004, Astrophys. J., 604, 18

Zel'dovich, Y. B. 1970, Astron. Astrophys., 5, 84

Zentner, A. R., Berlind, A. A., Bullock, J. S., Kravtsov, A. V., & Wechsler, R. H. 2005, Astrophys. J., 624, 505

Zukin, P., & Bertschinger, E. 2010a, Phys. Rev. D., 82, 104044

—. 2010b, Phys. Rev. D., 82, 104045